Leibniz-Institut für Astrophysik Potsdam

X-ray studies of exoplanet systems

Cumulative Dissertation
to obtain the academic degree
”doctor rerum naturalium”
(Dr. rer. nat.)
in the scientific discipline of astrophysics

submitted to the
Faculty of Mathematics and Natural Sciences
of the University Potsdam

Mary Grace Foster

Potsdam, 11. February 2022
Disputation: Potsdam, 22. September 2022

Published online on the
Publication Server of the University of Potsdam:
https://doi.org/10.25932/publishup-56215
https://nbn-resolving.org/urn:nbn:de:kobv:517-opus4-562152

Abstract

X-rays are integral to furthering our knowledge of exoplanetary systems. In this work we discuss the use of X-ray observations to understand star-planet interactions, mass-loss rates of an exoplanet's atmosphere and the study of an exoplanet's atmospheric components using future X-ray spectroscopy.

The low-mass star GJ 1151 was reported to display variable low-frequency radio emission, which is an indication of coronal star-planet interactions with an unseen exoplanet. In chapter 5 we report the first X-ray detection of GJ 1151's corona based on XMM-Newton data. Averaged over the observation, we detect the star with a low coronal temperature of 1.6 MK and an X-ray luminosity of $L_X = 5.5 \times 10^{26}$ erg/s. This is compatible with the coronal assumptions for a sub-Alfvénic star-planet interaction origin of the observed radio signals from this star.

In chapter 6, we aim to characterise the high-energy environment of known exoplanets and estimate their mass-loss rates. This work is based on the soft X-ray instrument on board the Spectrum Roentgen Gamma (SRG) mission, eROSITA, along with archival data from ROSAT, *XMM-Newton*, and *Chandra*. We use these four X-ray source catalogues to derive X-ray luminosities of exoplanet host stars in the 0.2-2 keV energy band. A catalogue of the mass-loss rates of 287 exoplanets is presented, with 96 of these planets characterised for the first time using new eROSITA detections. Of these first time detections, 14 are of transiting exoplanets that undergo irradiation from their host stars that is of a level known to cause observable evaporation signals in other systems, making them suitable for follow-up observations.

In the next generation of space observatories, X-ray transmission spectroscopy of an exoplanet's atmosphere will be possible, allowing for a detailed look into the atmospheric composition of these planets. In chapter 7, we model sample spectra using a toy model of an exoplanetary atmosphere to predict what exoplanet transit observations with future X-ray missions such as Athena will look like. We then estimate the observable X-ray transmission spectrum for a typical Hot Jupiter-type exoplanet, giving us insights into the advances in X-ray observations of exoplanets in the decades to come.

Zusammenfassung

Röntgenstrahlen sind ein wesentlicher Bestandteil, um unser Wissen über extrasolare Planetensysteme zu vertiefen und zu erweitern. In dieser Arbeit erörtern wir den Einsatz von Röntgenbeobachtungen zum Verständnis von Stern-Planeten-Interaktionen, der Abschätzung von Massenverlustraten von Exoplanetenatmosphären und die Untersuchung der atmosphärischen Komponenten eines Exoplaneten mithilfe zukünftiger Röntgenspektroskopie.

Beobachtungen des massearmen Sterns GJ 1151 deuten auf eine variable Emission niederfrequenter Radiostrahlung hin, was als Indiz für koronale Stern-Planeten-Wechselwirkungen mit einem unsichtbaren Exoplaneten angesehen wird. In Kapitel 5 berichten wir über den ersten Röntgennachweis der Korona von GJ 1151, basierend auf XMM-Newton Daten. Über die gesamte Beobachtungsdauer gemittelt, weisen wir den Stern mit einer niedrigen koronalen Temperatur von 1,6 MK und einer Röntgenluminosität von $L_X = 5,5 \times 10^{26}\,\mathrm{erg/s}$ nach. Dieser Nachweis im Röntgenlicht ist kompatibel mit der Annahme, dass sub-Alfvénische Wechselwirkungen zwischen stellarer Corona und Exoplanet die Ursache für die beobachteten Radiosignale des Sterns sind.

Kapitel 6 zielt darauf ab, die hochenergetische Umgebung bekannter Exoplaneten zu charakterisieren und die Massenverlustraten der Planetenatmosphären abzuschätzen. Diese Arbeit basiert auf neu gewonnenen Daten des Instruments für weiche Röntgenstrahlung an Bord der Spectrum Roentgen Gamma (SRG) Mission, eROSITA, und wird komplementiert von Archivdaten von ROSAT, XMM-Newton und Chandra. Mithilfe dieser vier Röntgenquellenkataloge vermessen wir die Röntgenhelligkeit der Zentralsterne von bekannten Exoplanetensytemen im Energiebereich von 0,2-2 keV. Die Ergebnisse sind zusammen mit den errechneten Massenverlustraten von 287 Exoplaneten in einem Katalog zusammengefasst, darunter 96 Planeten, die zum ersten Mal durch neue eROSITA-Nachweise charakterisiert wurden. Bei 14 dieser Erstnachweise handelt es sich um transitierende Exoplaneten, die von ihrem Heimatstern so stark bestrahlt werden, dass beobachtbare Signale, ausgelöst durch die Verdampfung ihrer Atmosphäre, zu erwarten sind. Speziell diese Systeme eignen sich besonders für Folgebeobachtungen.

Mit der nächsten Generation von Weltraumobservatorien wird die Röntgentransmissionsspektroskopie von extrasolaren Planetenatmosphären möglich sein, was nie dagewesene Details über die atmosphärische Zusammensetzung dieser Planeten ans Licht bringen wird. In Kapitel 7 modellieren wir Transmissionsspektren mithilfe eines vereinfachten Modells einer Exoplanetenatmosphäre um vorherzusagen, wie Transitbeobachtungen von Exoplaneten mit zukünftigen Röntgenmissionen wie Athena aussehen werden. Wir schätzen dann das beobachtbare Röntgentransmissionsspektrum für einen typischen Exoplaneten vom Typ Hot Jupiter ab, was uns einen Einblick in die zu erwartenden Fortschritte bei der Röntgenbeobachtung von Exoplaneten in den kommenden Jahrzehnten gibt.

Contents

Abstract i

Zusammenfassung iii

List of Figures ix

List of Tables xiii

1 Introduction to Exoplanets 1
- 1.1 Exoplanet Detection Methods . . . 1
  - 1.1.1 Radial Velocity . . . 1
  - 1.1.2 Microlensing . . . 3
  - 1.1.3 Imaging . . . 3
  - 1.1.4 Transits . . . 3
- 1.2 Mass-Loss . . . 4

2 Introduction to Host Stars 7
- 2.1 Stellar Atmosphere . . . 7
- 2.2 Stellar Corona . . . 7
- 2.3 Stellar X-rays . . . 9
- 2.4 Magnetic Dynamo . . . 9
- 2.5 Star-Planet Interactions . . . 10
  - 2.5.1 Tidal Interactions . . . 10
  - 2.5.2 Magnetic Interactions . . . 11

3 X-ray observatories 15
- 3.1 ROSAT . . . 15
- 3.2 Chandra . . . 17
- 3.3 XMM-Newton . . . 17
- 3.4 eROSITA . . . 18
- 3.5 Athena . . . 19

4 Overview of the included manuscripts 21

5 The corona of GJ 1151 in the context of star-planet interaction 25
- 5.1 Abstract . . . 25
- 5.2 Introduction . . . 25
- 5.3 Observations and data analysis . . . 26
- 5.4 Results . . . 28
  - 5.4.1 An X-ray detection of GJ 1151 with XMM-Newton . . . 28
  - 5.4.2 Temporal variability of GJ 1151's corona . . . 28

5.4.3 GJ 1151's coronal properties from X-ray spectra 32
5.4.4 Consistency with previous upper limits 33
5.5 Discussion 34
5.6 Conclusions 34

6 Exoplanet X-ray irradiation and evaporation rates with eROSITA 35
6.1 Abstract 35
6.2 Introduction 35
6.3 Observations 36
6.3.1 eROSITA 36
6.3.2 ROSAT 37
6.3.3 XMM-Newton 37
6.3.4 Chandra 38
6.4 Data analysis 38
6.4.1 Catalogue cross-matching 38
6.4.2 Flux conversions 43
6.4.3 Optical loading in eROSITA data 47
6.5 Results 48
6.5.1 New X-ray detections of exoplanet host stars 48
6.5.2 Flux comparisons for different X-ray missions 51
6.5.3 X-ray irradiation and mass loss of exoplanets 51
6.6 Discussion 55
6.6.1 Exoplanet mass-loss rates in context 55
6.6.2 Interesting individual targets identified with eROSITA data . 56
6.7 Conclusion 57
6.8 Appendix 58
6.8.1 X-ray fluxes of host stars with nearby stellar companions . . . 58
6.8.2 Table of exoplanet irradiation fluxes and estimated mass-loss rates 60

7 Identifying interesting planetary systems for future X-ray observations 63
7.1 Abstract 63
7.1.1 eROSITA 64
7.2 Data Analysis 64
7.2.1 Flux Comparisons 65
7.3 Results 65
7.3.1 XUV Irradiation 65
7.3.2 Mass-Loss Rates 66
7.4 Discussion 67
7.4.1 Interesting Systems 67
7.4.2 Simulated Athena Spectra 68
7.5 Conclusion 70

8 Conclusions 75
8.1 Scientific outcomes 75
8.1.1 Star-planet interactions 75
8.1.2 Mass-loss rates 75
8.1.3 Identifying new targets 75

8.2 Next generation of observatories . . . 76
    8.2.1 Athena . . . 76
    8.2.2 Lynx . . . 76
8.3 End notes on X-ray studies of exoplanets . . . 77

Bibliography **79**

Acknowledgment **89**

Declaration **91**

List of Figures

1.1 Simple illustration of the radial velocity method of detecting an exoplanet (black) orbiting its host star (yellow). The planet's gravitational pull on the host star causes the star to "wobble" which, in turn, causes the light from the star to appear slightly blue-shifted as the star moves closer to the observer in it's "wobble", and slightly red-shifted as the star moves away from the observer. 2

1.2 Simple illustration of an exoplanet (black) transiting its host star (yellow). 4

1.3 Transit curve of HD 209458 b from Charbonneau et al. (2000). The transits were observed a week apart and plotted as a function of time from the centre of the transit, T_c. The larger scatter in the data from 16/9/1999 (bottom) is due to the shorter exposure time compared to that on 9/9/1999 (top). 5

2.1 A sketch of the magnetic field of the solar corona from Low (1996) showing the open magnetic field lines, along which the solar winds are carried into space. This figure also shows the closed magnetic fields lines where plasma is trapped due to the high electrical conductivity conditions. 8

2.2 A typical tidally interacting system from Remus et al. (2012). Here a planet, B, is interacting with the star, A, and exerting a tidal force. The star adjusts itself with a phase lag, δ, due to internal friction. The adjustment is broken into to an adiabatic component and a weaker, dissipative one. 11

2.3 An uni-polar inductor model for a white-dwarf system from Willes & Wu (2005). A cone of radio emission is being generated by the sub-Alfvénic interaction, and is then dragged around by the exoplanet. 12

2.4 Radio image of GJ 1151 (denoted by the red cross-hairs) from Vedantham et al. (2020). The images were takes at two different epochs; 16 June 2014 and 28 May 2014 shown on the left and right respectively, with the star being visible at radio wavelengths in the left panel and not the right. 13

3.1 Exposure map from Voges et al. (1999). This map comes from the second processing of the RASS data. Due to the way RASS scans the sky, there is a higher exposure at the ecliptic poles than at the ecliptic equator. Note that the white spots represent locations where there were not enough guide stars for the satellite's automatic measuring system. 16

3.2 Effective exposure map from Predehl et al. (2021). This map is derived from eRASS1, the first eROSITA all-sky survey. The effective exposure values range from 100s at the ecliptic equator to more than 10 000s close to the ecliptic poles. 18

5.1 X-ray image of GJ1151 observed in the 0.2-2 keV energy band with *XMM-Newton* on 1st November 2018. The top panel shows the combined image from the two MOS cameras, the bottom panel shows the image extracted from the PN detector where the target position was located on a chip edge. GJ1151 is marked by a circle with a 20″ radius. 27

5.2 The *XMM-Newton* X-ray light curve of GJ 1151 with 1 ks time binning, using the co-added signal from both MOS detectors. The solid-line curve is the signal from the source region containing the true source signal and the underlying background, the background itself as estimated from a nearby region is shown as a dashed line. The star shows variability, possibly the decay of a flare at the beginning of the light curve. 30

5.3 The extracted GJ 1151 spectra from *XMM-Newton*'s MOS1 and MOS2 detectors (black and red crosses) are shown together with a two-temperature coronal plasma model fit (thick solid lines). The spectrum is very soft with an average coronal temperature of ca. 1.6 MK. 31

6.1 X-ray detections of known exoplanet host stars in the sky. Known planet host stars are depicted as small grey dots. The Kepler field at RA = 300 deg as well as the increased density of known planets along the ecliptic due to the coverage by the K2 mission are visible. Detections in the German eROSITA sky with the eRASS1 or eRASS2 survey are shown as filled red circles, previous detections with ROSAT, *XMM-Newton,* and *Chandra* are shown as filled black diamonds, open circles, and open squares, respectively. 40

6.2 X-ray to bolometric flux ratios of the exoplanet host stars in our sample vs their *Gaia* colour $G - R_p$; corresponding spectral types are given at the top of the figure. The horizontal dotted lines indicate the approximate upper and lower boundaries of typically observed flux ratios for main-sequence stars, with which our sample agrees well. 41

6.3 Fluxes of the X-ray detected stars in our sample in the soft X-ray band and the WISE W1 infrared band, large red dots for eRASS detections, and small black dots for all X-ray detections. The statistical dividing line between objects of stellar and non-stellar nature (Salvato et al., 2018) is shown as the solid grey line. The only source that falls into the non-stellar part of the parameter space is an exoplanet-hosting cataclysmic variable. 42

6.4 Simulated stellar coronal spectra using the eROSITA instrumental response. A single-temperature coronal plasma model was used with temperatures of 0.1, 0.4, and 1 keV (1.1, 4.6, and 11.4 million K). Almost all photons are emitted at energies below 2 keV even for very hot stellar coronae. 44

6.5 Hardness ratios HR1 and HR2 from simulated stellar coronal eROSITA spectra as a function of coronal temperature. HR2 is always close to -1, rising only very slightly for very high temperatures, and HR1 rapidly rises from low to moderate coronal temperatures and then saturates at a value of about 0.75 for temperatures above 0.5 keV. . . 45

6.6 Observed hardness ratio HR1 with 1σ uncertainties vs the *Gaia* $G - RP$ colour for the stars in our sample. The median hardness ratio, corresponding to a coronal temperature of about 0.3 keV, is depicted by the dashed line. The quite blue star to the left is the Herbig Be star HD 100546, a known X-ray emitter (Skinner & Güdel, 2020). . . 46

6.7 Nominal X-ray fluxes from eRASS1 vs optical brightness for stars in our sample. For stars with an apparent *Gaia* magnitude brighter than 4 mag, there is a clear trend towards high apparent eRASS fluxes, which can be attributed to optical loading. Some individual bright stars named in the plot can be expected to be only weak X-ray emitters because they are either lacking an outer convective envelope (β Pic) or are coronal graveyard-type giants (Ayres et al., 2003). Furthermore, these specific stars are known to be X-ray dim from previous observations by other X-ray telescopes. 48

6.8 Histogram of exoplanet host stars in distance bins of 5 pc (white with black outline) and the exoplanet host stars detected in the eRASS1 survey (red) in the German eROSITA sky out to a distance of 200 pc. The detection fraction is high with about 70% out to 20 pc and then drops off rapidly. A small number of X-ray detections exists for planet host stars at larger distances. 49

6.9 Comparison of soft X-ray fluxes in the 0.2-2 keV band for exoplanet host stars detected by more than one X-ray mission to fluxes detected by eRASS1. Stars detected by both eRASS1 and eRASS2 are shown in red. Some individual outliers are marked by name; these objects are expected to display strong variability in X-rays. 50

6.10 X-ray irradiation fluxes of exoplanets vs their orbital semi-major axis. The vertical spread represents the intrinsic luminosity distribution of the host stars. Transiting exoplanets are marked with open black circles; new eROSITA X-ray detections among them are additionally marked with a black cross. For guidance, the X-ray irradiation fluxes of known evaporating exoplanets, the hot Jupiter HD 189733 b and the warm Neptune GJ 436 b, are shown as horizontal dotted lines. . . 52

6.11 Estimated mass-loss rates of exoplanets in the energy-limited escape model (see text for details). The vertical spread represents the intrinsic luminosity distribution of the host stars. Transiting exoplanets, which are in principle accessible to follow-up observations to detect ongoing mass loss, are marked with open black circles; new eROSITA X-ray detections among them are additionally marked with a black cross. For guidance, the estimated mass-loss rates of known evaporating exoplanets, the hot Jupiter HD 189733 b and the warm Neptune GJ 436 b, are shown as horizontal dotted lines. 53

7.1 Histogram of the XUV flux at the planetary surface of exoplanets which are transiting their X-ray detected host stars (white with black outline). All exoplanets with host stars detected with eROSITA in the first two eRASS surveys are shown in solid grey, and the planets detected from the first time in X-rays by eROSITA are shown in striped blue. 66
7.2 Histogram of the estimated mass loss rates of X-ray detected exoplanets (white with black outline) and the exoplanets with host stars detected with eROSITA in the first two eRASS surveys (blue). 67
7.3 Density of planetary atmosphere of planets of differing masses in terms of the mass of WASP-10 b. The planets are with the same separation from their host star as that of WASP-10 b. Plot was adapted from Salz et al. (2016). 69
7.4 Toy model of an exoplanet (rocky core shown by the solid black circle) and its atmosphere. The atmosphere has decreasing density as the distance from the planetary surface increases (concentric blue circles around the planet). 71
7.5 Spectrum of a model star with a transiting planet (blue) compared to the spectrum of the same star when no planet is present (red). A magnification of the two largest peaks is shown in the subplot to highlight the change more clearly. 72
7.6 Model transmission spectrum of a star during the planetary transit of a planet with a mass that is 10% of the mass of WASP-10 b. Uncertainties are calculated for spectra with an accumulated exposure time of 100ks and a stellar X-ray flux of 10^{-12} erg/s/cm^2. 73

List of Tables

5.1 Fundamental physical parameters of the star GJ 1151. ^{a}Gaia Collaboration et al. (2018a) ^{b}Skrutskie et al. (2006) ^{c}Newton et al. (2017) ^{d}Bailer-Jones et al. (2018) 26
5.2 Best-fit parameters of the two-temperature coronal model to the MOS data. 29

6.1 Excerpt from the available electronic data table; the full table has additional columns and 343 rows. Radius superscript A denotes planets without measured radius values whose radii were estimated according to the mass-radius relationship by Chen & Kipping (2017). The same method was used to estimate planet masses with no measured value, which are denoted with superscript B in the electronic table. Superscript C for the X-ray flux denotes that the host star adopted X-ray flux and all entries derived from it were adjusted for unresolved bound stellar companions. The provenance of the used X-ray flux is given as E, R, X, and C for eROSITA, ROSAT, *XMM-Newton*, and *Chandra*, respectively. 61

1 Introduction to Exoplanets

Exoplanets are simply defined by NASA as "A planet orbiting a star other than our Sun". The first exoplanet around a main sequence star was discovered in 1995, when Mayor & Queloz (1995) detected 51 Peg b, a hot-Jupiter orbiting its host star with a period of 4.2 days. Since then, there have been 4935 exoplanets confirmed in 3706 different planetary systems (as of 3/3/2022)[1].

Due to biases in the most frequently used detection methods, most of the exoplanets discovered to date are in very close orbits to their host star. As a result, exoplanets experience very high irradiation levels from their host stars, and X-ray irradiation in particular can affect the planet's upper atmosphere, resulting in the evaporation of the atmosphere and mass-loss of the exoplanet, which will be discussed further in section 1.2.

1.1 Exoplanet Detection Methods

A number of different methods may be used to detect a planet outside of our solar system. In this section I will review the four different detection methods that have thus-so-far been most successfully used in exoplanetary science and the biases involved with them.

1.1.1 Radial Velocity

Mayor & Queloz (1995) reported the first exoplanet around a solar type star with the detection of 51 Peg, using the radial velocity method.

To use this method, a series of spectral observations are made of the host star. In the presence of an exoplanet, there may be detectable variations in the host star's spectrum, with the wavelengths of spectral lines increasing and decreasing periodically. This is due to the gravitational pull of the planet on the star. As the exoplanet orbits its host, it causes the star to also "wobble" slightly as it orbits the centre of mass between the planet and he star. This means that during the planetary orbit the star will move towards the observer and then away again at regular intervals. This causes a Doppler shift in the light reaching the observer, with the light being blue-shifted as the star moves towards us and the wavelength decreases, and then being red-shifted as the reverse occurs (see Fig. 1.1).

In addition to the detection of exoplanets, the radial velocity of a star may be used to determine the minimum mass for its planet. This can be done by assuming a value for the mass of the star and the inclination of the planet's orbit, as given by Butler et al. (2006) in:

$$M \sin i = K\sqrt{1-e^2}[\frac{P(M_* + M\sin i)^2}{2\pi G}]^{1/3}, \tag{1.1}$$

---

[1] `https://exoplanets.nasa.gov`

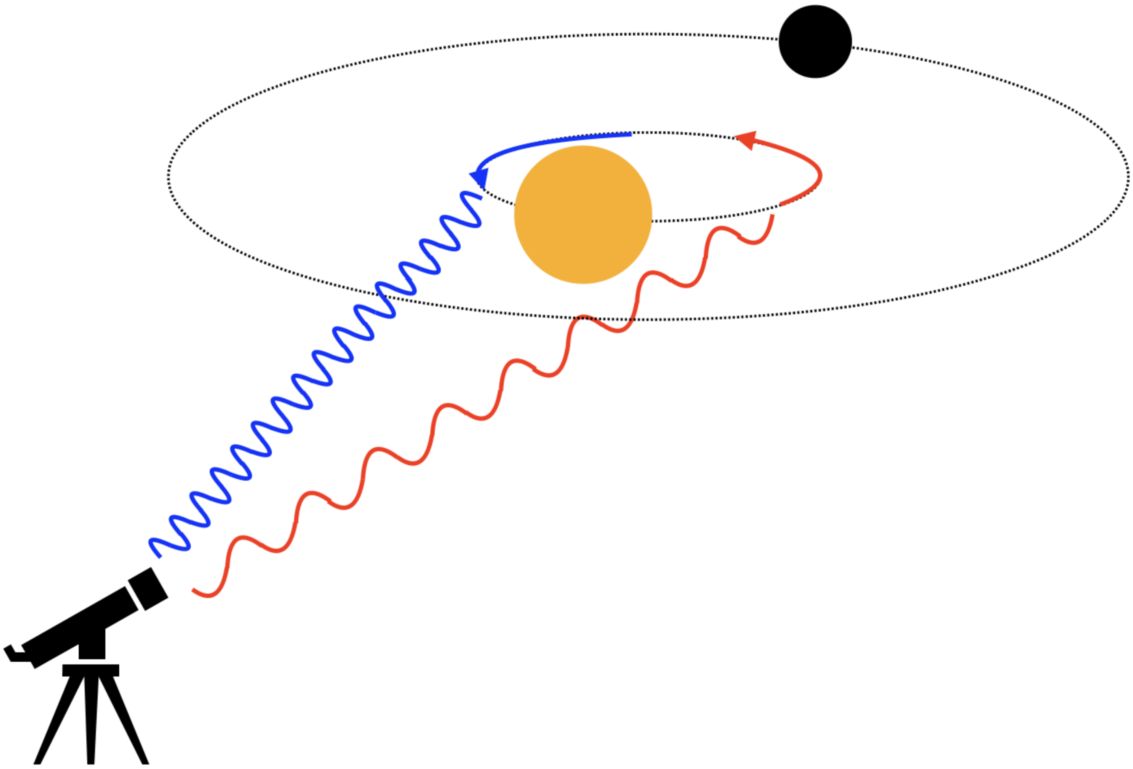

Figure 1.1: Simple illustration of the radial velocity method of detecting an exoplanet (black) orbiting its host star (yellow). The planet's gravitational pull on the host star causes the star to "wobble" which, in turn, causes the light from the star to appear slightly blue-shifted as the star moves closer to the observer in it's "wobble", and slightly red-shifted as the star moves away from the observer.

where i is the orbital inclination and $M \sin i$ is the minimum mass, K is the semi-amplitude of the reflex motion of the star (in ms^{-1}), e is the eccentricity of the planetary orbit, P is the planet's sidereal orbital period (in days), M_* is the mass of the host star, and G is the gravitational constant.

This effect is more pronounced for large, close-in exoplanets, such as hot Jupiters, as these have a greater gravitational pull on their host stars than smaller, further out planets such as those in our solar system. Therefore, the radial velocity method has a bias towards the detection of massive, close orbit exoplanets.

1.1.2 Microlensing

Microlensing is a useful detection technique for dim objects such as exoplanets. Microlensing involves repeatedly monitoring stars to detect the brightening that occurs when the dark planet passes between the observer on Earth and the source star in the distance. This brightening event occurs due to the star-planet system acting like a lens and its gravity bending and focusing the light from the distant source. This temporarily makes the light of the distant background star seem brighter to the observer. Once the lensing event is over, when the planet moves out of the observer's line of sight to the distant star, the star's brightness, as seen by the observer, returns to as it was before the microlensing event (Griest & Safizadeh, 1998).

An advantage of this method is that it can detect smaller planets and those in wider orbits than other methods such as the transit and radial velocity methods. However, it unfortunately is not repeatable as the alignment for the event to occur is by chance, and will not occur again.

1.1.3 Imaging

The direct imaging technique of planetary detection first provided an image of a planetary mass companion outside our solar system when Chauvin et al. (2005) reported the detection of 2M1207 b. Since this observation, a total of 55 exoplanets have been detected using this method[2].

For this technique to work, a coronagraph is used to prevent light from the exoplanet's host star being detected. This allows the light reflected off the planet, which is significantly dimmer than the light from the host star, to be observed and thus allows for astronomers to take an image of the exoplanet directly.

1.1.4 Transits

Finally, the most common way exoplanets are detected is through transits, with about 75% of planets being detected in this fashion. This method simply measures the dimming of the star when the exoplanet passes between its host star and the observer (Fig. 1.2). The photometric dimming of the star attributed to the passage of the planet across the stellar disk can be observed and allows a number of conclusions to be drawn about the planetary properties. Larger planets will block more light and the planetary transit (like the transit shown in Fig. 1.3) will be deeper for planets with larger radii. The radius of the planet can be calculated from its relative size compared to its host star. The planet's orbital period can also be found with this

---

[2] `https://exoplanets.nasa.gov/alien-worlds/ways-to-find-a-planet/`

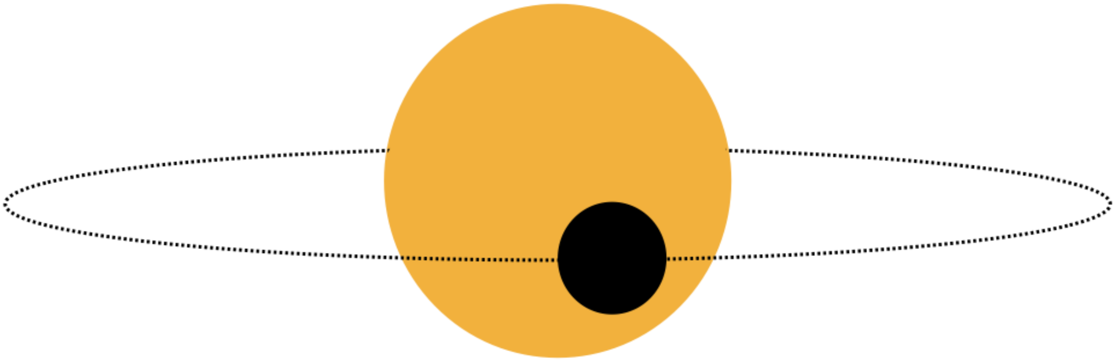

Figure 1.2: Simple illustration of an exoplanet (black) transiting its host star (yellow).

method by calculating the time between the planetary transits (Charbonneau et al., 2000).

The first planet to be detected in this manor was HD 209458 b (Charbonneau et al., 2000; Henry et al., 2000), whose transit light curve is shown in Fig. 1.3. Charbonneau et al. (2000) were able to confirm that this planet was a gas giant and estimated the radius to be $1.27R_{Jup}$. This planet is also the first with a detected atmosphere (Charbonneau et al., 2002). With this method, as the light from the planet's host star passes through the planetary atmosphere during a transit, certain wavelengths of light are absorbed more than others, corresponding to different elements and molecules in the exoplanet's atmosphere (see chapter 7 for a model of this effect).

The detection of planets via transits is the most relevant to our work with X-rays. A transit in X-rays is deeper due to the atmosphere being opaque at X-ray wavelengths and hence appearing larger than during observations at lower wavelengths, such as those is the visible energy range.

Of course, there are biases to detecting planets with this method. Much like with the radial velocity method, transit detection favour large, close-in exoplanets, for example hot Jupiters, around smaller stars. This is because the smaller the relative size difference between the planet and its host, the larger the transit light curve, allowing for easier detection.

Although there are a number of other exoplanet detection methods, such as pulsar timing and astrometry, these will not be discussed further in this work.

1.2 Mass-Loss

As discussed in section 1.1 our solar system is likely slightly unusual in its planetary distances to the Sun; with many thus-so-far discovered exoplanets being much closer to their host stars then even Mercury is to our own. This is due to the detection biases discussed earlier in this chapter. This means that these exoplanets receive much higher levels of irradiation from their host stars than we do from our Sun. This intense radiation is a driving factor in the inflation of hot Jupiters. High-energy irradiation, such as UV and X-ray irradiation, of an exoplanet's atmosphere can drive hydrodynamic evaporation. This intense radiation can cause the gas in the

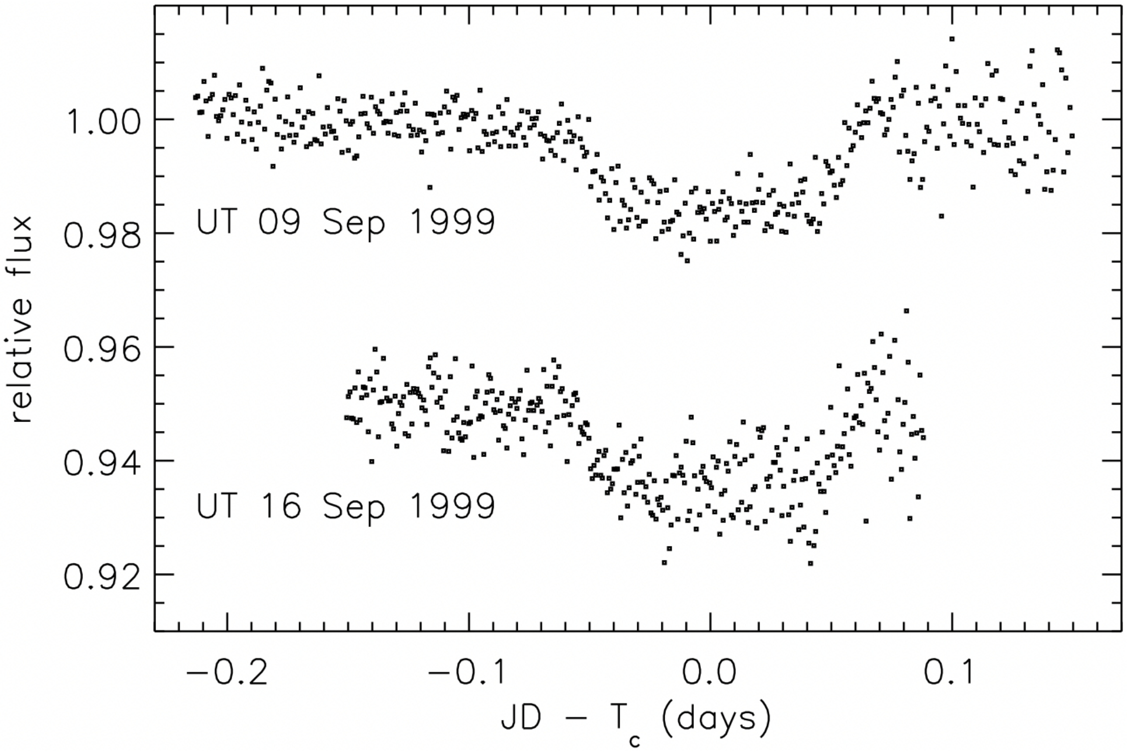

Figure 1.3: Transit curve of HD 209458 b from Charbonneau et al. (2000). The transits were observed a week apart and plotted as a function of time from the centre of the transit, T_c. The larger scatter in the data from 16/9/1999 (bottom) is due to the shorter exposure time compared to that on 9/9/1999 (top).

exoplanet atmospheres to expand and be lifted out of the gravitational well of the planet, causing the atmosphere to evaporate (Fortney & Nettelmann, 2010; Baraffe et al., 2010; Watson et al., 1981; Owen & Jackson, 2012).

In general, a planet's atmospheric evaporation is thought to be driven by soft X-rays and extreme-ultraviolet (EUV) radiation received by the planet from its host star. While this EUV component is not currently observable, there are a number of different instruments that can observe the X-ray part of the spectrum; the instruments important to this work are summarised in chapter 3 (Yelle, 2004; Murray-Clay et al., 2009).

The mass loss rate of a planet's atmosphere can be calculated with a simple energy-limited hydrodynamic escape model based on Lopez et al. (2012) and Owen & Jackson (2012):

$$\dot{M} = \epsilon \frac{\pi R_{XUV}^2 F_{XUV}}{KGM_{pl}/R_{pl}}, \tag{1.2}$$

where where $\dot{M}$ is the mass loss rate, ϵ is the efficiency of the atmospheric escape, G is the gravitational constant, K the effect of Roche-lobe overflow, F_{XUV} is incident the XUV flux on the planet, M_{pl} is the planet's mass, R_{XUV} is the planetary radius at XUV wavelengths and R_{pl} is the optical radius of the planet. This equation is used to estimate the mass loss rates of exoplanets with X-ray observed host stars in chapter 7, where atmospheric mass loss is also discussed in context.

2 Introduction to Host Stars

In addition to driving the atmospheric mass-loss of exoplanets (see section 1.2), X-rays are vital to the study of the planet hosting star. Stellar wind physics and coronal properties such as temperature are in turn important components to the interactions between the star and its planets. In this section, we will discuss the stellar corona and the star-planet interactions it effects.

2.1 Stellar Atmosphere

A cool star's internal structure, working outwards, is made up of the inner radiative zone and the outer convective zone, which is surrounded by the stellar atmosphere. This atmosphere is the observable layer of the star. Made up of extremely hot plasma, the atmosphere is the source of "space weather" conditions from which particles are released into space.

The atmosphere itself can be further divided into layers. The innermost, and also the coolest layer of a star's atmosphere is the photosphere. Beyond this lies the chromosphere, where the atmosphere begins to heat up, followed by the transition region, a thin region where the temperature rises rapidly. A star's corona is the outermost layer of its atmosphere. In cool stars, stellar corona are the origin of X-rays, making the corona the focus of this work on the X-ray studies of star-planet systems.

2.2 Stellar Corona

The corona is observable at X-ray wavelengths and thus X-ray studies of stars are critical to the study of coronal properties. This plasma layer is controlled by the magnetic fields of the star, and is the source of stellar winds, flares and coronal mass ejections (Schmitt, 1997).

Stellar winds are made up of charged particles which flow out of the star, interacting with its magnetic field and each other. The dense plasma in the lower corona is trapped in static equilibrium. However, outside of these pockets the solar wind can flow along the open magnetic field into space. In general, the hot corona tends to expand into the the solar wind (see Fig. 2.1).

Flares are triggered by magnetic energy being released on the star. This release of energy causes a rapid and energetic burst of particles called a flare as the magnetic field lines readjust themselves to a more stable configuration and reconnect. The reconnection likely takes place in the lower atmosphere and the interior of the star, and causes the region around where the process occurs to heat the plasma to tens of MK. The energy propagates along a magnetic loop from the corona to the chromosphere where the material is heated and expands into the corona, filling existing coronal

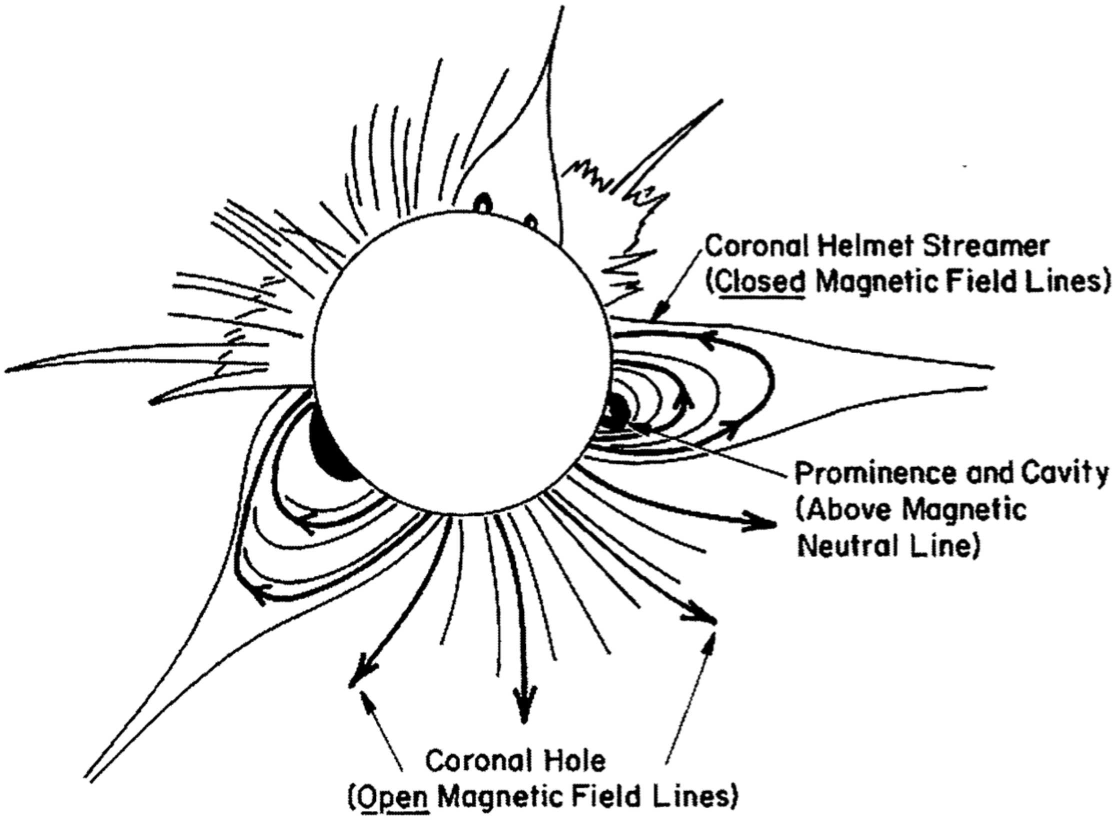
Coronal Helmet Streamer
(Closed Magnetic Field Lines)
Prominence and Cavity
(Above Magnetic
Neutral Line)
Coronal Hole
(Open Magnetic Field Lines)

Figure 2.1: A sketch of the magnetic field of the solar corona from Low (1996) showing the open magnetic field lines, along which the solar winds are carried into space. This figure also shows the closed magnetic fields lines where plasma is trapped due to the high electrical conductivity conditions.

loops and causing them to expand and expel the magnetic forces in a coronal mass ejection (Benz, 2008).

Coronal mass ejections are clouds of plasma and magnetic field lines which, after a stellar eruption, are released from the star into space. As they travel through space and expand, coronal mass ejections can interact the magnetic fields of planets and cause geomagnetic storms. These coronal mass ejections may lead to the reconnection conditions necessary for causing a flare. Coronal mass ejections and flares are the two most energetic phenomena that occur in the stellar corona (Low, 1996; Benz, 2008).

2.3 Stellar X-rays

X-rays can be produced and emitted by stars in a number of different ways depending on the characteristics of the star.

For hot stars, which I mention here for completeness, that have no stellar convection zones and hence no magnetic dynamo, hydrodynamic shocks are formed due to the unstable stellar winds being shed. The X-rays from these stars originate from these shocks and the stellar winds project them out across large radii into space. This is a similar process to the occurrences in binary stars, where there are colliding winds causing these shocks and emitting the X-rays (Güdel, 2002).

However, in stars with a magnetic dynamo (see section 2.4), it is this dynamo which is the origination of the X-rays from that star, as discussed further in the next section. Cool stars, such as flaring M-dwarfs, which are commonly detected planetary host stars, fall into this category.

2.4 Magnetic Dynamo

The presence of a stellar corona implies the existence of a stellar magnetic dynamo. The magnetic dynamo is produced by the stellar rotation interacting with the convection and begins at the bottom of the convection zone. The magnetic field produced is the cause of the magnetic incidences in the stellar atmosphere, such as stellar flares in the star's corona (Güdel & Nazé, 2009).

As these stars have an internal dynamo which is induced by the stellar rotation, the X-ray luminosity of a star is related to its rotation as given by Güdel & Nazé (2009):

$$L_X \approx 10^{27}(v \sin i)^2, \tag{2.1}$$

$$L_X \propto \Omega^2 \propto P^{-2}, \tag{2.2}$$

$$F_X, \frac{L_X}{L_{bol}} \propto Ro^{-2}, \tag{2.3}$$

where L_X is the X-ray luminosity ($ergs^{-1}$), $v \sin 1$ is the projected rotation period, Ω is the rotation rate, P is the rotation period, F_X is the X-ray flux, L_{bol} is the bolometric luminosity and Ro is the Rossby number, or the rotation period divided by the convective turnover time. Therefore, faster rotation of the star drives more activity, up until the magnetic fields are too strong and cover the entirety of the stellar surface, at which point the activity is saturated (Güdel & Nazé, 2009; Mohanty & Basri, 2003). The magnetic activity of the star can be altered by the presence of a planet orbiting its host.

This stellar dynamo is the driver of the magnetic field, which is, in turn, the driver of stellar flares and the heating of plasma to the coronal temperatures. Importantly for this work, we can use X-ray observations to predict the coronal temperature of a star. Johnstone & Güdel (2015) reports that the coronal temperature ($\bar{T}_{corona}$)in MK can be calculated from the observed X-ray flux (F_x) in $ergs^{-1}cm^{-2}$ simply using the relation:

$$\bar{T}_{corona} = 0.11F_X^{0.26}. \tag{2.4}$$

The temperature of the corona is necessary to verify the conditions for interactions, such as sub-Alfvénic interactions, to occur (see chapter 5). These sub-Alfvénic interactions are discussed further in subsection 2.5.2.

2.5 Star-Planet Interactions

Star-planet interactions are suspected to be able to alter stellar magnetic activity in a variety of ways. Exoplanets in close orbits to their host star can affect their host stars under two main mechanisms:

- tidal interactions and
- magnetic interactions.

2.5.1 Tidal Interactions

Tidal interactions are caused by nearby planets as a result of gravitational acceleration. These interactions occur when a giant planet raises tides on its host star and vice-versa. These tides can affect the star under certain conditions, such as if the stellar spin has a different period than the planetary orbit (Poppenhaeger, 2019).

In an *equilibrium tide* it is assumed that the star is in hydrostatic equilibrium. These tides are induced by the stellar structure hydrostatically readjusting due to a perturbing potential, which, for our purposes, will hereafter be referred to as the planet. An equilibrium tide occurs when the orbiting exoplanet has a shorter orbital period than the host star's rotation period. The tidal lag in these cases, raised on the star by the planet, is behind the planet as it orbits the star, causing the gravitational pull the planet has on the bulge to transfer angular momentum to the stellar spin from the planetary orbit. These equilibrium tides can be divided into two components: the adiabatic system and the dissipative system (see Fig. 2.2).The adiabatic tide ignores any dissipative processes when calculating the hydrostatic response to the planet and this adiabatic component is in phase with the tide, whereas the dissipative component is perpendicular to the phase of the tide and is due to the star's response to dissipative processes such as thermal dissipation and turbulent friction in convective regions (Zahn, 2008; Remus et al., 2012; Bolmont et al., 2017).

In addition to the equilibrium tide, *dynamical tides* are a part of tidal interactions. These tides are driven by Coriolis acceleration and have two main causes. The first

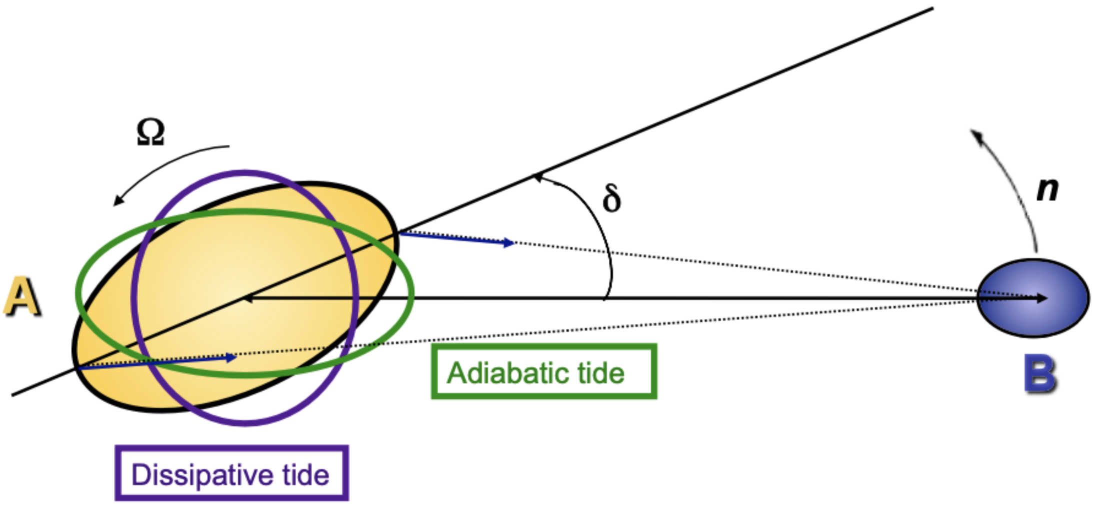

Figure 2.2: A typical tidally interacting system from Remus et al. (2012). Here a planet, B, is interacting with the star, A, and exerting a tidal force. The star adjusts itself with a phase lag, δ, due to internal friction. The adjustment is broken into to an adiabatic component and a weaker, dissipative one.

is when inside the convective envelope of the star, the inertial waves, which are driven by the Coriolis acceleration, propagate. The second cause of dynamical tides is when gravity waves in the radiative core of the star become inertial waves once affected by the Coriolis acceleration. This dynamical tide is what constitutes the wavelike component of the tidal interaction (Bolmont et al., 2017; Benbakoura et al., 2019).

2.5.2 Magnetic Interactions

The second mechanism in which exoplanets may interact with their host stars is magnetic interactions. These are the interactions between the magnetic fields of the star and its planetary companion. There are a number of different ways in which magnetic interaction may occur:

- by suppressing the stellar wind, which in turn prevents the stellar magnetic loops from opening (Cohen et al., 2010),
- by triggering stellar flares near the sub-planetary point (Lanza, 2018; Fischer & Saur, 2019),
- through the re-connection of the stellar and planetary field lines (Cuntz et al., 2000; Shkolnik et al., 2005; Lanza, 2008) and
- through sub-Alfvénic interactions.

For this work, we focus on the final of these four, sub-Alfvénic interactions, as the mechanism by which an exoplanet and its host star interact.

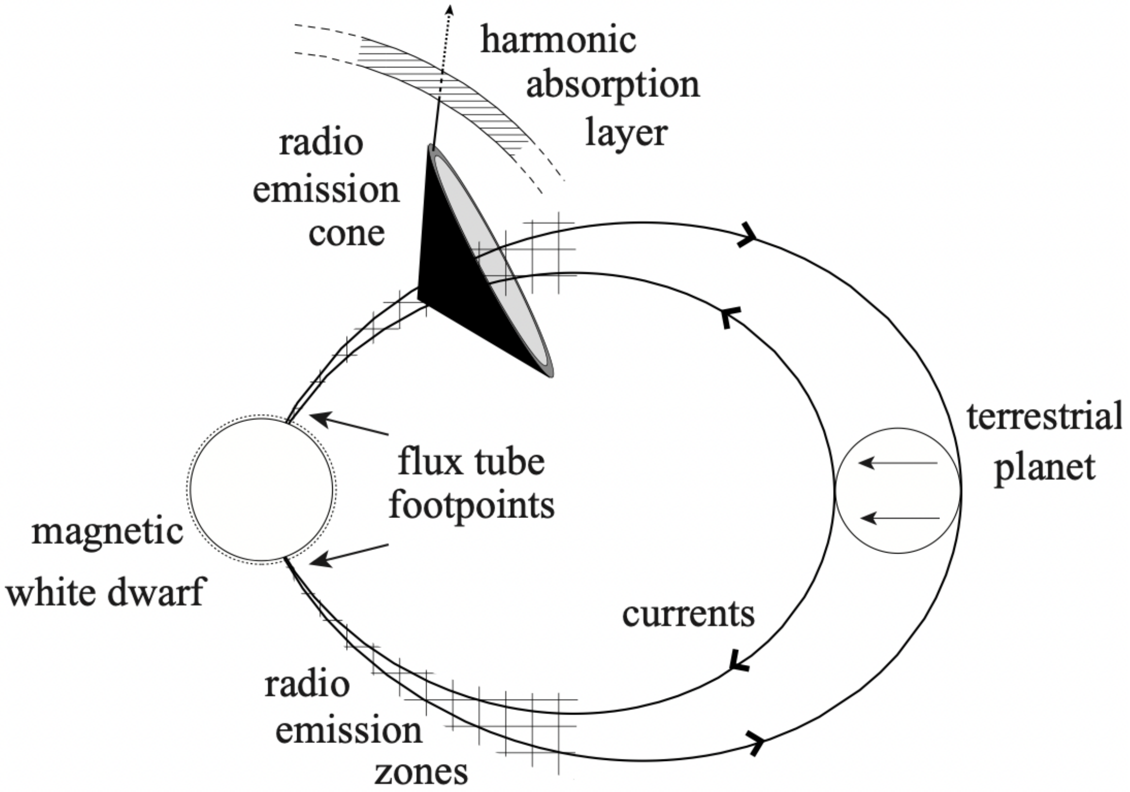

Figure 2.3: An uni-polar inductor model for a white-dwarf system from Willes & Wu (2005). A cone of radio emission is being generated by the sub-Alfvénic interaction, and is then dragged around by the exoplanet.

Sub-Alvénic Interaction

Sub-Alfvénic interactions are a scaled-up, partial analogue to the Jupiter-Io system interaction. In this interaction, the heated regions in the star's outer atmosphere track the orbit of the planet due to the nature of the interaction. This occurs when the planetary body orbits within the star's magnetosphere, so that the planet is an obstacle to the plasma flow. Alfvénic waves are then generated subsequent to the plasma flow and the waves propagate along the magnetic field, which in turn generate radiative energy and heat the plasma. This process can be seen in Fig. 2.3 for a terrestrial planet orbiting a magnetic white dwarf (Willes & Wu, 2005).

This process can explain the "on and off" type of radio emission as observed by Vedantham et al. (2020). The radio emission is only visible when the so called "cone" of emission (shown in Fig. 2.3) is not blocked from our field of view by the star itself. The variable radio emission observed by Vedantham et al. (2020) is shown in Fig. 2.4.

Importantly, for this Jupiter-Io like scenario, a low coronal temperature is necessary. The planet needs to be moving through a certain point in the the stellar wind where it streams out. A low temperature is important because it allows us to make assumptions about the stellar wind velocity, which in turn is important for sub-Alfvénic star planet interaction. Vedantham et al. (2020) used the X-ray non detection of GJ 1151 to assume an low ambient coronal temperature of 2 million kelvin. This would allow the variable radio emission shown in Fig. 2.4 to be ex-

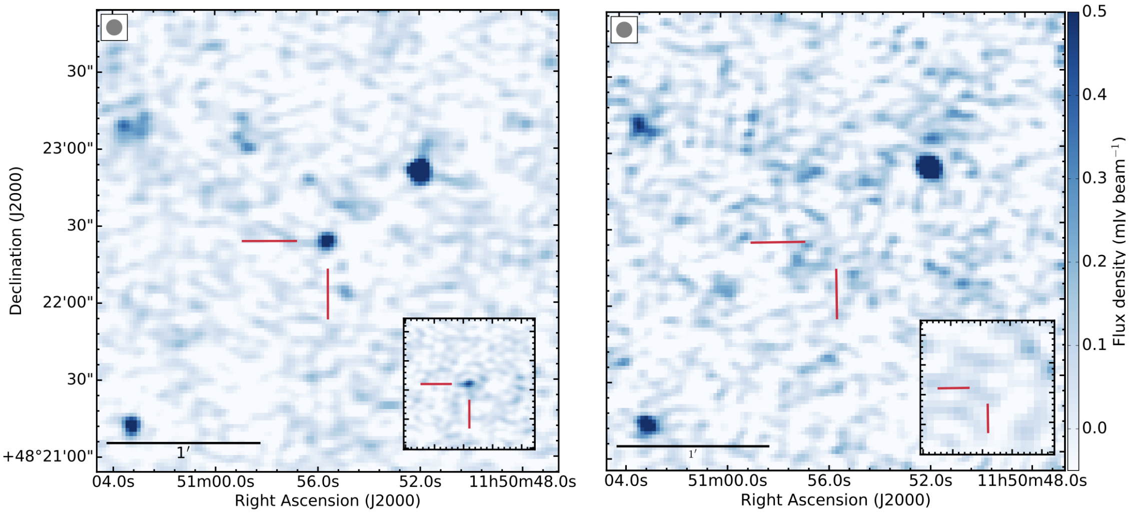

Figure 2.4: Radio image of GJ 1151 (denoted by the red cross-hairs) from Vedantham et al. (2020). The images were takes at two different epochs; 16 June 2014 and 28 May 2014 shown on the left and right respectively, with the star being visible at radio wavelengths in the left panel and not the right.

plained by sub-Alfvénic star planet interaction. X-ray results to confirm the coronal temperature and this assumption can be found in chapter 5.

3 X-ray observatories

Observed and simulated data from the following X-ray observatories were used throughout this work:

- ROSAT (1990-1999),
- Chandra (1999-present),
- XMM-Newton (1999-present),
- eROSITA (2019-present),
- Athena (planned launch in 2031).

This section will summarise the instruments listed above for those unfamiliar with these X-ray observatories.

3.1 ROSAT

Launched in 1990, ROSAT's primary mission was to perform the first all-sky survey in the X-ray regime. ROSAT's X-ray telescope (XRT) carried three focal plane instruments; two Position Sensitive Proportional Counters (PSPC) and the High Resolution Imager (HRI), on board. The XRT was sensitive to the X-ray energy range between 0.1 and 2.4 keV, which is most relevant to the work in chapter 7. The PSPC, which performed the ROSAT all-sky survey (RASS), was shut down in 1994 to conserve the detector gas which remained. However, in September 1998, the HRI was severely damaged when the telescope accidentally performed a slew near the Sun, and in December that year the PSPC was put back into the focal plane of the XRT[1]. In addition to the XRT, the ROSAT satellite also carried a smaller extreme ultraviolet (EUV) telescope which was sensitive to the 25 to 100 eV energy band (Truemper, 1982, 1993; Predehl & Schmitt, 1995; Schmitt, 1997).

In the all sky survey RASS, performed by the PSPC, the sky was scanned in great circles perpendicular to the ecliptic. These circles had a width of 2° and were perpendicular to the solar direction which meant that the cumulative exposure time was around 400s at the ecliptic equator and there was a much longer exposure time of around 40,000s at the ecliptic poles as seen in Fig. 3.1. This survey was performed during the first six months of the ROSAT mission in 1990 and 1991. A second analysis of the RASS data done between 1994 and 1995 detected 145,060 sources (Voges et al., 1996, 1999, 2000).

The second phase of the mission was dedicated to observations in the pointed mode, where detailed observations were made of selected sources . This phase lasted

---

[1] `https://heasarc.gsfc.nasa.gov/docs/rosat/rosat_history.html`

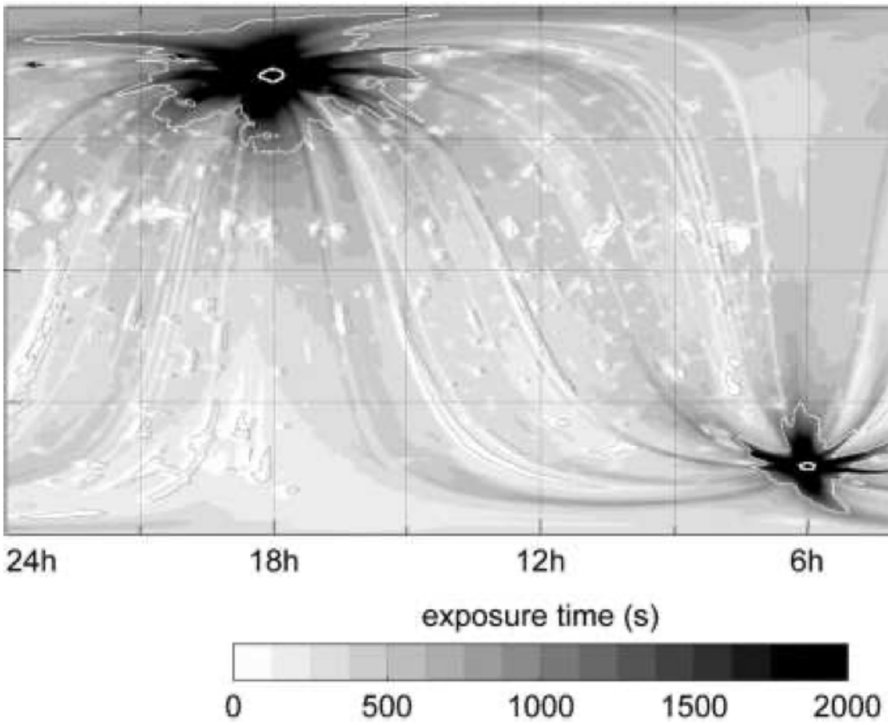
24h
18h
12h
6h
0h
exposure time (s)
0
500
1000
1500
2000

Figure 3.1: Exposure map from Voges et al. (1999). This map comes from the second processing of the RASS data. Due to the way RASS scans the sky, there is a higher exposure at the ecliptic poles than at the ecliptic equator. Note that the white spots represent locations where there were not enough guide stars for the satellite's automatic measuring system.

until the ROSAT observatory was deactivated in 1999 (Böhringer et al., 2001; Predehl et al., 2021).

Schmitt et al. (1995) provided the first X-ray survey of low mass stars (spectral type K and M) in the solar neighbourhood. Here the authors also provided a counts to flux conversion formula which is discussed in greater detail in chapter 7.

3.2 Chandra

Chandra is an X-ray observatory launched in 1999. Within the Integrated Science Instrument Module (ISIM) on-board, there is a X-ray imaging detector called the High-Resolution Camera (HRC). The image resolution of the High Resolution Mirror Assembly (HRMA) and the HRC combined is better than $1''$. The telescope itself is sensitive to an energy range of 0.1 keV to 10 keV; with the High Energy Transmission Grating Spectrometer (HETGS) being sensitive to an energy range of 0.4 to 10 keV and the Low Energy Transmission Grating Spectrometer (LETGS) sensitive to a range of 0.08 to 2 keV[2] (Weisskopf et al., 1995; Kraft et al., 2000).

The HETGS and LETGS can be used in conjunction with the X-ray imager the Advanced CCD Imaging Spectrometer (ACIS) for high resolution spectroscopy. However, the ACIS can also be used on its own for spectroscopy with moderate resolution. Importantly, the ACIS also allows for high resolution imaging of about 1 arcsecond. This is possible by the recording of the energy, arrival time and positions of the individually detected photons hitting the ACIS[3].

3.3 XMM-Newton

XMM-Newton is an X-ray observatory, which like Chandra launched in 1999. For the purpose of this work (see chapter 5), when talking about XMM-Newton we are specifically referring the European Photon Imaging Camera (EPIC). EPIC comprises of two MOS (Metal Oxide Semi-conductor) CCD arrays (hereafter referred to as the MOS1 and MOS2 cameras, or together simply MOS). and a pn CCD referred to as the pn camera. These EPIC cameras operate in the energy range from 0.15 to 15 keV. The MOS cameras have a useful quantum efficiency in the energy range 0.2 to 10 keV, whereas the more sensitive pn camera has a high efficiency detecting photons up to 15 keV[4].

These EPIC instruments are not only sensitive to X-rays, but also to infrared, visible and ultraviolet light. In order to minimise the contamination of the X-ray signal from this light, the EPIC cameras include optical blocking filters called the thin, medium and thick filters, which each block more contamination than the previous filter.

For the sake of completeness, I would like to mention the other scientific instruments on-board XMM-Newton in addition to the EPIC cameras. These include an array of reflecting gratings called the Reflection Grating Spectrometers (RGS) which diffract X-rays onto an array of CCD detectors. The RGS allows for high resolution

---

[2] `https://chandra.harvard.edu/about/science_instruments.html`

[3] `https://cxc.harvard.edu/cal/Acis/`

[4] `https://www.cosmos.esa.int/web/xmm-newton/technical-details-spacecraft`

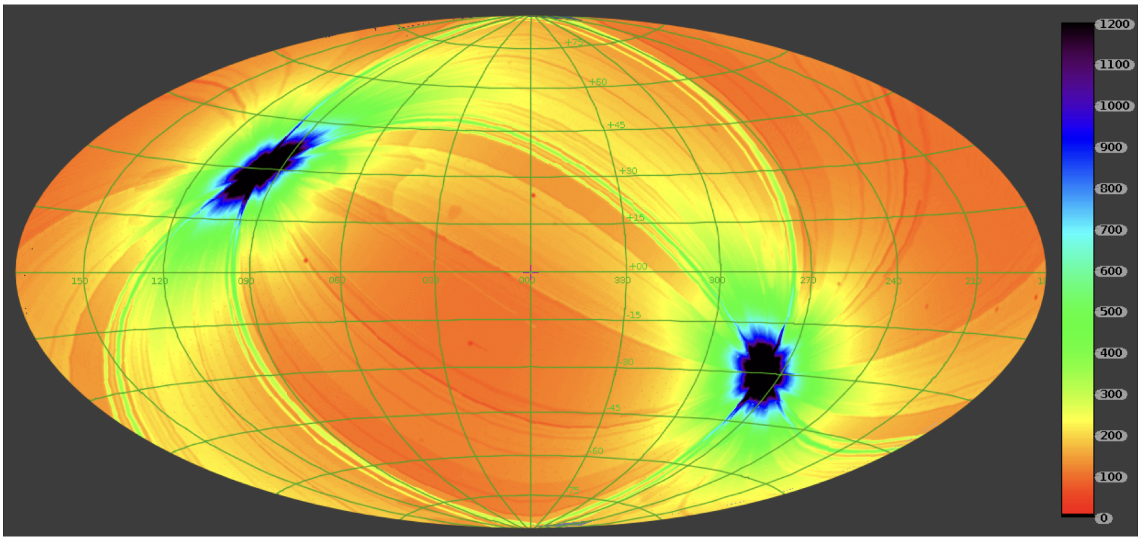

Figure 3.2: Effective exposure map from Predehl et al. (2021). This map is derived from eRASS1, the first eROSITA all-sky survey. The effective exposure values range from 100s at the ecliptic equator to more than 10 000s close to the ecliptic poles.

measurements to be taken in the soft X-ray range of 0.3 to 2.1 keV and is optimised for the detections of carbon, nitrogen, oxygen, neon, magnesium, and silicon, and iron (den Herder et al., 2001). Lastly, XMM-Newton also carries an Optical/UV Monitor (OM) telescope. The OM covers a square region of 17 arc minutes in the centre of the X-ray field of view, allowing for observations of XMM-Newton targets in the UV and optical bands simultaneously alongside those taken in the X-ray bands.

3.4 eROSITA

Launched in 2019, the joint Russian and German mission, the Spectrum Roentgen Gamma (SRG), carries the primary instrument, eROSITA on board. The instrument consists of seven mirror systems and is sensitive to the soft X-ray regime.

eROSITA is producing the eROSITA All-Sky Survey (eRASS) over four years, the first survey of its kind in X-rays since the ROSAT mission in the 1990s. This survey will consist of eight independent X-ray maps, one produced every six months over the four years of continuously scanning the sky. The survey works by performing parallel scans in alternating directions which are offset by 6’ so that each position in the sky is observed in ten consecutive scans (given the eROSITA field of view has a diameter of one degree). Much like the ROSAT sky survey (exposure map shown in Fig. 3.1), the eROSITA sky survey has an exposure time that is a hundred times longer at the ecliptic poles than at the ecliptic equator, as shown in Fig. 3.2. The all-sky survey produced by eROSITA will be about 25 times more sensitive in the soft X-ray band (0.2–2.3 keV) than the ROSAT All-Sky Survey and the hard band (2.3–8 keV) true imaging survey of the sky will be the first of its kind.

At the time of writing of chapter 6, the first two eROSITA all-sky surveys (eRASS1 and eRASS2) had available data which were considered for this project. More information on the eROSITA instrument and these surveys can be found in chapter 6 and chapter 7 (Brunner et al., 2021; Predehl et al., 2021; Sunyaev et al., 2021).

3.5 Athena

The Advanced Telescope for High Energy Astrophysics (Athena) mission, is an X-ray observatory currently scheduled to launch in 2031[5] (Barret et al., 2020). This instrument is summarised in chapter 7.

---

[5] `https://sci.esa.int/web/athena/-/59896-mission-summary`

4 Overview of the included manuscripts

Manuscript I: "The corona of GJ 1151 in the context of star-planet interactions", Monthly Notices of the Royal Astronomical Society: Letters, Volume 497, Issue 1, Pages 1015–1019, July 2020.

Authors: G. Foster[1,2], K. Poppenhaeger[1,2], J. D. Alvarado-Gómez[1] and J.H.M.M. Schmitt[3]

[1]Leibniz Institute for Astrophysics Potsdam (AIP), An der Sternwarte 16, 14482 Potsdam, Germany
[2]Universität Potsdam, Institut für Physik und Astronomie, Karl-Liebknecht-Straße 24/25, 14476 Potsdam, Germany
[3]Universität Hamburg, Hamburger Sternwarte, Gojenbergsweg 112, 21029 Hamburg, Germany

Contribution: I, G. Foster, was the first author on this paper entitled "The corona of GJ 1151 in the context of star-planet interactions". As the first author, I contributed the bulk of the analysis and body of the work. My contribution included extracting the spectra and the analysis for the coronal temperature as discussed in the manuscript given in chapter 5.

Other significant contributions came from K. Poppenhaeger who also wrote parts of the body of the paper and helped with the analysis of the spectra and light curve.

J. D. Alvarado-Gómez and J.H.M.M. Schmitt both provided valuable scientific input and advice about magnetic interaction and X-rays in the context of this work.

In the context of this thesis: this manuscript discusses the effect of star-planet interactions on the planetary host star GJ 1151 and uses X-ray observations to confirm the coronal conditions for these scenarios to occur.

Manuscript II: "Exoplanet X-ray irradiation and evaporation rates with eROSITA", Astronomy & Astrophysics. Accepted 21 June 2021 for publication in "The Early Data Release of eROSITA and Mikhail Pavlinsky ART-XC on the SRG mission" special issue.

Authors: G. Foster[1,2], K. Poppenhaeger[1,2], N. Ilic[1,2] and A. Schwope[1]

[1]Leibniz Institute for Astrophysics Potsdam (AIP), An der Sternwarte 16, 14482 Potsdam, Germany
[2]Universität Potsdam, Institut für Physik und Astronomie, Karl-Liebknecht-Straße 24/25, 14476 Potsdam, Germany

Contribution: I, G. Foster, was the first author on this paper entitled "Exoplanet X-ray irradiation and evaporation rates with eROSITA". As the first author, I contributed the bulk of the analysis and body of the work. My contribution most importantly included the conversions and analysis of the X-ray stellar flux and mass-loss rates of exoplanets and the published catalogue that goes alongside this paper (chapter 6).

K. Poppenhaeger provided invaluable contributions with work on the eROSITA data, such as the hardness ratios, optical loading and advising me with in using the new eROSITA data in a useful way. In addition, Prof. Dr. Poppenhaeger helped with the identification of interesting follow up targets which were eventually included in this work and provided some of the text for this paper.

N. Ilic provided information of stellar binary systems so that the X-ray flux at a position could be more correctly attributed to the correct star.

A. Schwope provided valuable input on the eROSITA data and X-rays.

In the context of this thesis: this manuscript uses new eROSITA X-ray data alongside archival ROSAT, XMM-Newton and Chandra data to create a X-ray catalogue of planet hosting stars. The X-ray flux incident on an exoplanet from its host star is calculated where possible and used to estimate and record the mass-loss rate of the exoplanet atmospheres.

Manuscript III: "Identifying interesting planetary systems for future X-ray observations", Astronomishe Nachrichen. Accepted 21 January 2022 for publication in the proceedings special issue "A high-energy view of exoplanets and their environments".

Authors: G. Foster[1,2] and K. Poppenhaeger[1,2]

[1]Leibniz Institute for Astrophysics Potsdam (AIP), An der Sternwarte 16, 14482 Potsdam, Germany
[2]Universität Potsdam, Institut für Physik und Astronomie, Karl-Liebknecht-Straße 24/25, 14476 Potsdam, Germany

Contribution: I, G. Foster, was the first author on this paper entitled "Identifying interesting planetary systems for future X-ray observations". As the first author, I contributed the analysis and body of the work in chapter 7.

K. Poppenhaeger offered valuable advice and input on both the analysis and text of this work.

In the context of this thesis: this manuscript identifies interesting exoplanet systems for observations with modern and future X-ray observatories. These systems are those where an exoplanet is both transiting its host star and highly irradiated and therefore may be undergoing currently observable atmospheric mass loss.

This work also simulates spectra from the future Athena mission to predict what future exoplanetary transit observations will look like. Here we model the transmission spectrum for a hot Jupiter to show that future missions will be able to use X-ray observations to identify the absorption of outer exoplanet atmospheres.

5 The corona of GJ 1151 in the context of star-planet interaction

5.1 Abstract

The low-mass star GJ 1151 has been reported to display variable low-frequency radio emission, which has been interpreted as a signpost of coronal star-planet interactions with an unseen exoplanet. Here we report the first X-ray detection of GJ 1151's corona based on XMM-Newton data. We find that the star displays a small flare during the X-ray observation. Averaged over the observation, we detect the star with a low coronal temperature of 1.6 MK and an X-ray luminosity of $L_X = 5.5 \times 10^{26}$ erg/s. During the quiescent time periods excluding the flare, the star remains undetected with an upper limit of $L_{X,qui} \leq 3.7 \times 10^{26}$ erg/s. This is compatible with the coronal assumptions used in a recently published model for a star-planet interaction origin of the observed radio signals from this star.

5.2 Introduction

Star-planet interactions are suspected to be able to alter stellar magnetic activity in a variety of ways. Tidal interaction may influence the rotational evolution and therefore the magnetic activity level of a host star, similar to tidal synchronization in close stellar binaries, or may influence convection in the outer layers of the star (Cuntz et al., 2000; Pont, 2009; Pillitteri et al., 2014). Magnetic interaction is thought to be able to manifest itself through processes like reconnection of stellar and planetary field lines (Cuntz et al., 2000; Shkolnik et al., 2005; Lanza, 2008), suppression of the stellar wind by preventing stellar magnetic loops from opening up (Cohen et al., 2010), triggering of stellar flares near the sub-planetary point (Lanza, 2018; Fischer & Saur, 2019), or sub-Alfvénic interaction, similar to the interaction seen in the Jupiter-Io system (Goldreich & Lynden-Bell, 1969). In cases such as the Jupiter-Io interaction, where a planetary body is an obstacle in the flow of the plasma, Alfvénic waves are generated subsequent to the flow. The waves propagate along the magnetic field generating radiative energy, causing heating of the plasma (Gosling et al., 1982; Saur et al., 2013; Strugarek et al., 2014; Turnpenney et al., 2018).

Observational studies have reported some hints for tidal and magnetic interactions (Shkolnik et al., 2005; Pont, 2009; Kashyap et al., 2008; Poppenhaeger & Wolk, 2014; Maggio et al., 2015; Cauley et al., 2018), but also caveats have been pointed out with respect to biases from planet-detection methods which may skew activity distributions in planet host samples (Poppenhaeger et al., 2010; Miller et al., 2015). The intrinsic variability of stellar activity on short and long time scales, such as

Table 5.1: Fundamental physical parameters of the star GJ 1151. [a]Gaia Collaboration et al. (2018a) [b]Skrutskie et al. (2006) [c]Newton et al. (2017) [d]Bailer-Jones et al. (2018)

Parameter	Value
Gaia DR2 ID	786834302079285632[a]
2MASS ID	J11505787+4822395[b]
G (mag)	11.694[a]
J (mag)	8.488[b]
H (mag)	7.952[b]
K (mag)	7.637[b]
mass	0.167 $M_\odot$[c]
radius	0.190 $R_\odot$[c]
distance	8.036 ± 0.008 pc[d]

flares or stellar activity cycles, makes an unambiguous attribution of stellar activity changes to a planetary origin challenging.

GJ 1151 is a low-mass star located in the solar neighbourhood; we list its basic physical parameters in Table 5.1. The star was observed to display variable radio emission (Vedantham et al., 2020) with LOFAR (van Haarlem et al., 2013). Several scenarios for a purely stellar origin of the radio emission were excluded, and Vedantham et al. (2020) concluded that sub-Alfvénic star-planet interaction with a so far undetected small planet in a close orbit is the most likely explanation for the observed radio signatures.

Here we report on the first X-ray detection of GJ 1151, and we present an analysis of the star's coronal properties in the context of star-planet interaction.

5.3 Observations and data analysis

The star GJ 1151 was observed with *XMM-Newton* on 1st November 2018 for 12 ks (ObsID 0820911301, PI J. Schmitt). The observations used the medium filter and full frame mode for all three CCD detectors (MOS1, MOS2, and PN). We analysed the data using XMM's SAS software version 18.0.0. We followed the standard data reduction steps outlined in the XMM SAS users guide[1], i.e. we filtered out bad-flag photon events and screened for times of high background using the full-chip high-energy count rates. Only the PN detector displayed significant time portions of high background. The MOS detectors displayed only such short time stretches of slightly elevated background that we opted to analyse the continuous MOS data, in order to facilitate a better analysis of the time variability of the source.

GJ 1151 is a star with a very long rotation period of 132 days (Irwin et al., 2011) and low activity in the chromospheric Hα line (Newton et al., 2017). Therefore its corona can be expected to emit mainly at soft X-ray energies below 2.0 keV. We therefore extracted X-ray images from the three CCD detectors in the 0.2-2.0 keV energy band, which we show in Fig. 5.1.

---

[1] `https://xmm-tools.cosmos.esa.int/external/xmm_user_support/documentation/sas_usg/USG/`

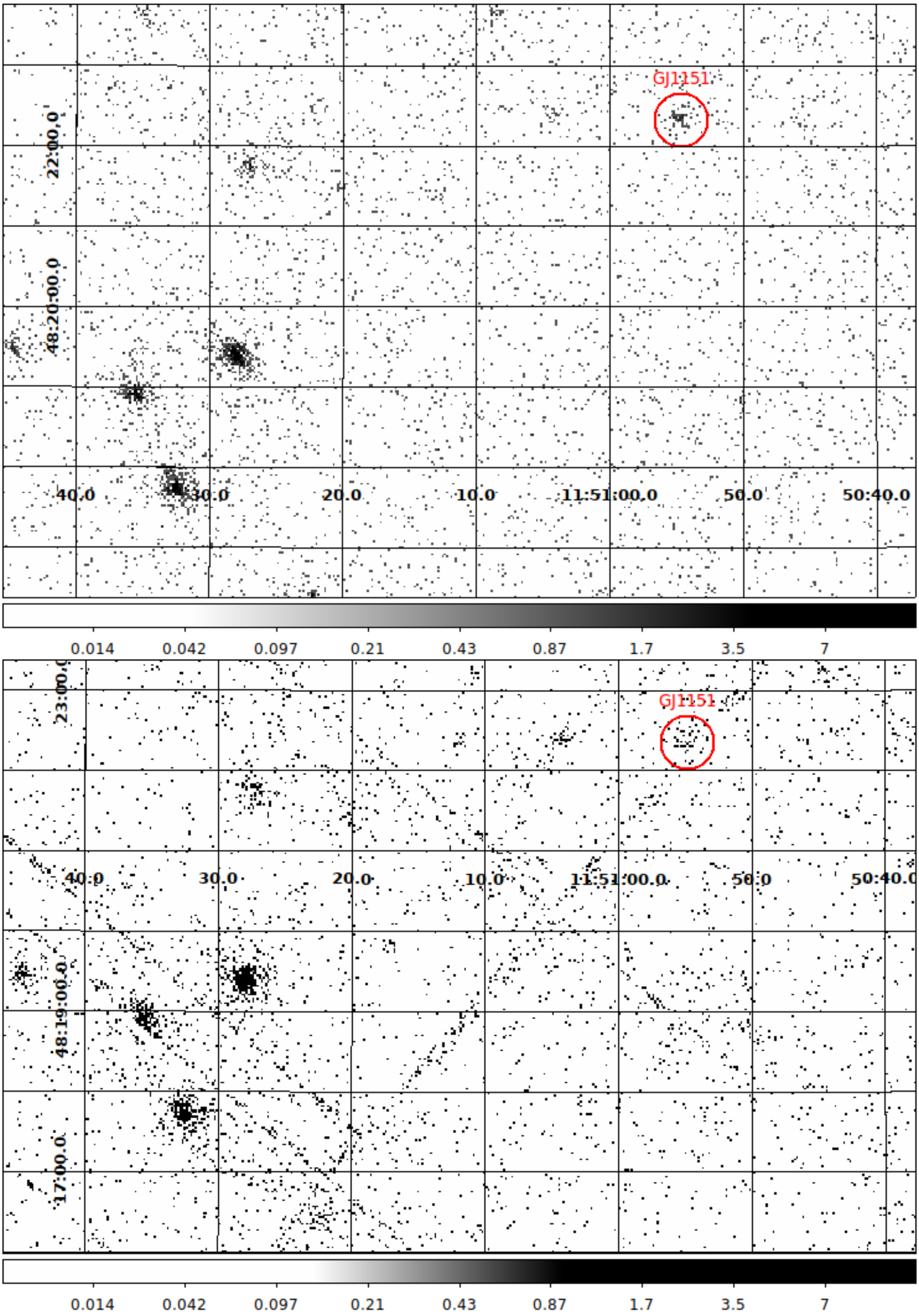
GJ1151
22:00.0
48:20:00.0
40.0
30.0
20.0
10.0
11:51:00.0
50.0
50:40.0
0.014
0.042
0.097
0.21
0.43
0.87
1.7
3.5
7
GJ1151
23:00.0
48:19:00.0
17:00.0
40.0
30.0
20.0
10.0
11:51:00.0
50.0
50:40.0
0.014
0.042
0.097
0.21
0.43
0.87
1.7
3.5
7

Figure 5.1: X-ray image of GJ1151 observed in the 0.2-2 keV energy band with *XMM-Newton* on 1st November 2018. The top panel shows the combined image from the two MOS cameras, the bottom panel shows the image extracted from the PN detector where the target position was located on a chip edge. GJ1151 is marked by a circle with a 20″ radius.

After taking into account the fast proper motion of the star, we placed a circular extraction region with 20″ radius at GJ 1151's expected position during the epoch of the XMM-Newton observation, and defined a nearby source-free background region with a radius of 60″. Unfortunately, GJ 1151's position fell on one of the PN detector's chip edges, so that only the data from the less sensitive MOS cameras could be used for further analysis. For the MOS detectors, we extracted light curves and CCD spectra following the standard procedures of the XMM SAS users guide.

5.4 Results

5.4.1 An X-ray detection of GJ 1151 with XMM-Newton

In Fig. 5.1 we show X-ray images from XMM-Newton's MOS and PN cameras with the position of GJ1151 indicated. An excess is visible at the star's position in all cameras, but weaker in PN due to the closeness of GJ 1151's position to a detector chip edge.

To test whether GJ 1151 is significantly detected in X-rays, we used the Kraft-Burrows-Nousek (KBN) estimator (Kraft et al., 1991) as implemented in the python astropy package (Astropy Collaboration et al., 2013, 2018). The KBN estimator takes as input the number of detected photons in a source detection region and the expected number of background photons in the same region, estimated from a larger source-free area; it assumes both numbers follow Poisson statistics, as is appropriate for X-ray photon counting. The KBN estimator marginalises over the possible background photons in the source detect region, and yields a confidence interval for the source counts in the source detection region.

In the 0.2-2 keV energy band, we find 43 and again 43 counts in the source extraction region for MOS1 and MOS2, respectively. For the same time intervals and energy band we find 112 and 82 counts in the nine times larger background extraction region (i.e. an expected background count rate of 12.4 and 9.1 per exposure in the source extraction region for MOS1 and MOS2, respectively). For both detectors individually the KBN estimator yields a detection at $> 3\sigma$ level.

When combining the signal from both MOS detectors for smaller uncertainties, we therefore have 86 photons in the source region and 194 counts in the larger background region, collected over a total exposure time of $10.46 + 10.46 = 20.91$ks. We then derive a total number of background-subtracted source counts of $64.4^{+9.6}_{-8.9}$ with 1σ uncertainties for both MOS detectors co-added, again using the Kraft-Burrows-Nousek estimator. This translates to a background-subtracted count rate of 3.1 counts per ks for the combined MOS detectors for GJ 1151 in the 0.2-2 keV energy band.

We also checked if there is significant flux at energies above 2.0 keV, and found that there is no significant excess of counts in the energy bands of 2-5 keV or 2-10 keV. This is consistent with GJ 1151 being a soft X-ray emitter, as expected for a low-activity star.

5.4.2 Temporal variability of GJ 1151's corona

We extracted light curves with a time bin size of 1000 seconds from the source and background extraction regions of the two MOS cameras. We co-added the

Table 5.2: Best-fit parameters of the two-temperature coronal model to the MOS data.

Parameter	Value
kT_1 (keV)	$0.095^{+0.03}_{-0.02}$
norm_1 ($\times10^{-5}$)	$5.2^{+7.1}_{-2.6}$
kT_2 (keV)	$0.74^{+0.17}_{-0.25}$
norm_2 ($\times10^{-5}$)	$0.41^{+0.11}_{-0.09}$
flux (erg cm^{-2} s^{-1}), 0.2-2 keV	$7.1^{+0.7}_{-4.6} \times 10^{-14}$
flux (erg cm^{-2} s^{-1}), 0.1-2.4 keV	$1.4^{+0.7}_{-0.9} \times 10^{-13}$
L_X (erg s^{-1}), 0.2-2 keV	$5.5^{+0.5}_{-3.6} \times 10^{26}$
L_X (erg s^{-1}), 0.1-2.4 keV	$1.1^{+0.4}_{-0.7} \times 10^{27}$

signal from the MOS cameras, and show the signal from the source region and the background regions (scaled to the source region size) in Fig. 5.2. The corona of GJ 1151 displays some variability: in the middle of the observation the stellar X-ray emission is indistinguishable from the background count rate, but at the beginning of the observation we seem to be witnessing the decay of a stellar flare. Unfortunately, the peak of the flare was not observed so that typical relations of flare decay times to the length of the flaring coronal loop (Reale, 2007) can not be applied here. Another possibility for the shape of the light curve at the beginning of the observation is rotational modulation of the corona, with an active region rotating from the front of the star to the back. However, as GJ 1151 has a rotation period of more than 100 days, we consider this to be less likely than a flare decay.

There is also a short spike in the source signal towards the end of the observation, but since the background spikes at the same time and the source signal is compatible with the background within 2σ, it is unclear if this represents another flare or not.

We note for completeness that another mechanism for coronal brightness changes is the occurrence of coronal dimmings, which are observed to take place on our Sun after flares which are accompanied by coronal mass ejections (Hudson et al., 1996; Thompson et al., 1998). However, with the X-ray data present for GJ 1151 it is not possible to distinguish between coronal quasi-quiescence versus coronal dimmings caused by coronal mass ejections.

We tried to determine the number of excess counts after the flare has been excluded in order to quantify the quiescent flux of GJ 1151. We therefore compared the counts in the source and background regions for time stamps after the first 4000 seconds of the observation which resulted in a non-detection. The corresponding 3σ upper limit to GJ 1151's count rate during this quiescent time stretch is 2.1 counts per ks for the combined MOS detectors in the 0.2-2 keV energy band.

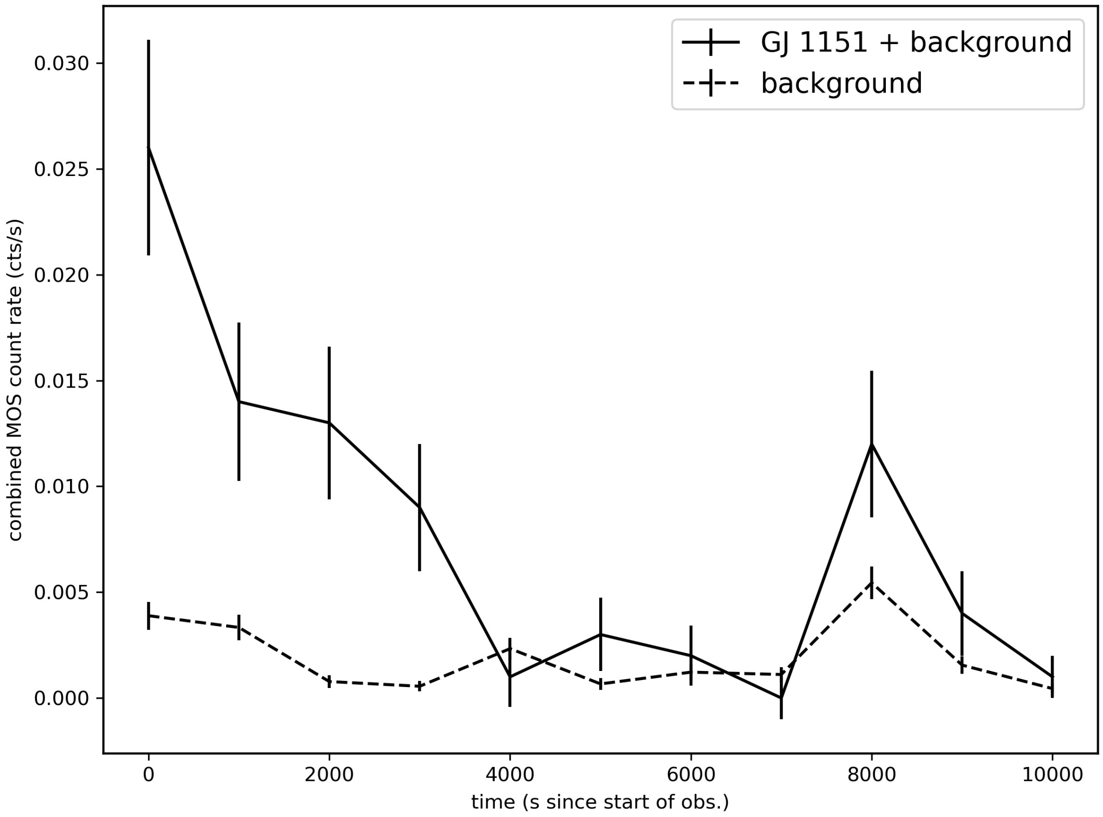

Figure 5.2: The *XMM-Newton* X-ray light curve of GJ 1151 with 1 ks time binning, using the co-added signal from both MOS detectors. The solid-line curve is the signal from the source region containing the true source signal and the underlying background, the background itself as estimated from a nearby region is shown as a dashed line. The star shows variability, possibly the decay of a flare at the beginning of the light curve.

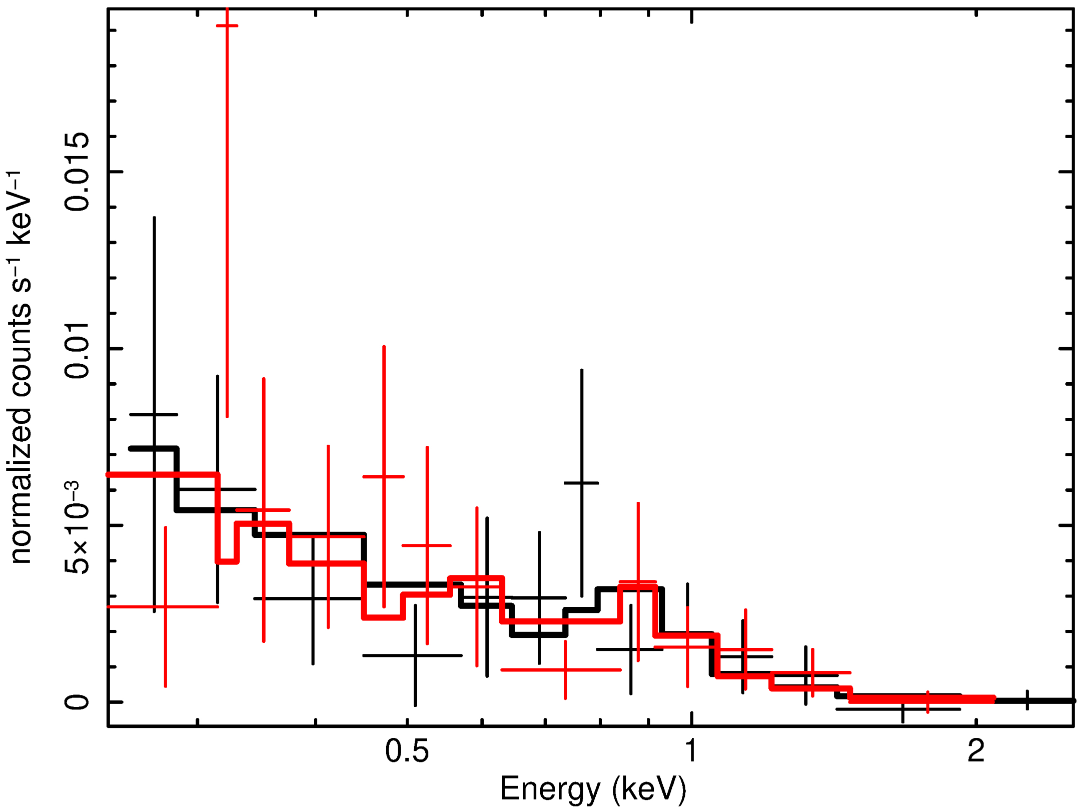

Figure 5.3: The extracted GJ 1151 spectra from *XMM-Newton*'s MOS1 and MOS2 detectors (black and red crosses) are shown together with a two-temperature coronal plasma model fit (thick solid lines). The spectrum is very soft with an average coronal temperature of ca. 1.6 MK.

5.4.3 GJ 1151's coronal properties from X-ray spectra

We extracted CCD spectra of GJ 1151 from the data of the two MOS cameras. We used Xspec version 12 to fit the spectra with an *APEC* coronal plasma model (Smith et al., 2001; Foster et al., 2012), using solar-like coronal abundances from Grevesse & Sauval (1998). Since the number of excess counts is small, we decided to group the counts into bins of at least three photons and appropriately use the Cash statistic (Cash, 1979) for spectral fitting. A single-temperature model did not yield a satisfactory fit, with a Cash statistic value of 35.9 with 28 degrees of freedom; the single-temperature model yielded a coronal temperature of 2.9 MK, but systematically underpredicted the spectral counts at energies below 0.5 keV. Therefore we used a two-component temperature model, which yielded a Cash statistic of value of 24.4 for 26 degrees of freedom. We note here that the Cash statistic, unlike the χ^2 statistic, does not yield a direct null hypothesis probability. However, the difference of the Cash statistic value between one model fit and another is distributed approximately as the difference in χ^2 values for the two models, if count numbers were high enough for the χ^2 statistic to be applicable. Therefore we judged that the two-temperature model, where the value of the Cash statistic is close to the number of degrees of freedom (i.e. similar to a reduced χ^2 value of unity), is a satisfactory fit. We note that since GJ 1151 is located at a distance of only 8 pc to the Sun, spectral effects of X-ray absorption by the interstellar medium can be ignored.

We display the MOS spectra, together with the best-fit model, in Fig. 5.3. The parameters of the best-fit model are listed in Table 5.2. The emission measure (characterized by the APEC model's "norm" parameter) of the lower-temperature component is not very well constrained, because it is close to the lower end of the detectors' energy sensitivity and a lower fitted temperature could be offset by a larger emission measure. Still, from the spectral shape it is clear that GJ 1151 is a very soft X-ray emitter. We note here that in principle one would expect to see variation in the spectrum during the flare decay; however, the signal-to-noise of the spectrum is too low to allow such an analysis, which is why we only calculate a spectral fit for the fully time-integrated observation.

We calculate the average coronal temperature of GJ 1151 to be 1.6MK. The X-ray flux and luminosity is highly dependent on the energy band that is desired for this quantity, because the temperature of its corona is so low that a significant fraction of the fitted flux is located at extremely soft energies below 0.2 keV, which are not observable by XMM-Newton. We determine GJ 1151's X-ray flux and luminosity in the 0.2-2 energy band to be $F_X = 7.1 \times 10^{-14}\,\mathrm{erg\,s^{-1}\,cm^{-2}}$(68% confidence interval), and $L_X = 5.5 \times 10^{26}\,\mathrm{erg/s}$. If we extrapolate the flux to an energy band of 0.1-2.4 keV, as was used by ROSAT, we find $F_X = 1.4 \times 10^{-13}\,\mathrm{erg\,s^{-1}\,cm^{-2}}$, and $L_X = 1.1 \times 10^{27}\,\mathrm{erg/s}$. We note that the uncertainties on the X-ray flux and luminosity are rather large, as reported in Table 5.2, due to the aforementioned uncertainty in the temperature of cooler component.

If we use the same spectral shape to quantify the upper limit of the flux during the quiescent time period, we find the upper limit to be $F_{X,qui} \leq 4.8\,[9.5] \times 10^{-14}\,\mathrm{erg\,s^{-1}\,cm^{-2}}$and $L_{X,qui} \leq 3.7\,[7.5] \times 10^{26}\,\mathrm{erg/s}$ for the 0.2-2 keV [0.1-2.4 keV] energy band. It is likely that the corona of GJ 1151 is even cooler during the quiescent time, which would make the flux even lower than our upper limit.

This places GJ 1151 among low-mass stars of low magnetic activity. We estimate

GJ 1151's bolometric luminosity to be 1.37×10^{31} erg/s; we base this on GJ 1151's mass of $0.167\,M_\odot$ as reported by Newton et al. (2017) and interpolate the bolometric luminosity from the tabulated values of Pecaut & Mamajek (2013)[2]. Therefore GJ 1151's coronal activity indicator is $\log L_X/L_{bol} = -4.4$ in the 0.2-2 keV energy band and -4.1 in the 0.1-2.4 legacy ROSAT energy band. This places GJ 1151 towards the lower end of the activity levels displayed by the very slowly rotating low-mass stars studied by Wright et al. (2018).

5.4.4 Consistency with previous upper limits

Two upper limits on GJ 1151's X-ray luminosity exist, one from the ROSAT All-Sky Survey (RASS) and one from a Chandra ACIS-S observation (ObsID 18944, Chandra observation cycle 18, 2.9 ks exposure time, PI Wright).

Revisiting the Chandra observation, we find that there is actually a marginal excess of counts at the location of GJ 1151 in the 0.2-2 keV energy band, namely 3 X-ray photons in a circular region with $2''$ radius placed at the nominal position of the star, versus a background signal of 0.041 expected counts for the same region size. This corresponds to a detection at 99.7% confidence level, albeit with a highly uncertain excess count measurement of $3.0^{+2.1}_{-1.4}$ counts with 1σ uncertainties, or correspondingly $1.0^{+0.7}_{-0.5}$ counts per ks [3]. Since Chandra's ACIS-S detector has become less sensitive to very soft-energy photons due to a deposit accumulation on its filters, it actually traces mostly photons with energies above 0.7 keV in this observation.

If we use our best-fit model from XMM-Newton and use the ACIS-S effective area at the time of the Chandra observation, we would expect a count rate of 4.5 counts per ks. This is higher than what is seen in the Chandra observation, which means that the star is likely not flaring during the Chandra observation. If we choose to use the same underlying spectrum as seen in XMM-Newton, the detected Chandra count number corresponds to a flux of $1.8 \times 10^{-14}\,\mathrm{erg\,s^{-1}\,cm^{-2}}$, which is likely an underestimate since GJ 1151's coronal X-ray emission would be even softer when the star is not flaring. This is in overall agreement with Wright et al. (2018), who derive an upper limit from this Chandra observation for both the Chandra (0.5-8 keV) and ROSAT (0.1-2.4 keV) energy bands of 1.4×10^{-14} and 2.0×10^{-14}, respectively. The small discrepancy to our detected flux seems to stem from their assumption of a coronal temperature around 0.5 keV, which is indeed often observed for fully convective M dwarfs, but is significantly lower in GJ 1151's corona as the XMM-Newton detection shows.

The RASS observation only has an accumulated exposure time of about 370 s at the position of GJ 1151, corresponding to a non-restrictive upper limit of $1.5 \times 10^{-13}\,\mathrm{erg\,s^{-1}\,cm^{-2}}$in the native ROSAT energy band of 0.1-2.4 keV, using our measured average coronal temperature of 1.6 MK.

---

[2] updated table values available at `https://www.pas.rochester.edu/~emamajek/EEM_dwarf_UBVIJHK_colors_Teff.txt`

[3] We note here that the low count numbers produce strong deviations from a Gaussian uncertainty regime. The $N\sigma$ confidence range is therefore no longer given by symmetrically multiplying the 1σ range limits by a factor of N.

5.5 Discussion

The coronal X-ray brightness of GJ 1151 is not unusual for low-activity M dwarfs. Similar X-ray activity levels have been found for slowly rotating M dwarfs by Wright et al. (2018). However, in the case of GJ 1151 we were able to show that its corona is of a very low temperature, which means that a considerable fraction of its X-ray flux is to be found at very soft energies below 0.3 keV.

Other slowly-rotating M dwarfs have been found to flare occasionally, see for example Raetz et al. (2020), so the fact that GJ 1151 as a low-activity star happens to flare in the XMM-Newton observation is not extraordinary.

In the context of star-planet interactions, the coronal properties we derived for GJ 1151 from our X-ray detection do not contradict the model presented by Vedantham et al. (2020), who based their analysis on the X-ray upper limits available at that time. Specifically, Vedantham et al. (2020) excluded radio flares as an explanation of the radio observations based on an assumed coronal temperature of 2 MK. This is very close to our measured average coronal temperature of 1.6 MK, and following the outlined calculations in Vedantham et al. (2020) a lower coronal temperature would lead to an even lower radio brightness temperature, strengthening their exclusion of radio flares as an explanation. Unfortunately, since the peak of the flare was no included in the X-ray observation, it is not possible no draw further inferences on the flare properties, such as loop length or any type of density analysis of the flaring loop.

The star-planet interaction scenario with open stellar field lines used by Vedantham et al. (2020) assumes a coronal temperature of 1 MK as the base for the stellar wind, and this can be considered realistic given our analysis. Since the X-ray observation contains a flare and the measured coronal temperature, averaged over the full observation, is 1.6 MK, one can assume that the corona of GJ 1151 is even cooler during quiescent times. The relationship of lower X-ray luminosities with lower coronal temperatures is very well established (Telleschi et al., 2005; Schmitt, 1997; Güdel et al., 1997; Johnstone & Güdel, 2015).

We note that the Poynting flux derived by Vedantham et al. (2020) of $F_P \sim 10^{23}$ erg/s is so low that a direct detection of coronal emission induced by star-planet interaction of GJ 1151 with a nearby planet is not in the feasible range for current X-ray observatories.

5.6 Conclusions

We have detected coronal X-ray emission from the M dwarf star GJ 1151, using *XMM-Newton*. The star displays coronal variability, a low coronal temperature of 1.6 MK and an average X-ray luminosity of 5.5×10^{26} ergs s^{-1} in the 0.2-2 keV energy band. The detected X-ray emission is compatible with a reported scenario of sub-Alfvénic star-planet interaction, motivated by the star's observed emission at radio wavelengths.

6 Exoplanet X-ray irradiation and evaporation rates with eROSITA

6.1 Abstract

High-energy irradiation is a driver for atmospheric evaporation and mass loss in exoplanets. This work is based on data from eROSITA, the soft X-ray instrument on board the Spectrum Roentgen Gamma (SRG) mission, as well as on archival data from other missions. We aim to characterise the high-energy environment of known exoplanets and estimate their mass-loss rates. We use X-ray source catalogues from eROSITA, *XMM-Newton*, *Chandra,* and ROSAT to derive X-ray luminosities of exoplanet host stars in the 0.2-2 keV energy band with an underlying coronal, that is, optically thin thermal spectrum. We present a catalogue of stellar X-ray and EUV luminosities, exoplanetary X-ray and EUV irradiation fluxes, and estimated mass-loss rates for a total of 287 exoplanets, 96 of which are characterised for the first time based on new eROSITA detections. We identify 14 first-time X-ray detections of transiting exoplanets that are subject to irradiation levels known to cause observable evaporation signatures in other exoplanets. This makes them suitable targets for follow-up observations.

6.2 Introduction

Exoplanets have been detected in a wide variety of orbital architectures, and a significant fraction of them orbit their host stars at close orbital distances. The first exoplanet detected around a main-sequence star, 51 Peg b, is an example of a so-called hot Jupiter, orbiting its host star in only 4.2 days (Mayor & Queloz, 1995). Exoplanets in close orbits are subject to much higher levels of irradiation from the host star than any planets in our own Solar System. The intense irradiation across the electromagnetic spectrum can cause inflated radii of hot Jupiters (see Fortney & Nettelmann (2010); Baraffe et al. (2010) for reviews). In the UV and X-ray part of the spectrum, the stellar photons are absorbed at high altitudes in the exoplanetary atmosphere, where they can power a hydrodynamic evaporation process (Watson et al., 1981; Murray-Clay et al., 2009). Extended exoplanetary atmospheres as well as ongoing atmospheric escape have been detected through different observational setups that target certain parts of the spectrum in which even optically thin atmospheric layers can cause enough absorption of starlight to produce observational effects during exoplanetary transits. Examples are the Lyman-α line of hydrogen (Vidal-Madjar et al., 2003; Lecavelier Des Etangs et al., 2010; Kulow et al., 2014; Ehrenreich et al., 2015), the near-infrared metastable lines of helium (Spake et al., 2018; Nortmann et al., 2018), and observations in the near-ultraviolet (Salz et al., 2019) and in soft X-rays (Poppenhaeger et al., 2013).

The main driver for exoplanetary atmospheric escape is thought to be the extreme-ultraviolet (EUV) and soft X-ray flux that the planet receives from the host star (Yelle, 2004; Murray-Clay et al., 2009). The EUV component of the stellar spectrum is currently not directly observable because no space observatories with sensitivity at the corresponding wavelengths are in operation; the EUVE satellite was the last major EUV observatory and ceased operations in 2001. In contrast, the X-ray part of the stellar spectrum is observable with a variety of currently operating instruments. The stellar EUV flux in turn can be estimated from the stellar X-ray emission and the UV part of the stellar spectrum (Sanz-Forcada et al., 2011; France et al., 2013). Several uncertainties still exist when the mass-loss rates of exoplanets are estimated, for example the X-ray absorption height in exoplanetary atmospheres and the overall efficiency of exoplanetary mass loss (Owen & Adams, 2014; Cohen et al., 2015; Dong et al., 2017), or mass-loss effects on planet-formation in protoplanetary disks (Monsch et al., 2019). However, one of the most important input quantities of exoplanet evaporation rates, namely the exoplanetary high-energy irradiation, can be determined through X-ray observations.

Launched in 2019, eROSITA is producing the first all-sky survey in X-rays since the ROSAT mission in the 1990s. We present a catalogue of exoplanet X-ray irradiation levels derived from the eROSITA full-sky survey data and the eROSITA Final Equatorial Depth Survey (eFEDS; see the publication by Brunner et al. (2021) in this volume), augmented by archival observations from ROSAT, *XMM-Newton*, and *Chandra*. We calculate the stellar combined X-ray and EUV (in short, XUV) fluxes as well as estimates for the exoplanetary evaporation rates. We report on several exoplanets that are strongly irradiated in the high-energy regime, which makes them good candidates for observing ongoing evaporation signatures at other wavelengths.

The paper is structured as follows: Section 6.3 describes the observations and data reduction; section 6.4 describes the considerations we used for the catalogue matching and the analysis we performed to extract flux estimates for stellar coronae; section 6.5 gives the main results with respect to stellar X-ray fluxes and luminosities, exoplanetary irradiation levels, and mass-loss rates; section 6.6 places the results in the context of exoplanet evaporation; and section 6.7 summarises our findings.

6.3 Observations

6.3.1 eROSITA

The eROSITA instrument consists of seven X-ray telescopes and CCD cameras on board the Russian-German Spectrum-X-Gamma (SRG) spacecraft (Sunyaev et al., 2021) and was launched into orbit in summer 2019. A detailed description of eROSITA is given in Merloni et al. (2012) and Predehl et al. (2021). In short, eROSITA has a circular field of view with a diameter of 1.03°, an average spatial resolution of 26″, and is sensitive to photons from an energy range of 0.2-10 keV. eROSITA observes the whole sky once within six months by scanning along great circles in the sky that are approximately perpendicular to the ecliptic, similar to the ROSAT All-Sky Survey (Voges et al., 1999, 2000; Boller et al., 2016). The survey portion of the eROSITA mission, called the eROSITA All-Sky Survey (eRASS), will last four years, in which the whole sky is scanned eight times. Prior to starting the eRASS, eROSITA performed a calibration and performance verification phase (CalPV), in which it observed an equatorial field of about 140 deg^2 size for an average exposure time of ca. 2 ks per pixel, in order to image a small patch of the sky to the same depth as is expected at the end of the four-year all-sky survey. This eROSITA Final Equatorial Depth Survey (eFEDS) (Brunner et al., 2021) will be included in the Early Data Release of the eROSITA consortium in 2021.

We used data from the intermediate consortium-wide data release of the eRASS1 and eRASS2 surveys, meaning the first and second full-sky surveys performed by eROSITA. We have access to all eRASS X-ray sources located in the half of the sky, which is proprietary to eROSITA_DE, the German eROSITA collaboration (i.e. with a galactic longitude higher than 180°). The raw data were processed with a calibration pipeline based on the eROSITA Science Analysis Software System (eSASS) (see Brunner et al., submitted). The intermediate eRASS1 and eRASS2 catalogues list the positions, detection likelihoods, and vignetting-corrected count rates of the detected X-ray sources in three energy bands, 0.2-0.6 keV, 0.6-2.3 keV, and 2.3-5.0 keV, among other parameters. Typical vignetting-corrected exposure times over an individual half-year survey are about 150 seconds per source, but can differ strongly depending on the position of the source on the sky, with longer exposure times towards the ecliptic poles.

For stellar coronae, significant X-ray emission is typically found at energies below 5 keV, with the exception of extremely powerful (but transient) flares (see Güdel (2004) for a review). We therefore concentrate our study on the three canonically extracted energy bands (0.2-0.6, 0.6-2.3 and 2.3-5.0 keV) of the intermediate eRASS catalogues.

6.3.2 ROSAT

ROSAT was a space telescope that observed the sky in soft X-rays in an energy range of 0.1-2.4 keV (Truemper, 1982), with an all-sky survey (RASS) as well as pointed observations. We used the Second ROSAT all-sky survey (2RXS) source catalogue from Boller et al. (2016), which is available through the VizieR service. To obtain stellar coronal fluxes, we used the counts-to-flux conversion formula from Schmitt et al. (1995), which uses detected count rates and hardness ratios from RASS for a flux calculation. We later scaled these fluxes to a canonical energy band of 0.2-2 keV, with details given in subsection 6.4.2.

6.3.3 XMM-Newton

XMM-Newton is an X-ray mission with several instruments on board (Jansen et al., 2001). Relevant for our analysis here are only the data collected by the EPIC instrument, consisting of three CCD cameras (Turner et al., 2001; Strüder et al., 2001). The energy range and spatial resolution of EPIC is similar to that of eROSITA. The *XMM-Newton* mission provides a number of different source catalogues, including merged source detections from pointed observations, the slew survey, and multiply observed sources (see e.g. Saxton et al. 2008; Watson et al. 2009; Traulsen et al. 2020). We used the 4XMM-DR10 catalogue[1] in its slim version, where the longest existing exposure was selected for any given source.

---

[1] `http://xmmssc.irap.omp.eu/Catalogue/4XMM-DR10/4XMM_DR10.html`

6.3.4 Chandra

Chandra is an X-ray telescope with two X-ray imaging instruments, ACIS and HRC (Weisskopf et al., 2002; Garmire et al., 2003; Murray et al., 1997). HRC is sensitive to photon energies from 0.08-10.0 keV, but provides no intrinsic energy resolution. ACIS has an intrinsic energy resolution of 50 eV (full width at half maximum, FWHM) at soft energies, and has an energy sensitivity of 0.2-10.0 or 0.6-10.0 keV, depending on which chip of the ACIS instrument a source falls onto. We used the *Chandra* Source Catalog (CSC), Release 2.0 (Evans et al., 2010; Evans & Civano, 2018) for our analysis, which is available through the VizieR interface.

6.4 Data analysis

6.4.1 Catalogue cross-matching

We used the NASA Exoplanet Archive catalogue of detected exoplanets as our starting point. We downloaded the full table of confirmed exoplanets and their properties on March 26, 2021 [2], using their default data sets for each exoplanet. We excluded the small number of exoplanets detected by the microlensing method because their stellar distances have large uncertainties of about 50%, which would propagate into our final exoplanetary mass-loss rates as very large uncertainties. We also discarded one entry in the exoplanet table, namely the postulated exoplanet around the cataclysmic variable HU Aqr, because the planet has been shown to be spurious (Schwope & Thinius, 2014; Bours et al., 2014; Goździewski et al., 2015). We plot the remaining exoplanets from the catalogue as the grey points in Fig. 6.1.

The host star coordinates in the Exoplanet Archive table are based on optical observations and are given by NASA for epoch J2015.5 for all sources with a *Gaia* DR2 source ID (Gaia Collaboration et al., 2018b; Lindegren et al., 2018), and for epoch J2000 for the remaining few exoplanet host stars without a *Gaia* DR2 entry. We propagated all host star coordinates to epochs suitable for catalogue matching with the respective X-ray catalogues, using the *Gaia* DR2 proper motions where available, and Hipparcos proper motions otherwise. Typical proper motions of known exoplanet host stars within a distance of 100 pc from the Sun are about 200 μarcsec/yr and significantly smaller at larger distances, but a small number of stars in the sample display proper motions upwards of 1 arcsec/yr.

We then performed a positional source matching of the exoplanet catalogue with the individual X-ray catalogues. The closest X-ray source in a chosen matching radius to an exoplanet host star was selected as the fiducial match. Maximum matching radii were based on considerations of both the typical positional uncertainties of the respective telescopes and the expected uncertainties in propagated stellar positions at the observing epoch. The typical positional uncertainties of the X-ray catalogues are about 12.5″ for ROSAT (Voges et al., 1999), 1.6″ for *XMM-Newton*[3], and 0.8″ for *Chandra*[4]. For eROSITA, the current positional uncertainty in the existing data reduction version is about 5″, but this is expected to improve with further detailed analysis and re-reduction of the data. As the ROSAT RASS survey and the eROSITA eRASS surveys span only narrow epoch ranges, we opted for maximum matching radii of twice the typical positional uncertainties of these catalogues after propagating the stellar positions to an epoch of J1990 for RASS and J2020.25/J2020.75 for eRASS1/eRASS2, respectively. For *XMM-Newton* and *Chandra*, however, their observing epochs span a range of roughly 20 years each, in which significant motions of some of our sample stars can accrue. We therefore initially matched the stars to the *XMM-Newton* and *Chandra* catalogues with large matching radii of $30''$, determined the observational X-ray epoch from the preliminary matches, and then performed a second source matching with suitably propagated stellar positions and narrower maximum matching radii of $5''$ for *XMM-Newton* and $2''$ for *Chandra*[5].

---

[2] `https://exoplanetarchive.ipac.caltech.edu`

[3] `https://www.cosmos.esa.int/web/xmm-newton/news-20201210`

[4] `https://cxc.harvard.edu/cal/ASPECT/celmon/`

The exoplanet host star catalogue is a sparse catalogue containing about 3200 stars over the whole sky, compared to about 700,000 X-ray sources in the eRASS1 catalogue covering the German half of the sky. The other X-ray catalogues we used are denser than the exoplanet host star catalogue as well. It is therefore expected that we do not find any true double matches in our proximity-based matching. The only double match, in which more than one entry in the host star catalogue was matched to the same X-ray source in eRASS and ROSAT, was for the system HD 41004AB. In this system two stars with an on-sky separation of about $0.5''$ are both orbited by known exoplanets, with the lower-mass star being positioned about $0.5''$ to the south of the primary (Raghavan et al., 2010). The system was also observed with *Chandra*, where visual inspection shows an X-ray bright source at the position of the B component, and no additional X-ray source is visible at the position of the A component. We therefore attributed all X-ray flux stemming from the HD 41004AB system to component B.

While there are no further double matches among the catalogues matched here, it is known that several exoplanet host stars are common proper motion binaries with other cool stars (Raghavan et al., 2010; Mugrauer, 2019) that are X-ray sources as well (Poppenhaeger & Wolk, 2014). These companion stars are often not known to host an exoplanet themselves and are therefore not listed in the exoplanet host star catalogue. Some of the companion stars are close enough to the planet host stars to not be spatially resolved by some of the used X-ray telescopes. In these cases, we split the X-ray flux stemming from the system equally between the unresolved stellar components. A more detailed analysis of these systems will be presented in Ilic et al. (in prep.); the list of stars for which such a split was performed in this work is given in the appendix.

To test whether our fiducial X-ray matches can be accepted as bona fide counterparts to the exoplanet host stars, we analysed the ratio of X-ray to bolometric flux for the fiducial matches. Stellar coronae are known to exhibit a ratio of $\log F_X/F_{bol}$ between -2.5 and -7.5 for most stars. Astrophysical exceptions are flaring low-mass stars that can temporarily display values of up to -2 and stars with extremely low or no magnetic activity, such as Maunder minimum stars in the former case or stars with masses that are high enough to prohibit an outer convective envelope in the latter. We extracted bolometric fluxes for exoplanet host stars with *Gaia* DR2 source IDs directly from the *Gaia* DR2 archive where bolometric luminosities

---

[5] In cases where the observed co-added epochs in the catalogues spanned more than three years and proper motions were large or not available, the maximum allowed matching radius was doubled.

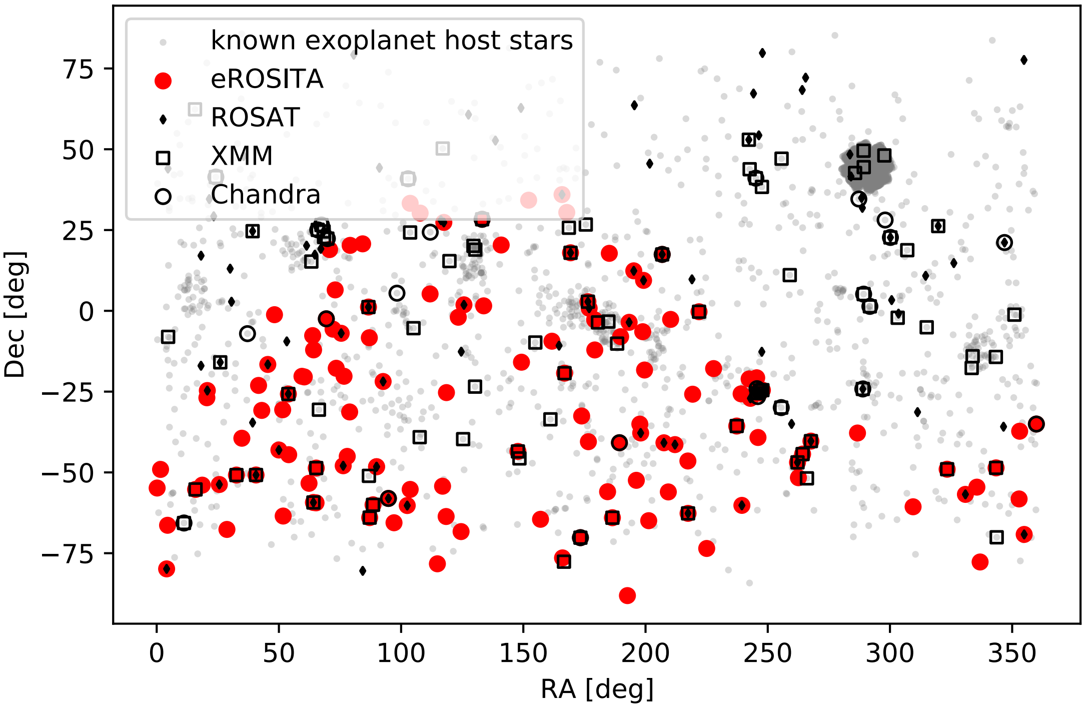

Figure 6.1: X-ray detections of known exoplanet host stars in the sky. Known planet host stars are depicted as small grey dots. The Kepler field at RA = 300 deg as well as the increased density of known planets along the ecliptic due to the coverage by the K2 mission are visible. Detections in the German eROSITA sky with the eRASS1 or eRASS2 survey are shown as filled red circles, previous detections with ROSAT, *XMM-Newton*, and *Chandra* are shown as filled black diamonds, open circles, and open squares, respectively.

were derived with the FLAMES algorithm (Andrae et al., 2018), which yielded L_{bol} values for 184 out of 241 X-ray detected host stars. After unifying X-ray fluxes from different catalogues for a stellar coronal spectral model and a common energy band as described in section 6.4.2, we found that the distribution of the X-ray to bolometric flux ratio of our matched sources is well within expectations for stellar coronal sources (Fig. 6.2).

Furthermore, we compared the soft X-ray fluxes to the infrared fluxes of the matched targets. Salvato et al. (2018) found that stars typically display higher infrared brightness in the WISE W1 band for a given soft X-ray flux than non-stellar X-ray sources such as active galactic nuclei (AGN), with stellar and non-stellar objects being well separated in a plane spanned by the X-ray flux and the W1 magnitude. We display our matched X-ray and optical sources, the majority of which have known W1 magnitudes listed in the exoplanet catalogue, in Fig. 6.3. Almost all of our matched sources fall into the stellar area of the diagram; the single source that falls into the non-stellar part of the diagram is an exoplanet-hosting object that is not a main-sequence star, namely the cataclysmic variable UZ For. We therefore consider it unlikely that our catalogue matches are contaminated by extragalactic sources.

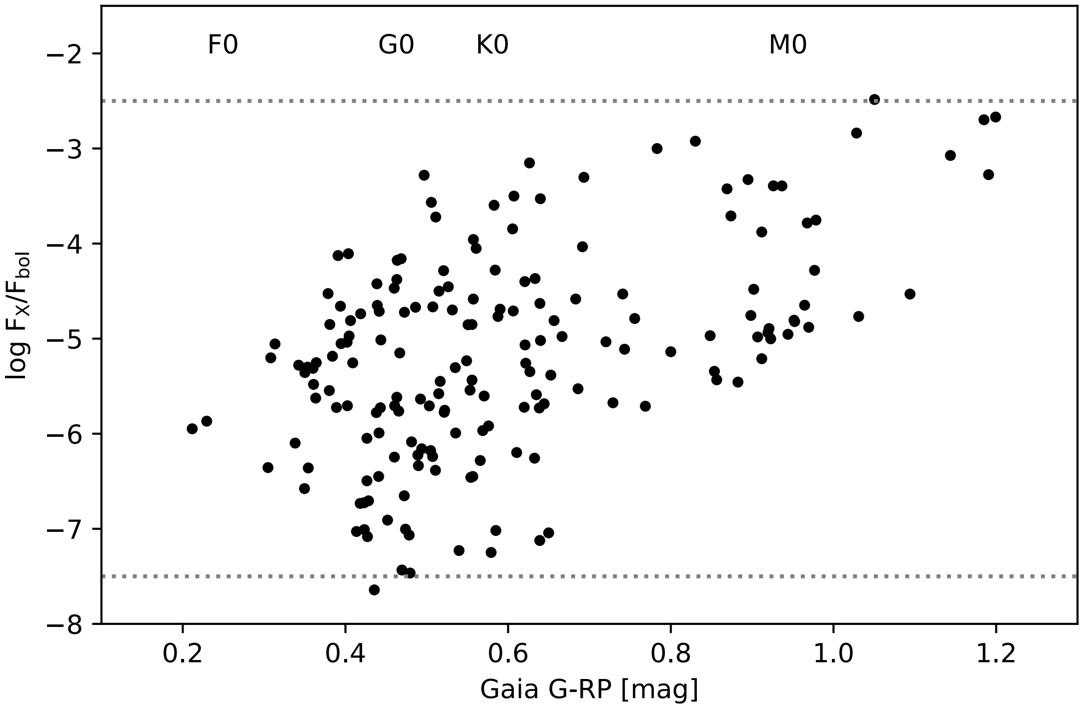

Figure 6.2: X-ray to bolometric flux ratios of the exoplanet host stars in our sample vs their *Gaia* colour $G-R_p$; corresponding spectral types are given at the top of the figure. The horizontal dotted lines indicate the approximate upper and lower boundaries of typically observed flux ratios for main-sequence stars, with which our sample agrees well.

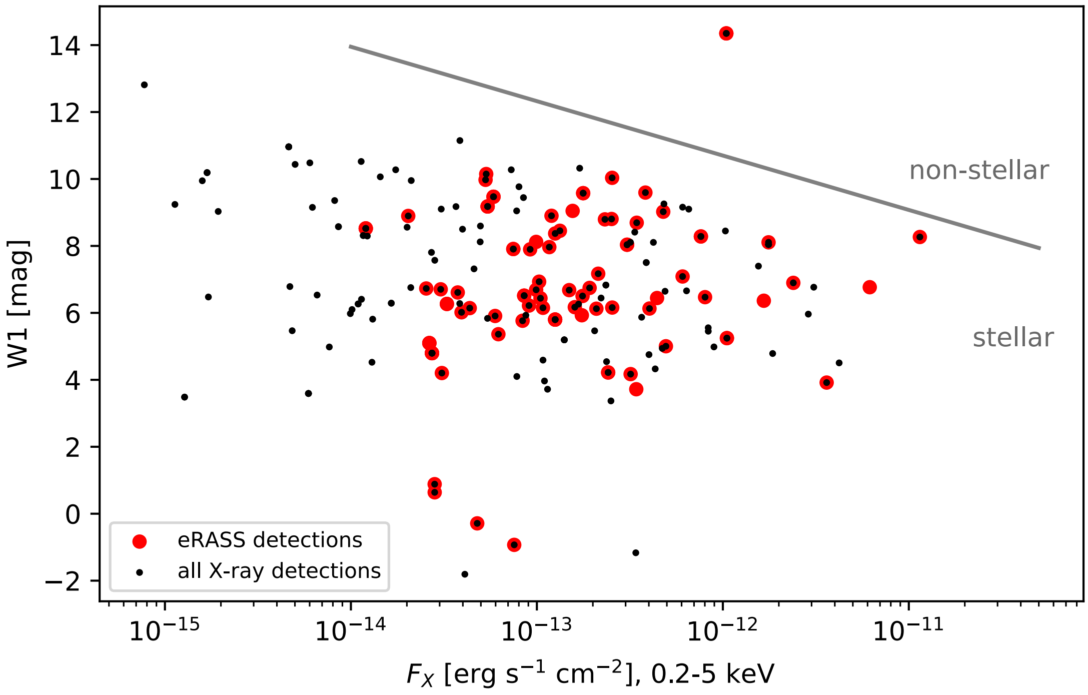

Figure 6.3: Fluxes of the X-ray detected stars in our sample in the soft X-ray band and the WISE W1 infrared band, large red dots for eRASS detections, and small black dots for all X-ray detections. The statistical dividing line between objects of stellar and non-stellar nature (Salvato et al., 2018) is shown as the solid grey line. The only source that falls into the non-stellar part of the parameter space is an exoplanet-hosting cataclysmic variable.

6.4.2 Flux conversions

The X-ray catalogues we used provide fluxes in slightly different energy bands. We opted for a commonly used soft X-ray band of 0.2-2 keV for the analysis of X-ray irradiation levels of exoplanets. We describe in the following how any necessary conversion factors were derived.

Similarly to the *XMM-Newton* catalogue, the intermediate eRASS catalogues use an assumed absorbed power-law spectral model to calculate X-ray fluxes from count rates. The assumed underlying model has an absorption column of $N_H = 1 \times 10^{20}$ and a power-law index of 1.7 for this intermediate version of the eRASS catalogues.

This is not a suitable spectral model for stellar coronae, which are described by an optically thin thermal plasma, with a contribution from absorption by the interstellar medium that tends to be small because detected exoplanets are typically located close to the Sun (more than 80% of the currently detected exoplanet host stars are located within a distance within 100 pc from the Sun).

In order to test whether an assumption of a typical coronal temperature of 0.3 keV is appropriate for the eROSITA-detected planet host stars, we first performed an analysis of X-ray hardness ratios in relation to coronal temperature. We simulated eROSITA spectra with Xspec version 12.11.1 (Arnaud, 1996) using the eROSITA instrumental response files. Because the eRASS surveys are currently still shallow, we omitted an absorbing column and simulated spectra with a single temperature component for a range of coronal temperature parameters with kT between 0.1 and 1.0 keV steps, corresponding to temperatures of approximately 1.1 to 11 million K. We show some of these spectra in Fig. 7.5. For each of these simulated spectra, we calculated the model-based fluxes in the 0.2-0.6 (S), 0.6-2.3 (M) and 2.3-5.0 (H) keV energy bands, as well as their simulated count rates in these bands and the corresponding hardness ratios HR1 = (M-S)/(M+S) and HR2 = (H-M)/(H+M). We find that for the typical range of coronal temperature simulated by us, the hardness ratio HR2 is always very close to -1 because the effective area of eROSITA drops significantly beyond 2.3 keV. The simulated softer hardness ratio HR1 ranges from -0.9 to 0.8. We display the relation of the modelled coronal temperature and the simulated eROSITA hardness ratios in Fig. 6.5. This is valid for stars whose coronal spectra are dominated by a single-temperature component; multiple stars and strongly different coronal temperature components can behave differently with respect to their observed hardness ratios. In the observed data for our sample stars, the hardness ratio HR1 spans the full range between -1 and 1, with typical uncertainties of about ±0.2, that is, consistent with the simulated range of values. The majority of our observed stars is concentrated between values from -0.1 to 0.9 (Fig. 6.6), with a median of 0.34. This corresponds to a coronal temperature of about 0.3 keV. The observed values of HR2 agree with a value of -1 within observational uncertainties.

Given the observed hardness ratios, the eROSITA-detected sample agrees well with a typical coronal temperature of 0.3 keV, which we used to correct the final fluxes for a power-law to a stellar coronal model. We find the conversion factor between the fluxes to be $F_{\mathrm{X,\,coronal}} = 0.85 F_{\mathrm{X,\,powerlaw}}$. The eRASS stellar fluxes were calculated by applying the relative conversion factor to the power-law-derived fluxes from the intermediate eRASS catalogues.

For ROSAT, we again used a typical coronal temperature of $kT = 0.3\,\mathrm{keV}$ to trans-

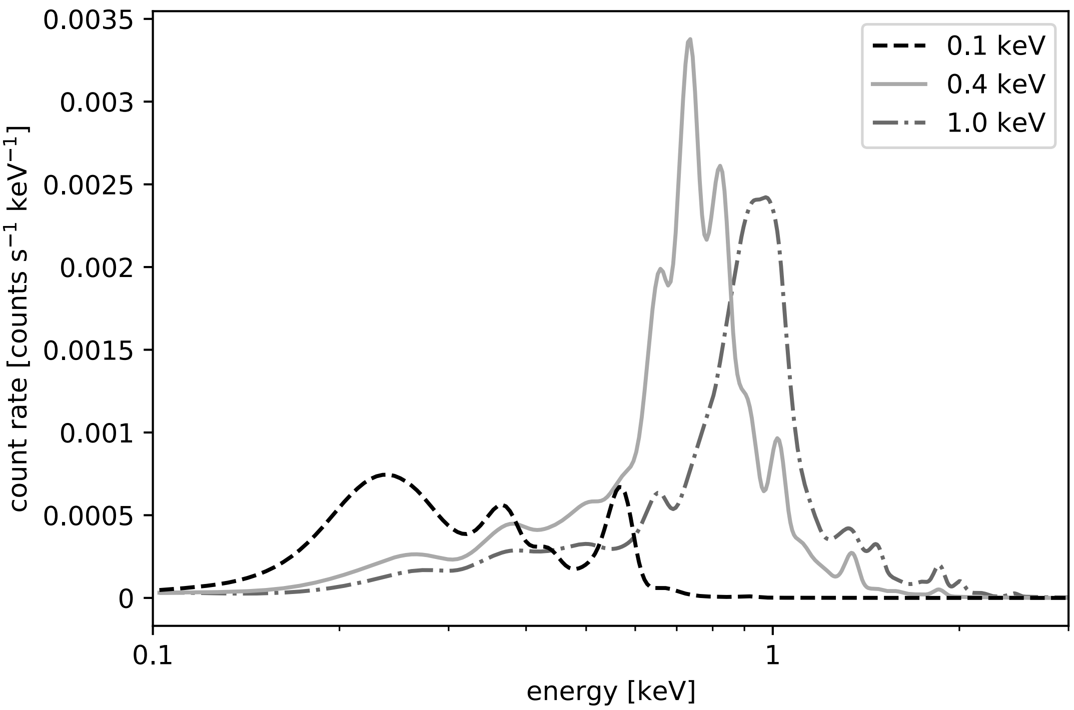

Figure 6.4: Simulated stellar coronal spectra using the eROSITA instrumental response. A single-temperature coronal plasma model was used with temperatures of 0.1, 0.4, and 1 keV (1.1, 4.6, and 11.4 million K). Almost all photons are emitted at energies below 2 keV even for very hot stellar coronae.

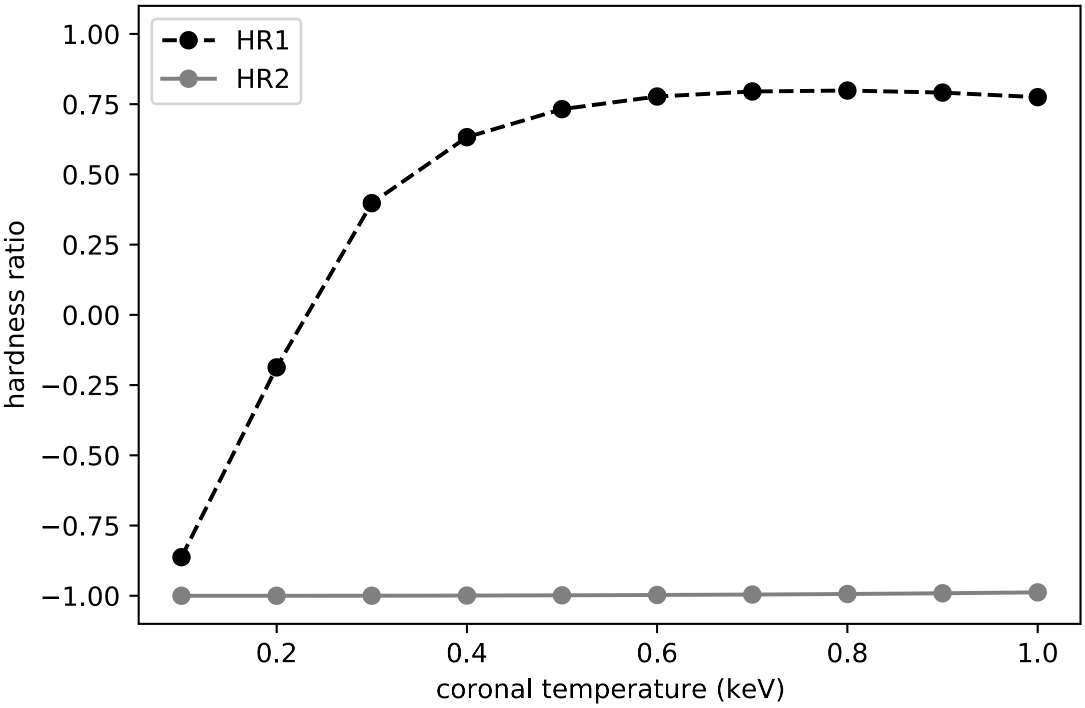

Figure 6.5: Hardness ratios HR1 and HR2 from simulated stellar coronal eROSITA spectra as a function of coronal temperature. HR2 is always close to -1, rising only very slightly for very high temperatures, and HR1 rapidly rises from low to moderate coronal temperatures and then saturates at a value of about 0.75 for temperatures above 0.5 keV.

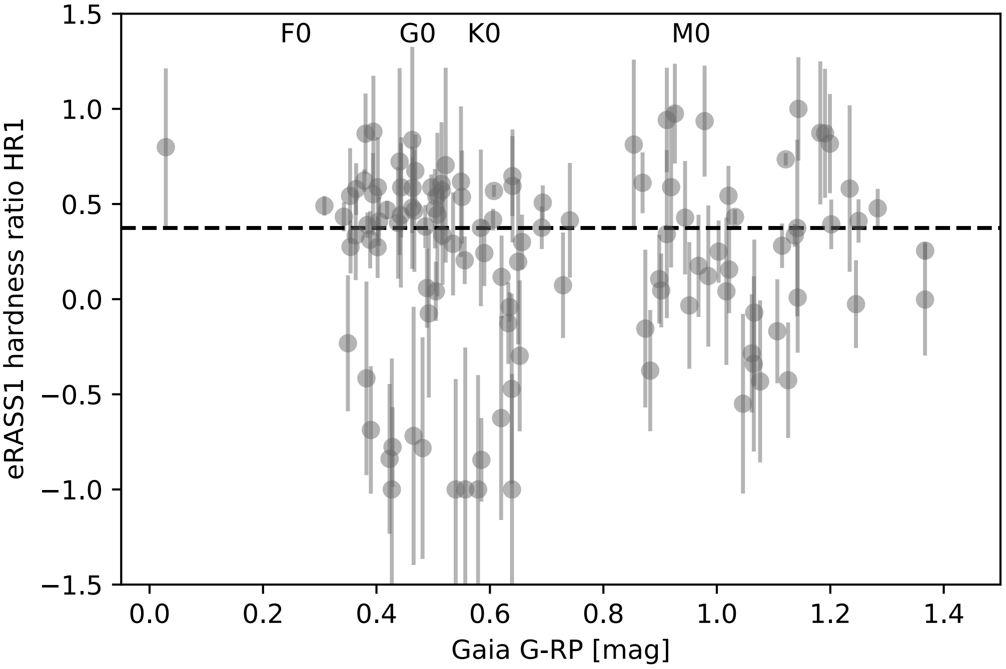

Figure 6.6: Observed hardness ratio HR1 with 1σ uncertainties vs the *Gaia* $G - RP$ colour for the stars in our sample. The median hardness ratio, corresponding to a coronal temperature of about 0.3 keV, is depicted by the dashed line. The quite blue star to the left is the Herbig Be star HD 100546, a known X-ray emitter (Skinner & Güdel, 2020).

form the fluxes from the 0.1-2.4 keV band into the canonical 0.2-2 keV band, using the WebPIMMS tool. The conversion factor is $F_{\mathrm{X},0.2-2\,\mathrm{keV}} = 0.87 \times F_{\mathrm{X},0.1-2.4\,\mathrm{keV}}$.

For *XMM-Newton*, the 0.2-2 keV band already is one of the canonical bands given in the source catalogues, as the sum of bands 1 (0.2-0.5 keV), 2 (0.5-1.0 keV), and 3 (1.0-2.0 keV). However, because the *XMM-Newton* catalogue fluxes assume an underlying power-law spectrum with $N_H = 3 \times 10^{20}$ and a power-law index of 1.7 Rosen et al. (2016), we need to correct these fluxes to an underlying stellar coronal model. We again chose as a representative stellar model a coronal plasma with a temperature of 0.3 keV. *XMM-Newton* typically has deep pointings, detecting sources at larger distances than eROSITA, so that for this model a non-zero absorption column of $N_H = 3 \times 10^{19}$ was used. The relative corrections compared to the power-law fluxes depend on the specific instruments and filters used in a given observations. Using the WebPIMMS tool[6], we find a typical correction factor of $F_{\mathrm{X,\,coronal}} = 0.87 F_{\mathrm{X,\,powerlaw}}$ for the 0.2-2 keV band for the combined signal from the EPIC cameras.

For *Chandra*, its second source catalogue also lists fluxes that are not explicitly model dependent, which are derived from the energies of the detected photons and the effective area of the instrument at these energies. We constructed the soft flux in the 0.2-2.0 keV band by combining the u (0.2-0.5 keV), s (0.5-1.2 keV), and m (1.2-2.0 keV) bands. However, it needs to be noted that depending on the instrument used in a given observation, the flux in the softest band may have gone undetected because the ACIS-I configuration has a very small effective area at the softest energies. Therefore some of the *Chandra*-derived fluxes may underestimate the true soft-band X-ray flux of a star.

6.4.3 Optical loading in eROSITA data

Objects with high optical brightness can cause spurious signals in X-ray observations. While X-ray CCDs are mainly sensitive to genuine X-ray photons, a large number of optical and infrared photons impinging on a CCD pixel within a readout time frame can release electrons in the CCD, which can be falsely attributed to an X-ray photon event; this is called 'optical loading'.

We show the nominal X-ray fluxes from the eRASS1 catalogue versus the optical *Gaia* magnitude of host stars in our sample in Fig. 6.7. We find that stars with an optical brightness of $m_G = 4\,\mathrm{mag}$ or brighter in the *Gaia* band display an apparent floor to their detected eRASS fluxes that rises with optical brightness. The A0V star β Pic is one of these stars, and it is known to be X-ray dimmer by two orders of magnitude from previous pointed X-ray observations (Hempel et al., 2005; Günther et al., 2012). We therefore attribute the apparent X-ray flux of optically bright sources with $m_G \lesssim 4\,\mathrm{mag}$ to optical loading in eROSITA observations and discard their contaminated eROSITA X-ray fluxes from the further analysis. We note that at least one optically bright star, ϵ Eridani, is a genuinely X-ray bright star that is known from observations with other X-ray telescopes (Poppenhaeger et al., 2010; Coffaro et al., 2020). However, a detailed spectral analysis of the eROSITA data to tease apart its coronal X-ray emission and the optical loading is beyond the scope of this work. We therefore use the measured ϵ Eri X-ray flux from *XMM-Newton* in

---

[6] `https://heasarc.gsfc.nasa.gov/cgi-bin/Tools/w3pimms/w3pimms.pl`

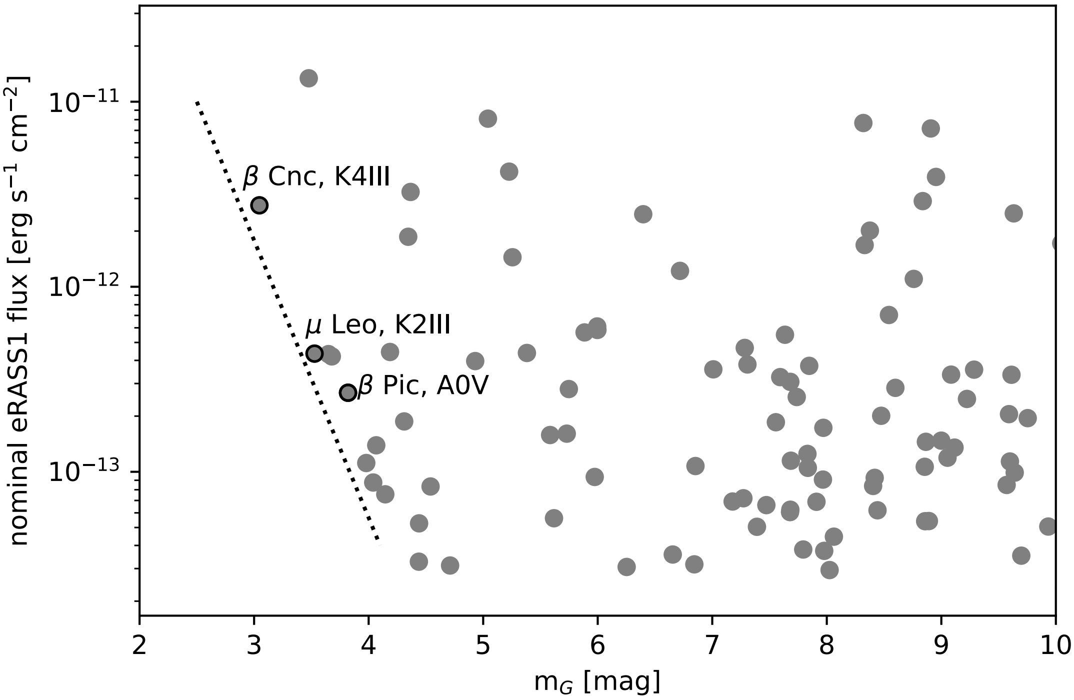

Figure 6.7: Nominal X-ray fluxes from eRASS1 vs optical brightness for stars in our sample. For stars with an apparent *Gaia* magnitude brighter than 4 mag, there is a clear trend towards high apparent eRASS fluxes, which can be attributed to optical loading. Some individual bright stars named in the plot can be expected to be only weak X-ray emitters because they are either lacking an outer convective envelope (β Pic) or are coronal graveyard-type giants (Ayres et al., 2003). Furthermore, these specific stars are known to be X-ray dim from previous observations by other X-ray telescopes.

the further analysis.

6.5 Results

6.5.1 New X-ray detections of exoplanet host stars

We show the positions of X-ray detected exoplanet host stars in the sky in Fig. 6.1. The total number of X-ray detected planet-hosting stars increases from 164 in the pre-eROSITA epoch to 241, that is, 77 are added through eRASS1 and eRASS2. This increase can be expected to roughly double with the data from the Russian half of the eROSITA data. The X-ray detection fraction of exoplanet host stars in the German eROSITA sky is 89% within a distance of 5 pc and 70% within 20 pc. At larger distances, the detection fraction drops rapidly (Fig. 6.8).

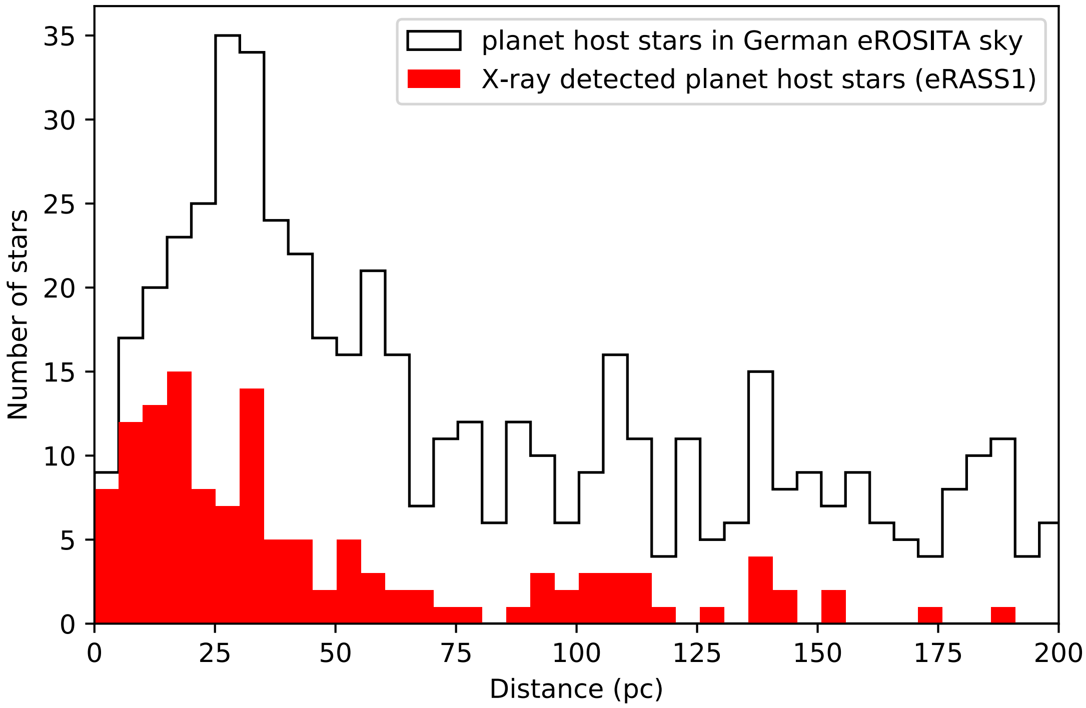

Figure 6.8: Histogram of exoplanet host stars in distance bins of 5 pc (white with black outline) and the exoplanet host stars detected in the eRASS1 survey (red) in the German eROSITA sky out to a distance of 200 pc. The detection fraction is high with about 70% out to 20 pc and then drops off rapidly. A small number of X-ray detections exists for planet host stars at larger distances.

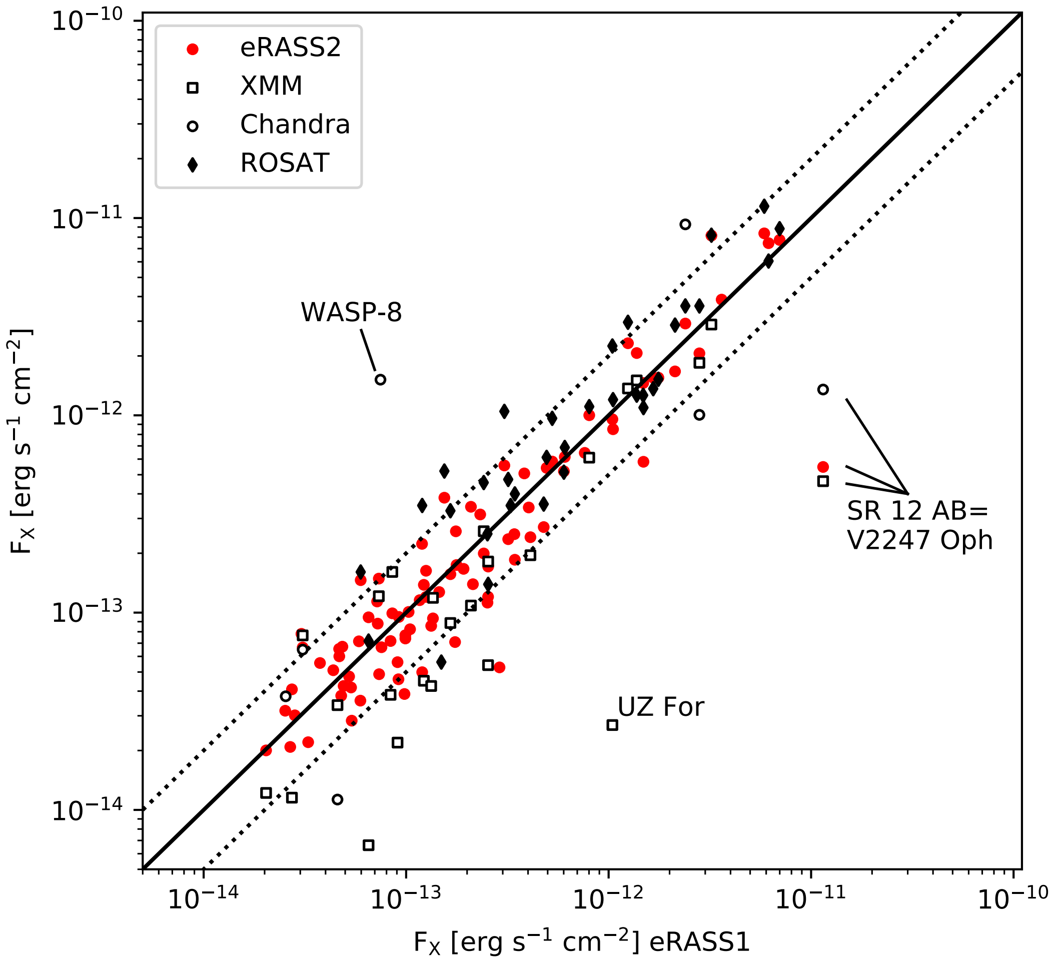

Figure 6.9: Comparison of soft X-ray fluxes in the 0.2-2 keV band for exoplanet host stars detected by more than one X-ray mission to fluxes detected by eRASS1. Stars detected by both eRASS1 and eRASS2 are shown in red. Some individual outliers are marked by name; these objects are expected to display strong variability in X-rays.

6.5.2 Flux comparisons for different X-ray missions

After performing the flux conversions for all data sets to cover the 0.2-2 keV range and correcting for an underlying stellar coronal model as laid out in section 6.4.2, we compared the fluxes observed for stars that were detected in more than one mission. We show the X-ray fluxes for stars that were detected in eRASS1 versus their fluxes observed in eRASS2, ROSAT, *XMM-Newton,* and *Chandra* in Fig. 6.9. About 75% of the observations display X-ray fluxes that agree within a corridor of 0.3 dex, which covers the typical low-level intrinsic variability of stellar coronae. The nominal flux discrepancies grow larger towards the faint end, which is to be expected because the flux uncertainties of the individual measurements increase as well. Additionally, when data sets from different surveys and/or pointed observations are compared, the shallowest survey will detect stars at the bottom of the survey sensitivity only when they happen to be temporarily X-ray bright, for example because of a flare. We see this effect in two directions here: the ROSAT survey is shallower than eRASS, which is why we see the ROSAT-eRASS data-points skewing towards higher ROSAT fluxes in the X-ray faint regime. On the other hand, eRASS tends to be much shallower than pointed *XMM-Newton* observations, which is why we see the XMM-eRASS data-points skewing towards higher eRASS fluxes at the X-ray dim end. For *Chandra*, there are not enough common detections to cause any visible skew.

Some individual notable outliers in the plot stem from intrinsically strongly variable stars, such as the binary T Tauri star V2247 Oph, the cataclysmic variable UZ For, and the M dwarf GJ 176, which is known to flare frequently (Loyd et al., 2018).

6.5.3 X-ray irradiation and mass loss of exoplanets

Exoplanets experiencing an intense high-energy irradiation are expected to lose parts of their atmosphere through a so-called energy-limited escape process, which is much more efficient than Jeans escape (Watson et al., 1981). The incoming XUV flux is assumed to be the driver of this process. The process describes that a certain part of the impinging high-energy flux heats the upper layers of the exoplanetary atmosphere, which expands upwards and can push the layers above out of the gravitational well of the exoplanet. There are known limitations to the energy-limited escape model, for example, it is expected for very high X-ray irradiation levels that hydrogen line cooling will start playing a more significant role, so that less energy is converted into atmospheric expansion (Murray-Clay et al., 2009). Magnetic effects such as stellar winds interacting with the planetary atmosphere or a planetary magnetosphere shielding the planet from winds may also play a role (Owen & Adams, 2014; Cohen et al., 2015; Dong et al., 2017). In the context of this work, we use a simple energy-limited hydrodynamic escape model based on Lopez et al. (2012) and Owen & Jackson (2012), with an atmospheric mass-loss rate given by

$$\dot{M} = \epsilon \frac{\pi R_{XUV}^2 F_{XUV}}{KGM_{pl}/R_{pl}}, \tag{6.1}$$

where ϵ is the efficiency of the atmospheric escape, which we assume to be 0.15, G is the gravitational constant, K is a factor representing the effect of Roche-lobe overflow, which we assume to be negligible for most systems and set to 1, M_{pl} is

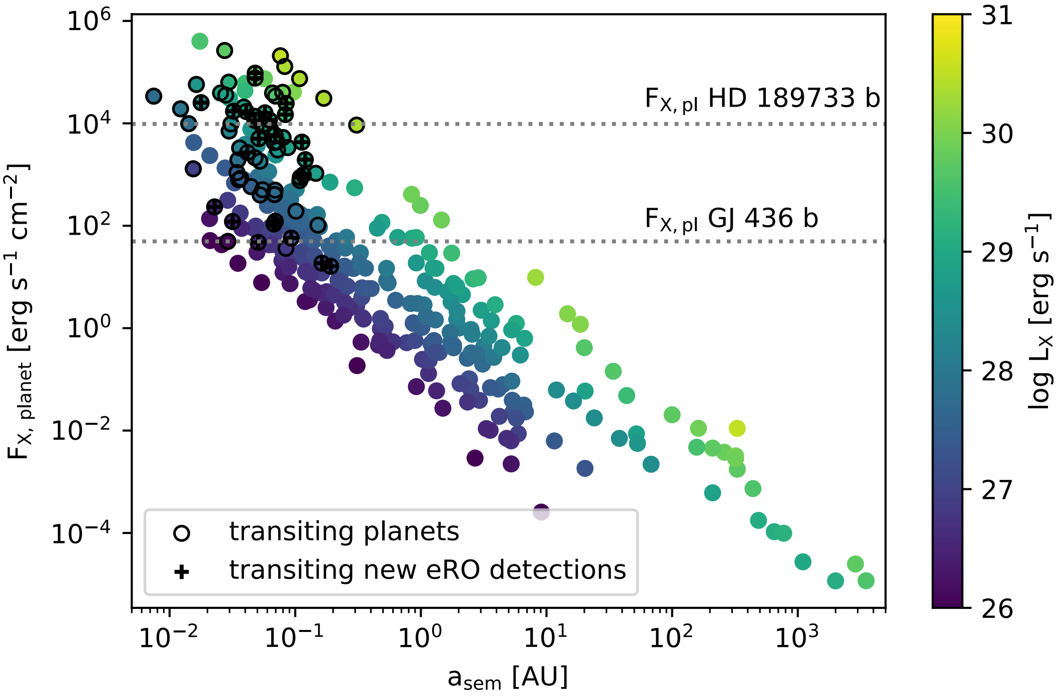

Figure 6.10: X-ray irradiation fluxes of exoplanets vs their orbital semi-major axis. The vertical spread represents the intrinsic luminosity distribution of the host stars. Transiting exoplanets are marked with open black circles; new eROSITA X-ray detections among them are additionally marked with a black cross. For guidance, the X-ray irradiation fluxes of known evaporating exoplanets, the hot Jupiter HD 189733 b and the warm Neptune GJ 436 b, are shown as horizontal dotted lines.

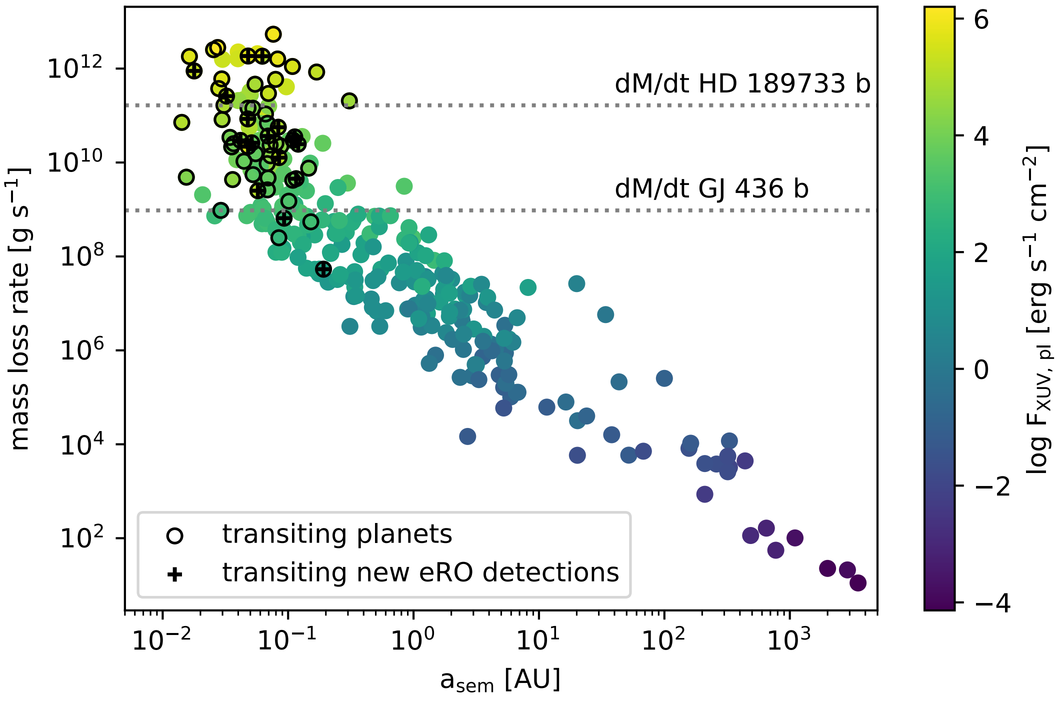

Figure 6.11: Estimated mass-loss rates of exoplanets in the energy-limited escape model (see text for details). The vertical spread represents the intrinsic luminosity distribution of the host stars. Transiting exoplanets, which are in principle accessible to follow-up observations to detect ongoing mass loss, are marked with open black circles; new eROSITA X-ray detections among them are additionally marked with a black cross. For guidance, the estimated mass-loss rates of known evaporating exoplanets, the hot Jupiter HD 189733 b and the warm Neptune GJ 436 b, are shown as horizontal dotted lines.

the mass of the planet, R_{pl} is the optical radius of the planet, F_{XUV} is the XUV flux incident on the planet, and R_{XUV} is the planetary radius at XUV wavelengths, which we assume to be 1.1 times the optical radius. For a detailed discussion of the assumptions made in this model, we refer to Poppenhaeger et al. (2021).

To estimate stellar XUV fluxes from X-ray fluxes alone, a variety of approaches exist (Sanz-Forcada et al., 2011; Linsky et al., 2014; Chadney et al., 2015; Johnstone et al., 2020; King & Wheatley, 2021). We chose the conversion relation between X-ray and EUV fluxes by Sanz-Forcada et al. (2011), which uses spectral energy distributions determined for a sample of cool stars. We first converted our X-ray fluxes for the 0.2-2 keV band into the required input band of 0.1-2.4 keV for the conversion. This was derived using WebPIMMS, which yields a stellar coronal flux ratio of 1.15 between the 0.1-2.4 keV and the 0.2-2 keV flux for a typical coronal temperature of 0.3 keV. We then added the X-ray and EUV to obtain the XUV flux.

The resulting X-ray fluxes in the 0.2-2.0 keV band at the planetary orbits are shown in Fig. 6.10. The XUV fluxes are a factor of about five to ten higher than the X-ray fluxes alone. We immediately see the X-ray luminosity distribution of cool stars depicted in the vertical spread at any given planetary orbital semi-major axis. The planets that are amenable to follow-up observations of currently ongoing mass loss are planets that are transiting and are highly irradiated in the high-energy regime. We indicate the transiting planets by black circles and the new X-ray detections of host stars of transiting planets by additional black crosses. The clustering of transiting planets at close orbital distances comes from the geometric probability of a planet at a given inclination to be transiting, which strongly decreases for larger semi-major axes. Of the about 90 transiting planets with X-ray detected host stars, 26 stem from new eROSITA discoveries. Comparing the irradiation fluxes with the known evaporating exoplanets HD 189733 b and GJ 436 b (see the discussion in section 6.6), we find that a total of 50 exoplanets in our sample show irradiation levels in excess of the one experienced by GJ 436 b, indicating that these exoplanets may be undergoing directly observable evaporation at the moment.

To determine the mass loss, data on both the planetary mass and radius are required. However, depending on the discovery method of a given planet, only the planetary mass or the radius may be known, but not necessarily both. In these cases we used the mass-radius relationship by Chen & Kipping (2017) to estimate a planetary radius from the planet mass, or its mass from its radius. Chen & Kipping (2017) divided planets into a 'terran' regime with radii smaller than $2R_\oplus$, in which masses are dominated by the rocky core, and a 'Neptunian' regime for planets with radii of $2R_\oplus$ or more in which the gaseous envelope contains a significant fraction of the total mass. In our final mass-loss estimates we only included numeric estimates for exoplanets with radii larger than $1.6R_\oplus$, based on Rogers (2015), who showed that exoplanets smaller than $1.6R_\oplus$ are likely fully rocky and therefore unlikely to undergo any significant atmospheric mass loss.

We show the resulting mass-loss estimates in Fig. 6.11. A table of estimated mass-loss rates and the related X-ray quantities is available as an electronic data table (see the appendix). The highest mass-loss rates are as expected found for planets in very close orbits around their host stars. Here the vertical spread comes from both the X-ray luminosity distribution of the host stars and the spread in individual exoplanet masses and radii, which affects the estimated mass-loss rates as well. We find four new eROSITA measurements with expected mass-loss rates higher than for HD 189733 b, and 14 new eROSITA discoveries with expected mass-loss rates higher than for the Neptune GJ 436 b.

6.6 Discussion

6.6.1 Exoplanet mass-loss rates in context

While exoplanet evaporation rates can be estimated under the energy-limited mass-loss regime, there are also direct observations of ongoing evaporation for some planets. One possibility for direct mass-loss observations is through transit observations in the ultraviolet Ly-α line of hydrogen. The observed line shape is quite complex, even in the absence of exoplanetary mass loss. The host star produces emission in Ly-α, which is then partially absorbed by the interstellar medium, and finally, also Earth's geocorona may add to the detected photons at the Ly-α wavelength. An actively evaporating exoplanetary atmosphere can be detected in the wings of the line, where planetary hydrogen moving at moderately high velocities causes additional absorption in the blue or red wing (or both) during the planetary transit. This was first successfully observed for the hot Jupiter HD 209458 b (Vidal-Madjar et al., 2003), and subsequent observations have targeted other hot Jupiters and even Neptunic planets. We focus here on the hot Jupiter HD 189733 b and the mini-Neptune GJ 436 b for our comparisons to the estimated mass-loss rates of other exoplanets.

HD 189733 b is a well-studied transiting hot Jupiter, orbiting a K0 star at a distance of about 20 pc from the Sun. The optical brightness of the host star makes this exoplanet one of the best-studied targets for transmission spectroscopy. Its absorption signature in the hydrogen Ly-α line showed that the planet is undergoing mass loss (Lecavelier Des Etangs et al., 2010). Because Ly-α observations can only quantify atomic (not ionised) hydrogen in the planetary atmosphere that is moving at relatively high speeds, determining mass-loss rates from these observations typically requires some additional model assumptions. Lecavelier Des Etangs et al. (2010) estimated the current mass-loss rate to be in the range of 10^9 and $10^{11}\,\mathrm{gs}^{-1}$. Other estimates for the mass loss have been made, such as the model by Chadney et al. (2017), who calculated an upper limit to the mass-loss rate of HD 189733b of about 10^7 and $10^{12} gs^{-1}$ during stellar flares with large-scale proton events. Our calculation is based on the energy-limited escape model and estimates a current mass-loss rate of about $1.8 \times 10^{11} gs^{-1}$, which is at the upper end, but compatible with the estimates based on hydrogen Ly-α observations.

In contrast, GJ 436 b is a mini-Neptune in a close orbit around a nearby (9.75 pc) M dwarf that is only mildly X-ray active. This exoplanet has been observed to expel a spectacularly large hydrogen tail, as was first presented by Kulow et al. (2014) and then analysed in more detail by Ehrenreich et al. (2015). The atomic hydrogen tail observed in the Ly-α line covers almost half of the stellar disk during transits, with the egress being delayed by several hours compared to the broadband optical transit. This is consistent with an extended tail-like structure consisting of the evaporating atmosphere. While the hydrogen transit signal is strong and well observable, the modelled mass-loss rate is rather modest with about 4×10^6 and $10^9 gs^{-1}$ (Kulow et al., 2014). Simulations conducted by Villarreal D'Angelo et al. (2021) calculated a higher mass-loss rate of up to $10^{10} gs^{-1}$. Our own results based on the high-energy irradiation estimate a current mass-loss rate of about 1.0×10^9 gs^{-1}, being bracketed by the hydrogen observations and simulations. This exoplanet shows that even more moderate mass-loss rates can produce strong observable signatures.

6.6.2 Interesting individual targets identified with eROSITA data

Transiting exoplanets with a high level of XUV irradiation are suitable for follow-up observations of ongoing mass loss, for example through transmission spectroscopy in the ultraviolet hydrogen Ly-α line or the metastable lines of helium (HeI 10830) in the infrared. We briefly discuss some particularly interesting systems here in terms of the planetary high-energy environment and mass loss.

TOI-251: TOI-251 is a solar-mass dwarf star with an apparent *Gaia* brightness of $G = 9.8$ mag, located at a distance of 99.5 pc from the Sun. It is a relatively young star with an age of 40–320 Myr, estimated from its rotation and magnetic activity (Zhou et al., 2021). TOI-251 hosts a mini-Neptune with a radius of $2.7 R_\oplus$ that orbits its host star in 4.9 days. We detect the host star with a high X-ray luminosity in the 0.2-2.0 keV band of $L_X = 1.5 \times 10^{29}\,\mathrm{erg}\,s^{-1}$ in eRASS1 and $L_X = 1.9 \times 10^{29}\,\mathrm{erg}\,s^{-1}$ in eRASS2. The source was previously detected in a pointed observation with ROSAT. The reported X-ray luminosity was slightly lower with $L_X = 1.1 \times 10^{29}\,\mathrm{erg}\,s^{-1}$ (Zhou et al., 2021). We derive that the orbiting mini-Neptune experiences an X-ray irradiation flux of about $16000\,\mathrm{erg\,s^{-1}\,cm^{-2}}$, corresponding to an estimated mass loss of about $3 \times 10^9\,\mathrm{g\,s^{-1}}$. This is higher than the estimated mass-loss rate of the known evaporating mini-Neptune GJ 436 b by a factor of ten, which makes this a highly interesting target for follow-up observations. Furthermore, this planet currently straddles the so-called evaporation gap in the radius distribution of planets (Fulton et al., 2017), indicating that it may currently undergo a marked change in radius due to evaporation. Poppenhaeger et al. (2021) recently showed for another young star-planet system, V1298 Tau and its four planets, that the early rotational evolution of the host star can make a significant difference in the initial-to-final radius relation of exoplanets. It is interesting in this context that TOI-251 seems to have already arrived on the slow/I-type sequence (Barnes, 2010) of the stellar colour-rotation diagram (Zhou et al., 2021). This means that its future magnetic activity evolution and therefore the future planetary mass-loss evolution are relatively well predictable.

GJ 143: GJ 143 is a bright K dwarf located at a distance of 16.3 pc from the Sun, with an apparent *Gaia* brightness of $G = 7.7$ mag. It hosts two planets. Planet b is a Neptunic planet in an orbit of 35.6 days (Trifonov et al., 2019), and planet c is a small rocky planet in a closer orbit of 7.8 days (Dragomir et al., 2019). The host star is only moderately X-ray bright with a luminosity of $L_X = 1.7 \times 10^{27}\,\mathrm{erg\,s^{-1}}$ in the 0.2-2.0 keV band. However, this is enough to create a high-energy environment of roughly similar intensity as the one that is present for the evaporating Neptune GJ 436 b, which shows an X-ray irradiation flux of $F_{\mathrm{X,\,pl}} = 50\,\mathrm{erg\,s^{-1}}\,cm^{-2}$. Planets b and c show irradiation fluxes of $F_{\mathrm{X,\,pl}} = 16$ and $123\,\mathrm{erg\,s^{-1}}\,cm^{-2}$, respectively. While planet c is now rocky and likely does not have a thick gaseous envelope from which it can lose mass, it is possible that it was formed with a hydrogen-helium envelope that it lost over time, especially during higher X-ray activity epochs in the youth of the host star. We estimate that the larger planet b loses its atmosphere at a rate of about $5 \times 10^7\,\mathrm{g\,s^{-1}}$, that is, about an order of magnitude less than GJ 436 b. However, because the host star is optically brighter by a factor of about six, the ongoing evaporation of GJ 143 b may well be observable with current instrumentation.

K2-198 bcd: K2-198 is a K dwarf star that is located at a distance of 110.6 pc from the Sun, with an apparent *Gaia* brightness of $G = 11.0$ mag. It hast three known transiting planets (Mayo et al., 2018; Hedges et al., 2019): the innermost planet c orbits at a period of 3.4 days and has a radius of $1.4\,R_\oplus$ (Hedges et al., 2019), which places it in the regime of rocky planets. The middle planet d is a mini-Neptune with an orbital period of 7.5 days and a radius of $2.4\,R_\oplus$ (Hedges et al., 2019). The largest planet b is a Saturn-like planet in a wider orbit with an orbital period of 25.9 days and a radius of $4.2\,R_\oplus$ (Mayo et al., 2018). The eROSITA data determined the host star X-ray luminosity to be $7.9 \times 10^{28}\,\mathrm{erg\,s^{-1}}$ in the 0.2-2.0 keV band. This places all three planets in an intense X-ray irradiation regime with fluxes at the planetary orbits of about $F_{\mathrm{X,\,pl}} = 17020, 5890, \text{and } 1950\,\mathrm{erg\,s^{-1}cm^{-2}}$ for planets c, d, and b, respectively. The middle planet d is more strongly irradiated than the evaporating mini-Neptune GJ 436 b and can be expected to actively lose mass at a high estimated rate of $4 \times 10^{10}\,\mathrm{g\,s^{-1}}$. The innermost planet is likely to be rocky and might therefore no longer undergo any significantly mass loss. However, it is possible that it was formed with a primordial hydrogen-helium envelope that has been evaporated completely in the youth of the system. The highest-mass planet b shows an intermediate intensity of high-energy irradiation, which is lower than for the known evaporating hot Jupiter HD 189733 b, but higher than for GJ 436 b. We estimate it to undergo mass loss at a rate of $2 \times 10^{10}\,\mathrm{g\,s^{-1}}$.

K2-240 bc: K2-240 is an early-M dwarf that was discovered to host two transiting mini-Neptunes (Díez Alonso et al., 2018). It is located at a distance of 72.9 pc from the Sun and an apparent *Gaia* brightness of $G = 12.6$ mag. We determine its X-ray luminosity to be $3.7 \times 10^{28}\,\mathrm{erg\,s^{-1}}$ in the 0.2-2.0 keV band. The two mini-Neptunes orbit the star in 6.0 and 20.5 days each. Their X-ray irradiation levels are well above those of the evaporating Neptune GJ 436 b with $F_{\mathrm{X,\,pl}} = 5020$ and $980\,\mathrm{erg\,s^{-1}\,cm^{-2}}$ for planets b and c, respectively. We estimate their mass-loss rates to be $\dot{M} = 3\times10^{10}$ and $5 \times 10^{9}\,\mathrm{g\,s^{-1}}$ for planets b and c. This is higher than for GJ 436 b by more than an order of magnitude for planet b. These two planets may be good targets for follow-up observations of ongoing evaporation.

6.7 Conclusion

We have presented a catalogue of X-ray luminosities of exoplanet host stars, high-energy irradiation levels of exoplanets, and their estimated atmospheric mass-loss rates. We combined new data from the eROSITA mission first and second all-sky surveys (eRASS1 and eRASS2) and amended our catalogue with archival data from ROSAT, *XMM-Newton*, and *Chandra*. We presented high-energy irradiation levels for 329 exoplanets, 108 of which stem from first-time detections with eROSITA, and mass-loss estimates for 287 exoplanets, 96 of which are derived from first-time eROSITA detections. Particularly interesting targets for follow-up observations of ongoing mass loss were found, including two multi-planet systems that can lead to unique insights into the evolution of exoplanetary atmospheres over time.

6.8 Appendix

6.8.1 X-ray fluxes of host stars with nearby stellar companions

Information about the flux corrections we applied for X-ray data from exoplanet host stars with nearby stellar companions is given below. We used information about stellar companions from Mugrauer (2019). We checked all host stars with a known stellar companion within 50″ for the X-ray instruments they were detected with, and considered a multi-star system to be likely blended in eROSITA, ROSAT, *XMM-Newton*, and *Chandra* if the stellar separation is below 8, 30, 8, and 1″, respectively. In these cases we divided the final listed X-ray flux, which we used for the calculations of the planetary irradiation and mass loss, by the number of blended stars (typically two). If a star is close to or below the blending separation, but X-ray data from a telescope with higher spatial resolution were available, we used the high-resolution data as the final listed flux.

18 Del: This star has a known stellar companion at a separation of about 29.2″, and the only available X-ray detection stems from ROSAT, which does not resolve the two stars. We therefore assigned 50% of the detected ROSAT flux at the position of this binary system to the exoplanet host star.

2MASS J01033563-5515561 A: This star has a known stellar companion at a separation of about 2″, and the existing XMMNewton and eRASS detections do not resolve the system. We therefore assigned 50% of the detected eRASS flux at the position of this binary system to the exoplanet host star.

CoRoT-2: This star has a known stellar companion at a separation of about 4.1″. The existing *Chandra* observations resolve the system, but the *XMM-Newton* observations does not. However, the *Chandra* data showed that the companion star is very X-ray faint and does not significantly contribute to the total X-ray flux of the system (Schröter et al., 2011), so that no adjustment was necessary.

DS Tuc A: This star has a known stellar companion at a separation of about 5″ (Newton et al., 2019). The current eRASS catalog does not resolve the two stars, and we therefore assigned 50% of the detected eRASS flux at the position of this binary system to the exoplanet host star.

GJ 338 B: This star has a known optically brighter stellar companion at a separation of 17″. The only existing X-ray detection stems from ROSAT, which does not resolve this wide binary. We therefore assigned 50% of the detected *XMM-Newton* flux at the position of this system to the exoplanet host star.

HAT-P-16: This is a hierarchical triple system, with a close stellar companion known at a separation of 0.4″ from the planet host star, and another wide companion at a separation of 23.3″. The close AB system is not resolved in the existing *XMM-Newton* detection, but the wider C component is not blended. We therefore assigned 50% of the detected *XMM-Newton* flux at the position of this system to the exoplanet host star.

HD 103774: This star has a known stellar companion at a separation of about 6.2″, and X-ray detections are present from eRASS1 and eRASS2, which do not resolve the two stars. We therefore assigned 50% of the detected eROSITA flux at the position of this binary system to the exoplanet host star.

HD 142: This star has a known stellar companion at a separation of about 3.9″, and X-ray detections are present from eRASS1 and eRASS2, which do not resolve the two stars. We therefore assigned 50% of the detected eROSITA flux at the position of this binary system to the exoplanet host star.

HD 162004: This star, also known as ψ 1 Dra B, has a known stellar companion at a separation of about 30″, and an X-ray detections is only present from ROSAT, which does not fully resolve the two stars. We therefore assigned 50% of the detected ROSAT flux at the position of this binary system to the exoplanet host star.

HD 189733: This star has a known stellar companion at a separation of about 11.4″. The ROSAT data do not resolve the system, but the *Chandra* and *XMM-Newton* observations do. Furthermore, it is known from an analysis of the *Chandra* data (Poppenhaeger et al., 2013) that the stellar companion is much less X-ray bright than the planet host star, therefore no adjustment was necessary.

HD 195019: This star has a known stellar companion at a separation of about 3.4″, and X-ray detections are present from eRASS2, which does not resolve the two stars. We therefore assigned 50% of the detected eROSITA flux at the position of this binary system to the exoplanet host star.

HD 19994: This is a triple system in which the planet host star is orbited by a close binary system (components B and C) at a separation of about 2.2″. X-ray detections are present from eRASS1 and eRASS2, which do not resolve the three stars. We therefore assigned one-third of the detected eROSITA flux at the position of this system to the exoplanet host star.

HD 212301: This star has a known stellar companion at a separation of about 4.4″, and an X-ray detection is present from eRASS1, which does not resolve the two stars. We therefore assigned 50% of the detected eROSITA flux at the position of this binary system to the exoplanet host star.

HD 65216: This is a triple system in which the planet host star is orbited by a close binary system (components B and C) at a separation of about 7.2″. X-ray detections are present from eRASS1 and eRASS2, which do not resolve the three stars. We therefore assigned one-third of the detected eROSITA flux at the position of this system to the exoplanet host star.

HIP 65 A: This star has a known stellar companion at a separation of about 4″, and the existing X-ray detections from eRASS do not resolve the stars. We therefore assigned 50% of the detected eROSITA flux at the position of this system to the exoplanet host star.

HR 858: HR 858 is a late-F type star that was reported to have a co-moving stellar companion of spectral type M at a separation of 8.4″ (Vanderburg et al., 2019). An X-ray source found in the eRASS datasets is located at the position of the secondary star and not the planet-hosting primary, therefore we attribute the detected X-ray flux to the secondary alone and do not report an X-ray detection for the planet host star based on the available data.

Kepler-1651: This star has a known stellar companion at a separation of about 4.1″, and an X-ray detection is present from ROSAT, which does not resolve the two stars. We therefore assigned 50% of the detected ROSAT flux at the position of this binary system to the exoplanet host star.

LTT 1445 A: This star has a known stellar companion at a separation of about 6.7″. The eRASS data detect flux from the position of the secondary alone, and we attribute the detected X-ray flux to the companion star alone.

τ Boo: This star has a close stellar companion at a separation of about 2″. X-ray detections exist with several X-ray missions, including *Chandra.* The existing

Chandra observation is able to resolve the system and shows that the secondary is much fainter than the planet-hosting primary (Wood et al., 2018), so that no adjustment was necessary.

WASP-140: This star has a known stellar companion at a separation of about 7.2″, and an X-ray detection is present from eRASS2, which does not resolve the two stars. We therefore assigned 50% of the detected eROSITA flux at the position of this binary system to the exoplanet host star.

WASP-8: This star has a known stellar companion at a separation of about 4.5″, and an X-ray detection is present from eRASS1 and *Chandra*. *Chandra* observations have shown that the secondary is X-ray faint compared to the primary (Salz et al., 2015), and we therefore attribute the detected eRASS1 flux to the primary in our further calculations.

omi UMa: This star has a known stellar companion at a separation of about 6.8″, and an X-ray detection is present from ROSAT, which does not resolve the two stars. We therefore assigned 50% of the detected ROSAT flux at the position of this binary system to the exoplanet host star.

6.8.2 Table of exoplanet irradiation fluxes and estimated mass-loss rates

We show an excerpt from the electronic data table with the most interesting columns for exoplanetary considerations in Table 6.1.

Table 6.1: Excerpt from the available electronic data table; the full table has additional columns and 343 rows. Radius superscript A denotes planets without measured radius values whose radii were estimated according to the mass-radius relationship by Chen & Kipping (2017). The same method was used to estimate planet masses with no measured value, which are denoted with superscript B in the electronic table. Superscript C for the X-ray flux denotes that the host star adopted X-ray flux and all entries derived from it were adjusted for unresolved bound stellar companions. The provenance of the used X-ray flux is given as E, R, X, and C for eROSITA, ROSAT, *XMM-Newton*, and *Chandra*, respectively.

Planet	Distance [pc]	Semi-major Axis [AU]	M$_{pl}$ [$M_\oplus$]	R$_{pl}$ [$R_\oplus$]	X-ray provenance	F_X [erg s^{-1}cm^{-2}]	L_X [erg s^{-1}]	L_{XUV} [erg s^{-1}]	$F_{\mathrm{X,\,pl}}$ [erg s^{-1}cm^{-2}]	$F_{\mathrm{XUV,\,pl}}$ [erg s^{-1}cm^{-2}]	Mass-Loss [g s^{-1}]
11 Com b	93.2	1.29	6165.6	12.4^A	E	2.8e-14	2.9e+28	2.5e+29	6.3e+00	5.3e+01	6.1e+06
14 Her b	17.9	2.93	1481.1	13.1^A	X	2.4e-14	9.4e+26	1.2e+28	3.9e-02	5.1e-01	2.9e+05
18 Del b	76.2	2.60	3273.5	12.7^A	R	2.5e-13^C	1.7e+29	1.2e+30	9.2e+00	6.3e+01	1.5e+07
1RXS J160929.1-210524 b	139.1	330.00	3000.0	12.8^A	E	2.3e-13	5.4e+29	3.3e+30	1.8e-03	1.1e-02	2.7e+03
2MASS J01033563-5515561 AB b		84.00			E	7.8e-14^C					
2MASS J01225093-2439505 b	33.8	52.00	7786.5	12.3^A	E	4.8e-13	6.5e+28	5.1e+29	8.6e-03	6.6e-02	5.9e+03
2MASS J02192210-3925225 b		156.00			E	5.3e-14					
30 Ari B b	44.7	0.99	4392.4	12.6^A	R	2.9e-12	6.9e+29	4.0e+30	2.5e+02	1.5e+03	2.5e+08
51 Eri b	29.8	12.00			E	2.4e-13	2.5e+28	2.2e+29	6.2e-02	5.4e-01	
55 Cnc b	12.6	0.11	255.4	14.1^A	E	4.6e-14	8.7e+26	1.1e+28	2.4e+01	3.2e+02	1.3e+09
55 Cnc c	12.6	0.24	51.2	8.4^A	E	4.6e-14	8.7e+26	1.1e+28	5.5e+00	7.2e+01	3.1e+08
55 Cnc d	12.6	5.96	991.6	13.3^A	E	4.6e-14	8.7e+26	1.1e+28	8.7e-03	1.1e-01	1.0e+05
55 Cnc e	12.6	0.02	8.0	1.9	E	4.6e-14	8.7e+26	1.1e+28	1.3e+03	1.7e+04	5.2e+09
55 Cnc f	12.6	0.77	47.8	8.0^A	E	4.6e-14	8.7e+26	1.1e+28	5.2e-01	6.9e+00	2.7e+07
61 Vir b	8.5	0.05	5.1	2.1^A	E	7.2e-14	6.2e+26	8.6e+27	8.8e+01	1.2e+03	8.6e+08
61 Vir c	8.5	0.22	18.2	4.5^A	E	7.2e-14	6.2e+26	8.6e+27	4.7e+00	6.4e+01	1.2e+08
61 Vir d	8.5	0.48	22.9	5.2^A	E	7.2e-14	6.2e+26	8.6e+27	9.8e-01	1.3e+01	3.1e+07
AB Pic b	50.0	260.00	4290.5	12.6^A	E	2.4e-12	7.2e+29	4.2e+30	3.8e-03	2.2e-02	3.8e+03
...	...	...	...	...	...	...	...	...	...	...	

7 Identifying interesting planetary systems for future X-ray observations

7.1 Abstract

X-ray observations of star-planet systems are important to grow our understanding of exoplanets; these observation allow for studies of photoevaporation of the exoplanetary atmosphere, and in some cases even estimations of the size of the outer planetary atmosphere. The German-Russian eROSITA instrument onboard the SRG (Spectrum Roentgen Gamma) mission is performing the first all-sky X-ray survey since the 1990s, and provides X-ray fluxes and spectra of exoplanet host stars over a much larger volume than was accessible before. Using new eROSITA data as well as archival data from XMM-Newton, Chandra and ROSAT we estimate mass loss rates of exoplanets under an energy-limited escape scenario, and identify several exoplanets with strong X-ray irradiation and expected mass-loss that are amenable to follow-up observations at other wavelengths. We model sample spectra using a toy model of an exoplanetary atmosphere to predict what exoplanet transit observations with future X-ray missions such as Athena will look like, and estimate the observable X-ray transmission spectrum for a typical Hot Jupiter-type exoplanet.

Since the first exoplanet detected around a main-sequence star, the hot Jupiter 51 Peg b (Mayor & Queloz, 1995), exoplanets have continued to be detected around a diverse array of host stars. Mulders et al. (2018) suggest that between 45% and 100% of stars have at least one planetary companion and, in addition, systems without planets interior to the orbits of Mercury and Venus are rare. This means our solar system is likely abnormal in its distance to the host star, with most planets being much closer in to their host star than we are to our Sun. Due to their close orbits, many exoplanets are subject to strong stellar irradiation. This intense radiation can cause the gas in the exoplanet atmospheres to expand and be lifted out of the gravitational well of the planet, causing the atmosphere to evaporate (Owen & Jackson, 2012). In general, planet evaporation is thought to be driven by soft X-rays and extreme-ultraviolet (EUV) radiation received by the planet from its host star (Yelle, 2004; Murray-Clay et al., 2009). Whilst this EUV component is not directly observable with currently operational space observatories, the X-ray components may be observed from a number of different instruments.

As the driver of exoplanetary evaporation, high-energy irradiation is one of the most important input quantities of exoplanet evaporation rates. Thus, we are particularly interested in the X-ray and EUV irradiation of exoplanets. This X-ray irradiation of the planet can be calculated from the X-ray observations of their host stars. In turn, the stellar EUV flux can be estimated from the stellar X-ray emission and the UV part of the stellar spectrum (Sanz-Forcada et al., 2011; France et al., 2013).

We present here a characterisation of the high-energy environment of known exoplanets and estimate their mass loss rates using new X-ray data from eROSITA as well as archival data from other missions; in addition, we identify a number of systems that are interesting for follow-up observations with current or future X-ray missions, for example Athena.

7.1.1 eROSITA

eROSITA is the primary instrument on board the Spectrum Roentgen Gamma (SRG) mission (Sunyaev et al., 2021; Brunner et al., 2021). The instrument consists of seven mirror modules and is sensitive to the soft X-ray regime (Sunyaev et al., 2021). Launched in July 2019, eROSITA is producing an all-sky survey over four years called the eROSITA All-Sky Survey (eRASS) (Predehl et al., 2021). This survey will consist of eight independent X-ray maps, one produced every six months over the four years of continuously scanning the sky (Sunyaev et al., 2021).

We use data from the intermediate consortium-wide data release of the first and second full-sky surveys performed by eROSITA (eRASS1 and eRASS2 respectively) proprietary to the German eROSITA collaboration (i.e. with a galactic longitude higher than 180°). The eROSITA Science Analysis Software System (eSASS) (see Brunner et al. (2021)) was used to process the raw data, after which parameters such as positions and count rates in three energy bands, 0.2-0.6 keV, 0.6-2.3 keV, were listed. We focus on these extracted energy bands of the eRASS catalogue for this project.

7.2 Data Analysis

To gather the current information of X-ray irradiation of exoplanets as fully as possible, we use new eROSITA data along with archival data from XMM-Newton, Chandra and ROSAT. We use the NASA Exoplanet Archive catalogue downloaded on March 26, 2021[1] as the basis for cross matching with the individual X-ray catalogues. We exclude any exoplanets detected by the microlensing method due to their stellar distances having uncertainties of about 50%, which would propagate into our final exoplanetary mass-loss rates as very large uncertainties. We also discard the exoplanet around the cataclysmic variable HU Aqr, as the planet has been shown to be spurious (Schwope & Thinius, 2014; Bours et al., 2014; Goździewski et al., 2015).

Pre-eROSITA, the total number of of these planet-hosting stars that had been detected in the X-ray detected was 169 and through eRASS1 and eRASS2 this number increased by 74 to 243. We can expect this increase to be roughly double with the data from the Russian half of the eROSITA data as well as increasing further with the upcoming three years of eRASS surveys.

---

[1] `https://exoplanetarchive.ipac.caltech.edu`

7.2.1 Flux Comparisons

The fluxes reported in the X-ray catalogues used were each provided in slightly different energy bands. Therefore, before any further analysis could be done we opted to convert all fluxes into the commonly used 0.2-2.0 keV energy band. The following conversions were used for each telescope.

eROSITA: The eRASS stellar fluxes were calculated by applying the relative conversion factor to the power-law-derived fluxes from the intermediate eRASS catalogues. This factor was found to be $F_{\mathrm{X,\,coronal}} = 0.85 F_{\mathrm{X,\,powerlaw}}$ (see Foster et al. (2021)).

ROSAT: Assuming a typical coronal temperature of $kT = 0.3$ keV, we to transform the ROSAT fluxes from the 0.1-2.4 keV band into the 0.2-2 keV band, using the WebPIMMS[2] tool. The conversion factor is $F_{\mathrm{X,0.2-2\,keV}} = 0.87 \times F_{\mathrm{X,0.1-2.4\,keV}}$.

XMM-Newton: Although the XMM-Newton catalogue already provides the 0.2-2 keV band by summing bands 1 (0.2-0.5 keV), 2 (0.5-1.0 keV), and 3 (1.0-2.0 keV), the fluxes assume a power-law spectrum. In order to convert this into an underlying stellar coronal model we again use WebPIMMS. Here we find a typical correction factor of $F_{\mathrm{X,\,coronal}} = 0.87 F_{\mathrm{X,\,powerlaw}}$ for the 0.2-2 keV band for the combined signal from the EPIC cameras.

Chandra: In its second source catalogue, Chandra lists fluxes which are not specifically model dependent. Thus we simply constructed the soft flux 0.2-2.0 keV band by combining the u (0.2-0.5 keV), s (0.5-1.2 keV), and m (1.2-2.0 keV) bands.

After the fluxed for all data sets to cover were converted into the 0.2-2 keV range, we compared the fluxes observed for the stars which were detected by multiple missions. They were found to be in good agreement with each other (see Figure 9 in Foster et al. (2021) for the comparison between missions).

7.3 Results

7.3.1 XUV Irradiation

Incident X-ray and extreme-ultraviolet (combined, in short, to XUV) flux on a planet is thought to be the driver of the energy-limited escape process in which exoplanets are assumed to lose parts of their atmosphere (Watson et al., 1981).

To estimate this stellar XUV fluxes we use the conversion put forward by Sanz-Forcada et al. (2011). This approach uses stellar coronal models to calculate the extreme-ultraviolet (0.013-0.1 keV) contribution to the spectra. Sanz-Forcada et al. (2011) gives a conversion between the logs of the extreme-ultraviolet and the X-ray flux in the 0.1-2.4 keV. To change the X-ray flux in our catalogue in the 0.2-2 keV band into the required input band of 0.1-2.4 keV band we use WebPIMMS to find a ratio of 1.15 between the two fluxes. We then calculate the EUV flux from 0.013-0.1 keV using the conversion from Sanz-Forcada et al. (2011) and add the X-ray and extreme-ultraviolet fluxes together to find the XUV flux.

The XUV fluxes at the the planetary orbits shown in Fig. 7.1 are about five to ten times bigger than the fluxes in the X-ray 0.2-2.0 keV band on its own. The planets that we identify as particularly interesting for follow up observations are those which are highly irradiated and transiting.

---

[2] `https://heasarc.gsfc.nasa.gov/cgi-bin/Tools/w3pimms/w3pimms.pl`

Of the 59 transiting planets with X-ray detected host stars, 18 stem from new eROSITA discoveries. Comparing the XUV irradiation fluxes with that of known evaporating exoplanets HD 189733 b and GJ 436 b, we find a total of 16 transiting exoplanets showing irradiation levels in excess of those experienced by GJ 436 b ($8.4 \times 10^2\,\mathrm{erg\,s^{-1}cm^{-2}}$). Four of these exoplanets experience levels in excess of that of HD 189733 b ($8.4 \times 10^4\,\mathrm{erg\,s^{-1}cm^{-2}}$). This is a strong indicator that we may be able to observe the ongoing evaporation of these exoplanets in optical and UV wavelength bands, as has been done for HD 189733 b and GJ 436 b.

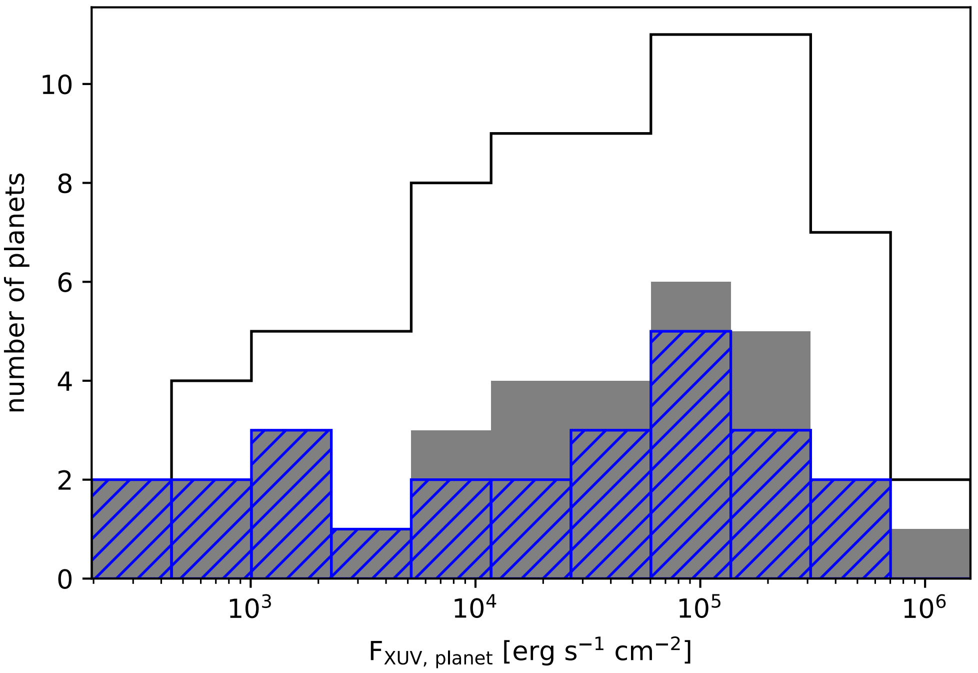

Figure 7.1: Histogram of the XUV flux at the planetary surface of exoplanets which are transiting their X-ray detected host stars (white with black outline). All exoplanets with host stars detected with eROSITA in the first two eRASS surveys are shown in solid grey, and the planets detected from the first time in X-rays by eROSITA are shown in striped blue.

7.3.2 Mass-Loss Rates

In the context of this work, we use a simple energy-limited hydrodynamic escape model based on Lopez et al. (2012) and Owen & Jackson (2012), and refer to Poppenhaeger et al. (2021) for the assumptions made in our model.

In instances where either the planet mass or the planet radius were known, but not both, we estimated the planet radius from its mass, or vice versa using the mass-radius relationship given by Chen & Kipping (2017). We plot the distribution of our estimate mass-losses in Fig. 7.2.

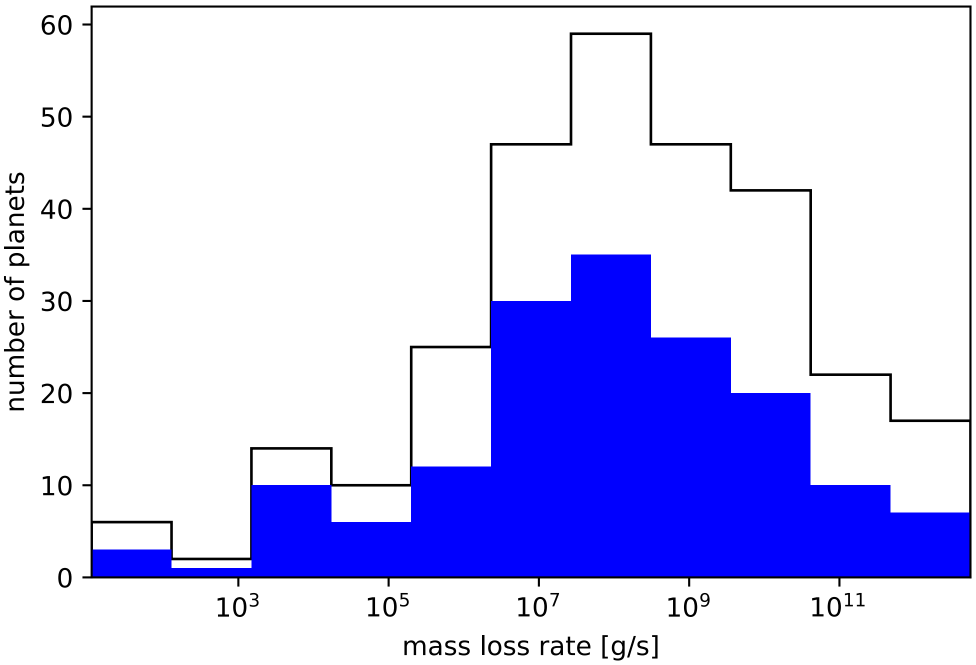

Figure 7.2: Histogram of the estimated mass loss rates of X-ray detected exoplanets (white with black outline) and the exoplanets with host stars detected with eROSITA in the first two eRASS surveys (blue).

The distributed mass-losses in Fig. 7.2 omit estimates for exoplanets with radii smaller than $1.6R_\oplus$. This is based on Rogers (2015), who showed that exoplanets smaller than $1.6R_\oplus$ are unlikely to undergo any significant atmospheric mass-loss as they are likely fully rocky.

With eROSITA, we measure four expected mass-loss rates higher than those of HD 189733 b for the first time ($1.8 \times 10^{11}\,\mathrm{g\,s^{-1}}$), as well as 14 new eROSITA measurements which have expected mass-loss rates higher than those of the Neptune GJ 436 b ($1.0 \times 10^{9}\,\mathrm{g\,s^{-1}}$).

7.4 Discussion

7.4.1 Interesting Systems

Systems where an exoplanet is both transiting its host star and highly irradiated are most suitable for follow up observations. With X-ray observatories such as eROSITA some of these systems are being observed in the X-ray regime for the first time. Especially interesting, are binary systems which can either be resolved for the first time, or will soon be resolvable either with further eROSITA surveys or future missions such as Athena.

DS TUC A

DS Tuc A is G-type star and the primary stellar component of its binary system, which includes the K3 secondary, DS Tuc B (Newton et al., 2019). DS Tuc A hosts a planet, DS Tuc A b, that has an orbital period of 8.14 days (Benatti et al., 2021). The system was partially resolved by the XMM-Newton in the MOS images, with both stars in the binary appearing with similar intensities (Benatti et al., 2021). However, Benatti et al. (2021) still reports that in estimating the fluxes there is cross-contamination of order of 16% due to the tight separation if the system.

In Foster et al. (2021) a high mass-loss rate of $6 \times 10^{11}\,\mathrm{g\,s^{-1}}$ was estimated for the planet of radius $5.7\,R_\oplus$ and mass $26.7\,M_\oplus$. This was estimated from the high stellar X-ray flux of $3.1 \times 10^{-12}\,\mathrm{erg\,s^{-1}cm^{-2}}$, which is 50% of the detected eRASS flux at the position of the DS Tuc binary system.

With more observations over future eRASS surveys we hope to fully resolve the binary system, which is separated by $5''$ (Newton et al., 2019), to make a more accurate calculation of the mass loss rate of DS Tuc A b using the actual X-ray flux of DS Tuc A.

WASP-180 A

WASP-180 A b is a transiting exoplanet whose host star has been detected in the X-ray regime for the first time with the eRASS surveys. This hot Jupiter orbits the primary star of a visual binary, WASP-180 A (Temple et al., 2019).

This planet, which has a mass of $0.9\,M_J$ and a radius of $1.2\,R_J$, is highly irradiated with an XUV flux of $5.7 \times 10^5\,\mathrm{erg\,s^{-1}cm^{-2}}$ at the planetary surface. This gives us an estimated mass loss rate of $2 \times 10^{12}\,\mathrm{g\,s^{-1}}$. This is a greater estimated mass loss rate than the that of the well known Hot Jupiter HD 189733 b (estimated to have a mass loss rate between 10^9 and $10^{11}\,\mathrm{gs^{-1}}$ by Lecavelier Des Etangs et al. (2010)) making this star a good target for follow up observations at other wavelengths to potentially directly observe the mass loss of WASP-180 A b.

7.4.2 Simulated Athena Spectra

In the future we will not only have the eROSITA mission for more in-depth X-ray observations. Exoplanetary science may be furthered with the Athena's ability for spatially resolved X-ray spectroscopy and deep wide-field spectral imaging. This instrument is expected to yield a vast improvement over the capabilities of current X-ray observatories such as XMM-Newton and eROSITA.

The Advanced Telescope for High Energy Astrophysics (Athena) mission, an X-ray observatory selected by the European Space Agency (ESA) in 2014, is currently scheduled to launch in 2031[3] (Barret et al., 2020). The observatory includes the high resolution X-ray spectrometer called the X-ray integral Field Unit (X-IFU) (Barret et al., 2018). This instrument will produce X-ray spectra in the 0.2 to 12 keV range with a spectral resolution of about 2.5 eV and a field of view of 5' (Barret et al., 2018).

The X-IFU, with its higher sensitivity and spectral resolution compared to current instruments, is expected to improved our knowledge of the effects of X-ray irradiation on exoplanets immensely. With this it may be possible to measure the transmission spectrum of exoplanet atmospheres during transits for the first time, making this mission of interest for the future of exoplanetary science (Barret et al., 2016).

---

[3] `https://sci.esa.int/web/athena/-/59896-mission-summary`

We use a density radius planet model by Salz et al. (2016) as a representation of how an atmosphere changes for planets of different masses (Fig. 7.3). From this we make a toy model of an atmosphere around a planet with 10% of the mass of WASP-10 b (Fig. 7.4). This model simplifies a planet atmosphere into areas of descending densities as we move away from the planetary surface. We take multiple cross-sections of the planetary atmosphere to calculate the column density through each concentric ring, as well as to calculate the area of the planet of this density. An example of one cross section is shown by the dotted black line in Fig. 7.4.

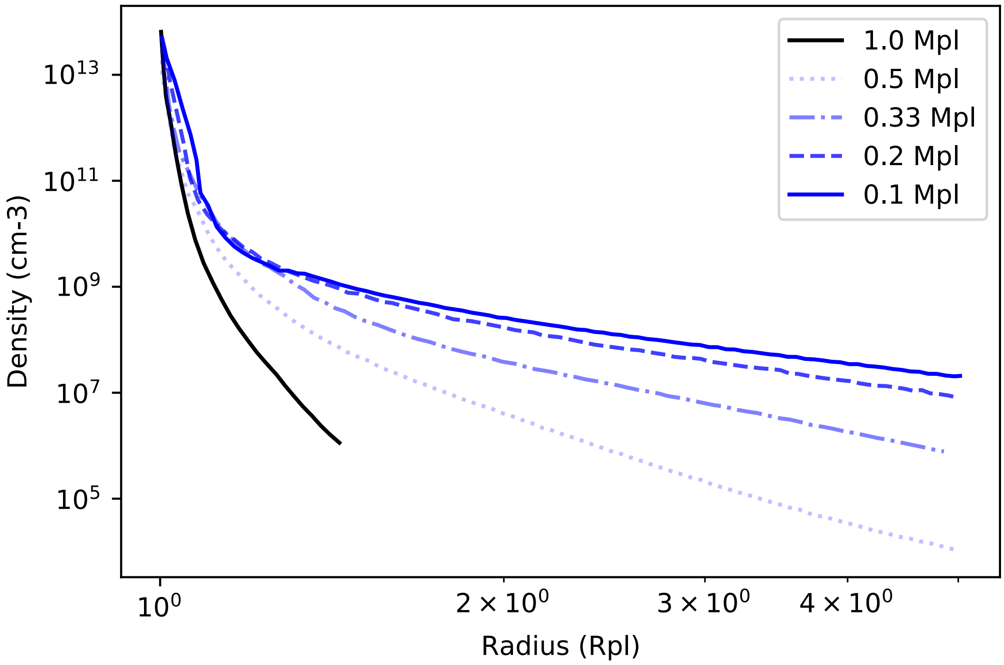

Figure 7.3: Density of planetary atmosphere of planets of differing masses in terms of the mass of WASP-10 b. The planets are with the same separation from their host star as that of WASP-10 b. Plot was adapted from Salz et al. (2016).

We then simulated spectra with XSPEC version 12.11.1 (Arnaud, 1996) using an APEC coronal model with differing absorbing columns, using multiplicative photo-electric absorption models, to simulate each ring of our toy atmosphere. We assumed solar abundances for the absorbing planetary atmosphere. We use a single temperature component with a kT of 0.4 keV for each model, corresponding to a temperature of approximately 4.6 million K, and an emission measure corresponding to a bright stellar X-ray flux of about 10^{-12} erg/s/cm^2 . We show how the spectra of the star changes during a planetary transit in Fig. 7.5.

The transmission spectra of the modelled transiting exoplanet is shown in Fig. 7.6, as the quotient of the X-ray spectrum with the planet in transit and the planet-free spectrum, simulated for 100 ks observing time accumulated in transit and outside of transit. This corresponds to co-added observations of the order of ten observed transits for typical transit duration of short-period exoplanets. Note the small ionisation edges at 0.5 keV and 0.3 keV in the model, which correspond to oxygen and carbon in the atmosphere respectively (Wilms et al., 2000). However, it is the absorption at very soft X-ray energies that will likely be best observable since at those energies the X-ray radius of the planetary atmosphere increases significantly.

Although it is unlikely the oxygen absorption edge the size of the one simulated here would be detectable from the uncertainties in the spectra, it is possible that this edge could be more prominent for some transiting planets. For example with respect to solar abundances, Jupiter has an atmosphere enriched in carbon by a factor of about three (Öberg & Wordsworth, 2019). Similar conditions in hot Jupiters with respect to their host stars may produce transmission spectra with more prominent absorption edges which would be more easily detectable with Athena.

7.5 Conclusion

We have presented high-energy irradiation levels and mass-loss estimates for exoplanets with X-ray observations using new eROSITA data as well as archival data from XMM-Newton, Chandra and ROSAT. Particularly interesting targets for follow-up observations, DS Tuc and WASP-180, with either eROSITA or future X-ray missions, such as Athena, were identified.

We have modelled sample spectra of stars as seen by Athena and predict what exoplanetary transit observations will look like with this observatory. We use this to estimate the observable X-ray transmission spectrum for a hot Jupiter with a mass 10% of the mass of WASP-10 b. From this modelled transmission spectrum we identified that with future missions such as Athena the absorption of outer exoplanetary atmospheres may be identified using X-ray observations.

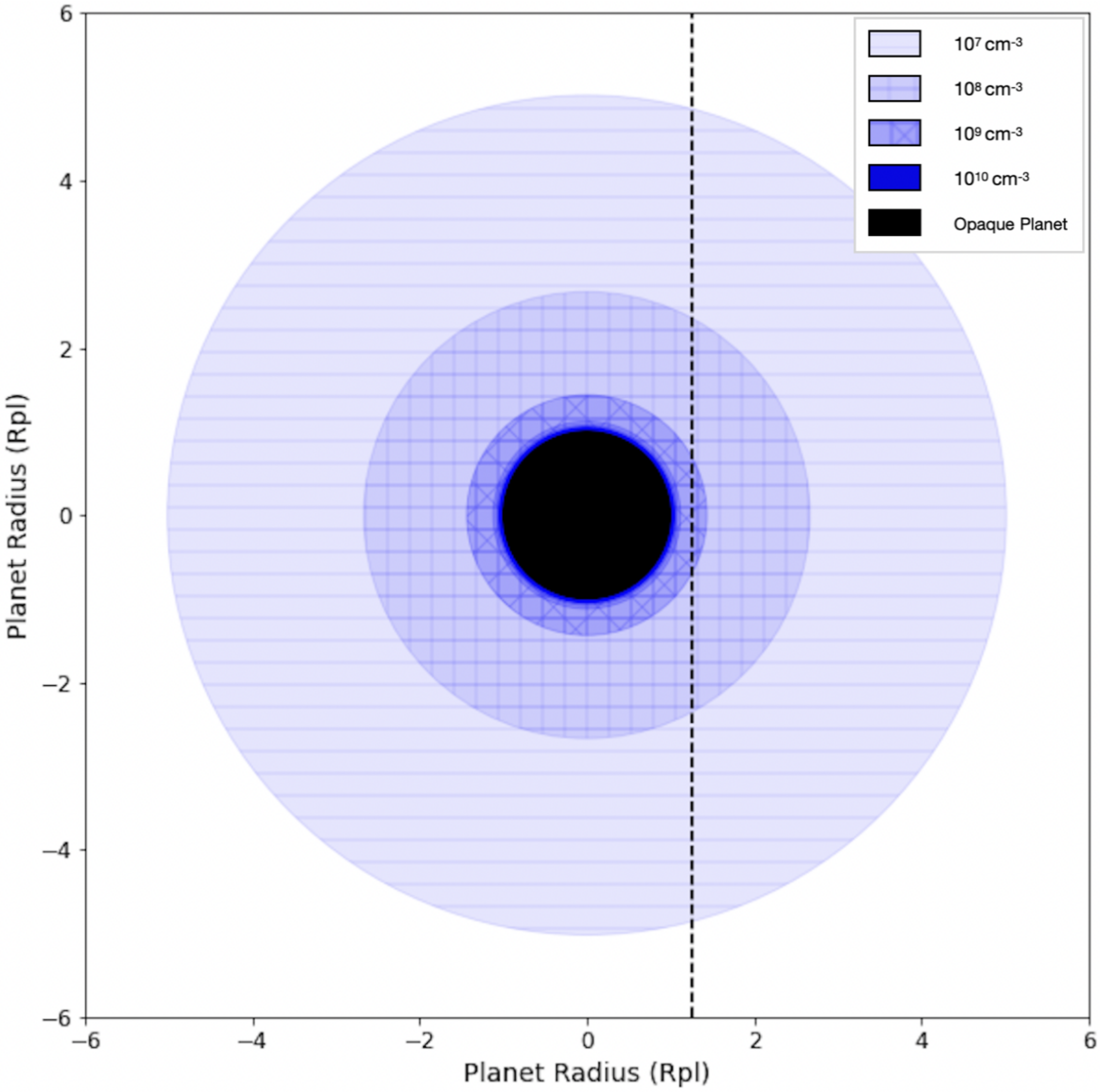
10^7 cm^{-3}
10^8 cm^{-3}
10^9 cm^{-3}
10^{10} cm^{-3}
Opaque Planet
Planet Radius (Rpl)
Planet Radius (Rpl)
6
4
2
0
−2
−4
−6
−6
−4
−2
0
2
4
6

Figure 7.4: Toy model of an exoplanet (rocky core shown by the solid black circle) and its atmosphere. The atmosphere has decreasing density as the distance from the planetary surface increases (concentric blue circles around the planet).

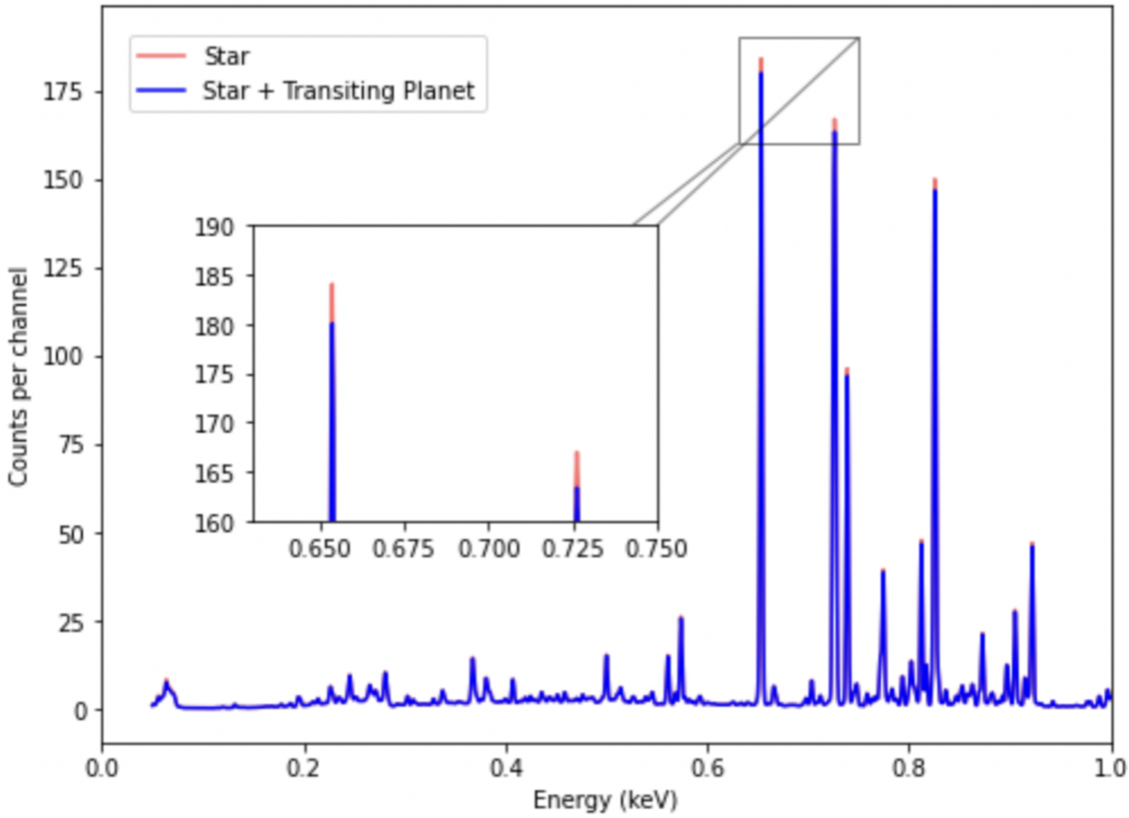

Figure 7.5: Spectrum of a model star with a transiting planet (blue) compared to the spectrum of the same star when no planet is present (red). A magnification of the two largest peaks is shown in the subplot to highlight the change more clearly.

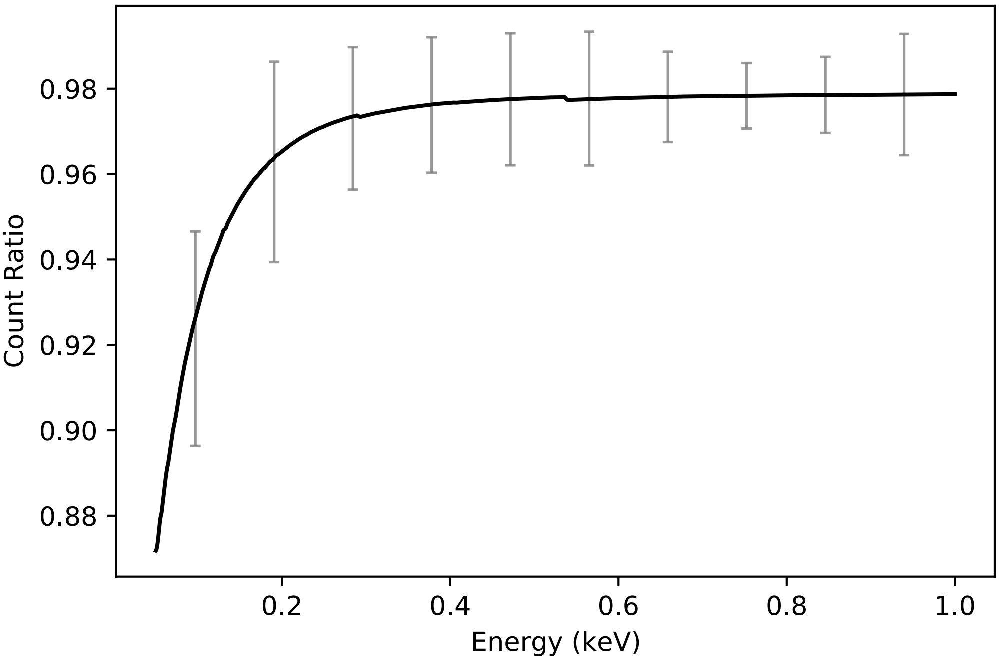

Figure 7.6: Model transmission spectrum of a star during the planetary transit of a planet with a mass that is 10% of the mass of WASP-10 b. Uncertainties are calculated for spectra with an accumulated exposure time of 100ks and a stellar X-ray flux of 10^{-12} erg/s/cm^2.

8 Conclusions

8.1 Scientific outcomes

In this work, X-ray observations have been discussed in their importance to exoplanetary studies.

8.1.1 Star-planet interactions

In chapter 5, X-ray observations were discussed with regards to characterising a star's corona and identifying the conditions necessary for star planet interactions. The X-ray emission from the M-dwarf star GJ 1151 was detected using *XMM-Newton* and used to estimate the star's low coronal temperature of 1.6 MK. Vedantham et al. (2020) previously reported variable radio emission observed from GJ 1151, which the authors explained with a scenario of sub-Alfvénic star-planet interaction. For this interaction to take place a specific set of conditions must be met by the star's corona, which rely on the stellar coronal temperature being low. X-ray observations are vital to characterising the corona and estimating the stellar coronal temperature, and therefore this observation was necessary to explaining the star planet-interaction between GJ 1151b and its host. Similar observations will be important for future characterisations of the interactions between an exoplanet and its host star.

8.1.2 Mass-loss rates

The mass-loss rate of an exoplanet's atmosphere not only give astrophysicists information on how that exoplanet is changing, but can also give a picture of how planets as a whole can evolve over time. In chapter 6 and chapter 7 X-ray luminosities of exoplanet host stars were presented using archival data from XMM-Newton, Chandra and ROSAT, along with new X-ray data from the eROSITA mission. Using this data, the X-ray flux incident on the exoplanet from its host star could be calculated, along with the mass-loss rates of the planets. In these chapters the new X-ray data used was from the combined eROSITA mission first and second all-sky surveys (eRASS1 and eRASS2). As this mission continues its all-sky survey in the coming years we can expect a greater population of X-ray observed host stars to be detected and therefore a great number of exoplanets with calculable mass-loss rates to increase our understanding of the evaluation of an exoplanet's atmosphere over time.

8.1.3 Identifying new targets

An important product of the catalogue of X-ray detected host stars as published in chapter 6 and discussed further in chapter 7 is the identification of targets which may be interesting for follow up observations. With the coming eROSITA observations and new observatories which will be discussed in the following section, more detailed follow up observations of planets with ongoing mass loss will be possible. These could include detailed observations of multi-planet systems which, in the future, can use X-ray observations to discover unique insights into the evolution of exoplanetary atmospheres.

8.2 Next generation of observatories

As discussed in chapter 6, in order to accurately calculate the mass-loss rate of an exoplanet's atmosphere, in addition to the X-ray component of the flux from the host star, the extreme ultraviolet (EUV) component is also needed. This EUV component of the stellar spectrum is currently not directly observable because no space observatories with sensitivity at the corresponding wavelengths are in operation; the EUVE satellite was the last major EUV observatory and ceased operations in 2001[1]. Until an observatory for these EUV missions is available, the X-ray part of the spectrum will be the focus of studies into the mass-loss rates of exoplanets, as well as being important to the characterisation of a host star's corona as discussed in chapter 5 and in the future being useful in identifying component's of an exoplanet's atmosphere as discussed in chapter 7. In this section we will discuss proposed X-ray missions and what they may contribute to exoplanetary science in the coming decades.

8.2.1 Athena

In chapter 7 we discussed the Advanced Telescope for High Energy Astrophysics (Athena) mission, currently scheduled to launch in 2031, as an interesting mission for exoplanetary science. This is due to Athena's plan on producing X-ray spectra in the 0.2 to 12 keV range with a spectral resolution of about 2.5 eV, and its much larger effective area in comparison to today's X-ray telescopes (Barret et al., 2018). In this chapter, model sample spectra of stars as they would be seen by Athena were produced and predictions for what exoplanetary transit observations will look like with this observatory were made. With these predictions we were able to estimate the observable X-ray transmission spectrum for a hot Jupiter and thus identified the possibility that with Athena, the absorption of outer exoplanetary atmospheres may be identified using X-ray observations. Therefore, in the coming years we may consider the possibility of using X-ray observations to characterise the atmospheres of exoplanets.

8.2.2 Lynx

In the Decadal Survey on Astronomy and Astrophysics 2020 (National Academies of Sciences & Medicine, 2021), one of the three priority areas identified was "Pathways to Habitable Worlds"; a programme to identify and characterise Earth-like exoplanets. This survey identified necessary capabilities for achieving this scientific goals, which includes a high spatial and spectral resolution X-ray observatory which can probe stellar activity across the entire range of stellar types. This is the basis of

---

[1] `https://heasarc.gsfc.nasa.gov/docs/euve/euve.html`

Lynx, one of the four NASA strategic mission concepts under consideration. Lynx, if built and launched, will carry a number of instruments, most notably the High Definition X-ray Imager (HDXI) and the X-ray Grating Spectrometer (XGS).

The HDXI will enable Lynx to survey the sky 800 time faster than Chandra and the optics design of Lynx will maintain sub-arcsecond spatial resolution out to ten arcminutes which is an improvement of a factor of sixteen over Chandra in area.

The XGS will provide the high spectral resolution as required for studying the physics of stellar corona and assessing the impact of stellar activity on exoplanets in the 0.2-2 keV energy band.

In summary, Lynx will be capable of studying stellar corona, the impacts of the X-ray flux of a host star on its exoplanet and provide insights on the effect of stellar X-rays on a planets habitability, further continuing the use of X-rays in the study of exoplanetary systems[2].

8.3 End notes on X-ray studies of exoplanets

To conclude, X-rays are integral to increase our understanding of exoplanetary systems both now and in the future. With X-ray observations we can characterise stellar corona, allowing us to verify the conditions for star planet interactions such as sub-Alfvénic interactions. We can also estimate the mass loss rates of exoplanets and thus make predictions on a planet's evolution using the X-ray flux incident on a planet from its host star. Finally, with upcoming missions such as Athena, we may be able to probe the upper atmosphere of exoplanets, which while opaque to X-rays are translucent to other wavelengths of light, thus allowing us to characterise the components of the exoplanet's atmosphere more fully.

With the scheduled Athena mission and the proposed Lynx mission, as well as the ongoing data from eROSITA, the future of X-ray observations is very exciting and will unlock the answers to questions about exoplanetary habitability and evolution for the decades to come.

---

[2] `https://www.lynxobservatory.com/mission`

Bibliography

Andrae R., et al., 2018, Astronomy and Astrophysics, 616, A8

Arnaud K. A., 1996, in Jacoby G. H., Barnes J., eds, Astronomical Society of the Pacific Conference Series Vol. 101, Astronomical Data Analysis Software and Systems V. p. 17

Astropy Collaboration et al., 2013, Astronomy and Astrophysics, 558, A33

Astropy Collaboration et al., 2018, Astronomical Journal, 156, 123

Ayres T. R., Brown A., Harper G. M., 2003, Astrophysical Journal, 598, 610

Bailer-Jones C. A. L., Rybizki J., Fouesneau M., Mantelet G., Andrae R., 2018, Astronomical Journal, 156, 58

Baraffe I., Chabrier G., Barman T., 2010, Reports on Progress in Physics, 73, 016901

Barnes S. A., 2010, Astrophysical Journal, 722, 222

Barret D., et al., 2016, in den Herder J.-W. A., Takahashi T., Bautz M., eds, Society of Photo-Optical Instrumentation Engineers (SPIE) Conference Series Vol. 9905, Space Telescopes and Instrumentation 2016: Ultraviolet to Gamma Ray. p. 99052F (`arXiv:1608.08105`), doi:10.1117/12.2232432

Barret D., et al., 2018, in den Herder J.-W. A., Nikzad S., Nakazawa K., eds, Society of Photo-Optical Instrumentation Engineers (SPIE) Conference Series Vol. 10699, Space Telescopes and Instrumentation 2018: Ultraviolet to Gamma Ray. p. 106991G (`arXiv:1807.06092`), doi:10.1117/12.2312409

Barret D., Decourchelle A., Fabian A., Guainazzi M., Nandra K., Smith R., den Herder J.-W., 2020, Astronomische Nachrichten, 341, 224

Benatti S., et al., 2021, Astronomy and Astrophysics, 650, A66

Benbakoura M., Réville V., Brun A. S., Le Poncin-Lafitte C., Mathis S., 2019, Astronomy and Astrophysics, 621, A124

Benz A. O., 2008, Living Reviews in Solar Physics, 5, 1

Böhringer H., et al., 2001, Astronomy and Astrophysics, 369, 826

Boller T., Freyberg M. J., Trümper J., Haberl F., Voges W., Nandra K., 2016, Astronomy and Astrophysics, 588, A103

Bolmont E., Gallet F., Mathis S., Charbonnel C., Amard L., Alibert Y., 2017, Astronomy and Astrophysics, 604, A113

Bours M. C. P., et al., 2014, Monthly Notices of the RAS, 445, 1924

Brunner H., et al., 2021, arXiv e-prints, p. arXiv:2106.14517

Butler R. P., et al., 2006, Astrophysical Journal, 646, 505

Cash W., 1979, Astrophysical Journal, 228, 939

Cauley P. W., Shkolnik E. L., Llama J., Bourrier V., Moutou C., 2018, Astronomical Journal, 156, 262

Chadney J. M., Galand M., Unruh Y. C., Koskinen T. T., Sanz-Forcada J., 2015, Icarus, 250, 357

Chadney J. M., Koskinen T. T., Galand M., Unruh Y. C., Sanz-Forcada J., 2017, Astronomy and Astrophysics, 608, A75

Charbonneau D., Brown T. M., Latham D. W., Mayor M., 2000, Astrophysical Journal, Letters, 529, L45

Charbonneau D., Brown T. M., Noyes R. W., Gilliland R. L., 2002, Astrophysical Journal, 568, 377

Chauvin G., Lagrange A. M., Dumas C., Zuckerman B., Mouillet D., Song I., Beuzit J. L., Lowrance P., 2005, Astronomy and Astrophysics, 438, L25

Chen J., Kipping D., 2017, Astrophysical Journal, 834, 17

Coffaro M., et al., 2020, Astronomy and Astrophysics, 636, A49

Cohen O., Drake J. J., Kashyap V. L., Sokolov I. V., Gombosi T. I., 2010, Astrophysical Journal, Letters, 723, L64

Cohen O., Ma Y., Drake J. J., Glocer A., Garraffo C., Bell J. M., Gombosi T. I., 2015, Astrophysical Journal, 806, 41

Cuntz M., Saar S. H., Musielak Z. E., 2000, Astrophysical Journal, Letters, 533, L151

Díez Alonso E., et al., 2018, Monthly Notices of the RAS, 480, L1

Dong C., Lingam M., Ma Y., Cohen O., 2017, Astrophysical Journal, Letters, 837, L26

Dragomir D., et al., 2019, Astrophysical Journal, Letters, 875, L7

Ehrenreich D., et al., 2015, Nature, 522, 459

Evans I. N., Civano F., 2018, Astronomy and Geophysics, 59, 2.17

Evans I. N., et al., 2010, Astrophysical Journal, Supplement, 189, 37

Fischer C., Saur J., 2019, Astrophysical Journal, 872, 113

Fortney J. J., Nettelmann N., 2010, Space Science Reviews, 152, 423

Foster A. R., Ji L., Smith R. K., Brickhouse N. S., 2012, Astrophysical Journal, 756, 128

Foster G., Poppenhaeger K., Ilic N., Schwope A., 2021, arXiv e-prints, p. arXiv:2106.14550

France K., et al., 2013, Astrophysical Journal, 763, 149

Fulton B. J., et al., 2017, Astronomical Journal, 154, 109

Gaia Collaboration et al., 2018a, Astronomy and Astrophysics, 616, A1

Gaia Collaboration et al., 2018b, Astronomy and Astrophysics, 616, A1

Garmire G. P., Bautz M. W., Ford P. G., Nousek J. A., Ricker George R. J., 2003, in Truemper J. E., Tananbaum H. D., eds, Society of Photo-Optical Instrumentation Engineers (SPIE) Conference Series Vol. 4851, X-Ray and Gamma-Ray Telescopes and Instruments for Astronomy.. pp 28–44, doi:10.1117/12.461599

Goldreich P., Lynden-Bell D., 1969, Astrophysical Journal, 156, 59

Gosling J. T., Asbridge J. R., Bame S. J., Feldman W. C., Zwickl R. D., Paschmann G., Sckopke N., Russell C. T., 1982, Journal of Geophysics Research, 87, 239

Goździewski K., et al., 2015, Monthly Notices of the RAS, 448, 1118

Grevesse N., Sauval A. J., 1998, Space Science Reviews, 85, 161

Griest K., Safizadeh N., 1998, Astrophysical Journal, 500, 37

Güdel M., 2002, Philosophical Transactions of the Royal Society of London Series A, 360, 1935

Güdel M., 2004, Astronomy and Astrophysics Reviews, 12, 71

Güdel M., Nazé Y., 2009, Astronomy and Astrophysics Reviews, 17, 309

Güdel M., Guinan E. F., Skinner S. L., 1997, Astrophysical Journal, 483, 947

Günther H. M., Wolk S. J., Drake J. J., Lisse C. M., Robrade J., Schmitt J. H. M. M., 2012, Astrophysical Journal, 750, 78

Hedges C., Saunders N., Barentsen G., Coughlin J. L., Cardoso J. V. d. M., Kostov V. B., Dotson J., Cody A. M., 2019, Astrophysical Journal, Letters, 880, L5

Hempel M., Robrade J., Ness J. U., Schmitt J. H. M. M., 2005, Astronomy and Astrophysics, 440, 727

Henry G. W., Marcy G. W., Butler R. P., Vogt S. S., 2000, Astrophysical Journal, Letters, 529, L41

Hudson H. S., Acton L. W., Freeland S. L., 1996, Astrophysical Journal, 470, 629

Irwin J., Berta Z. K., Burke C. J., Charbonneau D., Nutzman P., West A. A., Falco E. E., 2011, Astrophysical Journal, 727, 56

Jansen F., et al., 2001, Astronomy and Astrophysics, 365, L1

Johnstone C. P., Güdel M., 2015, Astronomy and Astrophysics, 578, A129

Johnstone C. P., Bartel M., Güdel M., 2020, arXiv e-prints, p. arXiv:2009.07695

Kashyap V. L., Drake J. J., Saar S. H., 2008, Astrophysical Journal, 687, 1339

King G. W., Wheatley P. J., 2021, Monthly Notices of the RAS, 501, L28

Kraft R. P., Burrows D. N., Nousek J. A., 1991, Astrophysical Journal, 374, 344

Kraft R. P., et al., 2000, Astrophysical Journal, Letters, 531, L9

Kulow J. R., France K., Linsky J., Loyd R. O. P., 2014, Astrophysical Journal, 786, 132

Lanza A. F., 2008, Astronomy and Astrophysics, 487, 1163

Lanza A. F., 2018, Astronomy and Astrophysics, 610, A81

Lecavelier Des Etangs A., et al., 2010, Astronomy and Astrophysics, 514, A72

Lindegren L., et al., 2018, Astronomy and Astrophysics, 616, A2

Linsky J. L., Fontenla J., France K., 2014, Astrophysical Journal, 780, 61

Lopez E. D., Fortney J. J., Miller N., 2012, Astrophysical Journal, 761, 59

Low B. C., 1996, Solar Physics, 167, 217

Loyd R. O. P., et al., 2018, Astrophysical Journal, 867, 71

Maggio A., et al., 2015, Astrophysical Journal, Letters, 811, L2

Mayo A. W., et al., 2018, Astronomical Journal, 155, 136

Mayor M., Queloz D., 1995, Nature, 378, 355

Merloni A., et al., 2012, arXiv e-prints, p. arXiv:1209.3114

Miller B. P., Gallo E., Wright J. T., Pearson E. G., 2015, Astrophysical Journal, 799, 163

Mohanty S., Basri G., 2003, Astrophysical Journal, 583, 451

Monsch K., Ercolano B., Picogna G., Preibisch T., Rau M. M., 2019, Monthly Notices of the RAS, 483, 3448

Mugrauer M., 2019, Monthly Notices of the RAS, 490, 5088

Mulders G. D., Pascucci I., Apai D., Ciesla F. J., 2018, Astronomical Journal, 156, 24

Murray-Clay R. A., Chiang E. I., Murray N., 2009, Astrophysical Journal, 693, 23

Murray S. S., et al., 1997, in Siegmund O. H., Gummin M. A., eds, Society of Photo-Optical Instrumentation Engineers (SPIE) Conference Series Vol. 3114, EUV, X-Ray, and Gamma-Ray Instrumentation for Astronomy VIII. pp 11–25, doi:10.1117/12.283772

National Academies of Sciences E., Medicine 2021, Pathways to Discovery in Astronomy and Astrophysics for the 2020s, doi:10.17226/26141.

Newton E. R., Irwin J., Charbonneau D., Berlind P., Calkins M. L., Mink J., 2017, Astrophysical Journal, 834, 85

Newton E. R., et al., 2019, Astrophysical Journal, Letters, 880, L17

Nortmann L., et al., 2018, Science, 362, 1388

Öberg K. I., Wordsworth R., 2019, Astronomical Journal, 158, 194

Owen J. E., Adams F. C., 2014, Monthly Notices of the RAS, 444, 3761

Owen J. E., Jackson A. P., 2012, Monthly Notices of the RAS, 425, 2931

Pecaut M. J., Mamajek E. E., 2013, Astrophysical Journal, Supplement, 208, 9

Pillitteri I., Wolk S. J., Sciortino S., Antoci V., 2014, Astronomy and Astrophysics, 567, A128

Pont F., 2009, Monthly Notices of the RAS, 396, 1789

Poppenhaeger K., 2019, Astronomische Nachrichten, 340, 329

Poppenhaeger K., Wolk S. J., 2014, Astronomy and Astrophysics, 565, L1

Poppenhaeger K., Robrade J., Schmitt J. H. M. M., 2010, Astronomy and Astrophysics, 515, A98

Poppenhaeger K., Schmitt J. H. M. M., Wolk S. J., 2013, Astrophysical Journal, 773, 62

Poppenhaeger K., Ketzer L., Mallonn M., 2021, Monthly Notices of the RAS, 500, 4560

Predehl P., Schmitt J. H. M. M., 1995, Astronomy and Astrophysics, 500, 459

Predehl P., et al., 2021, Astronomy and Astrophysics, 647, A1

Raetz S., Stelzer B., Damasso M., Scholz A., 2020, arXiv e-prints, p. arXiv:2003.11937

Raghavan D., et al., 2010, Astrophysical Journal, Supplement, 190, 1

Reale F., 2007, Astronomy and Astrophysics, 471, 271

Remus F., Mathis S., Zahn J. P., 2012, Astronomy and Astrophysics, 544, A132

Rogers L. A., 2015, Astrophysical Journal, 801, 41

Rosen S. R., et al., 2016, Astronomy and Astrophysics, 590, A1

Salvato M., et al., 2018, Monthly Notices of the RAS, 473, 4937

Salz M., Schneider P. C., Czesla S., Schmitt J. H. M. M., 2015, Astronomy and Astrophysics, 576, A42

Salz M., Schneider P. C., Czesla S., Schmitt J. H. M. M., 2016, Astronomy and Astrophysics, 585, L2

Salz M., Schneider P. C., Fossati L., Czesla S., France K., Schmitt J. H. M. M., 2019, Astronomy and Astrophysics, 623, A57

Sanz-Forcada J., Micela G., Ribas I., Pollock A. M. T., Eiroa C., Velasco A., Solano E., García-Álvarez D., 2011, Astronomy and Astrophysics, 532, A6

Saur J., Grambusch T., Duling S., Neubauer F. M., Simon S., 2013, Astronomy and Astrophysics, 552, A119

Saxton R. D., Read A. M., Esquej P., Freyberg M. J., Altieri B., Bermejo D., 2008, Astronomy and Astrophysics, 480, 611

Schmitt J. H. M. M., 1997, Astronomy and Astrophysics, 318, 215

Schmitt J. H. M. M., Fleming T. A., Giampapa M. S., 1995, Astrophysical Journal, 450, 392

Schröter S., Czesla S., Wolter U., Müller H. M., Huber K. F., Schmitt J. H. M. M., 2011, Astronomy and Astrophysics, 532, A3

Schwope A. D., Thinius B. D., 2014, Astronomische Nachrichten, 335, 357

Shkolnik E., Walker G. A. H., Bohlender D. A., Gu P. G., Kürster M., 2005, Astrophysical Journal, 622, 1075

Skinner S. L., Güdel M., 2020, Astrophysical Journal, 888, 15

Skrutskie M. F., et al., 2006, Astronomical Journal, 131, 1163

Smith R. K., Brickhouse N. S., Liedahl D. A., Raymond J. C., 2001, Astrophysical Journal, Letters, 556, L91

Spake J. J., et al., 2018, Nature, 557, 68

Strüder L., et al., 2001, Astronomy and Astrophysics, 365, L18

Strugarek A., Brun A. S., Matt S. P., Réville V., 2014, Astrophysical Journal, 795, 86

Sunyaev R., et al., 2021, arXiv e-prints, p. arXiv:2104.13267

Telleschi A., Güdel M., Briggs K., Audard M., Ness J.-U., Skinner S. L., 2005, Astrophysical Journal, 622, 653

Temple L. Y., et al., 2019, Monthly Notices of the RAS, 490, 2467

Thompson B. J., Plunkett S. P., Gurman J. B., Newmark J. S., St. Cyr O. C., Michels D. J., 1998, Geophysics Research Letters, 25, 2465

Traulsen I., et al., 2020, Astronomy and Astrophysics, 641, A137

Trifonov T., Rybizki J., Kürster M., 2019, Astronomy and Astrophysics, 622, L7

Truemper J., 1982, Advances in Space Research, 2, 241

Truemper J., 1993, Science, 260, 1769

Turner M. J. L., et al., 2001, Astronomy and Astrophysics, 365, L27

Turnpenney S., Nichols J. D., Wynn G. A., Burleigh M. R., 2018, Astrophysical Journal, 854, 72

Vanderburg A., et al., 2019, Astrophysical Journal, Letters, 881, L19

Vedantham H. K., et al., 2020, Nature Astronomy, 4, 577

Vidal-Madjar A., Lecavelier des Etangs A., Désert J. M., Ballester G. E., Ferlet R., Hébrard G., Mayor M., 2003, Nature, 422, 143

Villarreal D'Angelo C., Vidotto A. A., Esquivel A., Hazra G., Youngblood A., 2021, Monthly Notices of the RAS, 501, 4383

Voges W., et al., 1996, in Zimmermann H. U., Trümper J., Yorke H., eds, Roentgenstrahlung from the Universe. pp 637–640

Voges W., et al., 1999, Astronomy and Astrophysics, 349, 389

Voges W., et al., 2000, IAU Cirulars, 7432, 3

Watson A. J., Donahue T. M., Walker J. C. G., 1981, Icarus, 48, 150

Watson M. G., et al., 2009, Astronomy and Astrophysics, 493, 339

Weisskopf M. C., O'Dell S. L., Elsner R. F., Van Speybroeck L. P., 1995, in Hoover R. B., Walker A. B., eds, Society of Photo-Optical Instrumentation Engineers (SPIE) Conference Series Vol. 2515, X-Ray and Extreme Ultraviolet Optics. pp 312–329, doi:10.1117/12.212599

Weisskopf M. C., Brinkman B., Canizares C., Garmire G., Murray S., Van Speybroeck L. P., 2002, Publications of the ASP, 114, 1

Willes A. J., Wu K., 2005, Astronomy and Astrophysics, 432, 1091

Wilms J., Allen A., McCray R., 2000, Astrophysical Journal, 542, 914

Wood B. E., Laming J. M., Warren H. P., Poppenhaeger K., 2018, Astrophysical Journal, 862, 66

Wright N. J., Newton E. R., Williams P. K. G., Drake J. J., Yadav R. K., 2018, Monthly Notices of the RAS, 479, 2351

Yelle R. V., 2004, Icarus, 170, 167

Zahn J. P., 2008, in Goupil M. J., Zahn J. P., eds, EAS Publications Series Vol. 29, EAS Publications Series. pp 67–90 (`arXiv:0807.4870`), doi:10.1051/eas:0829002

Zhou G., et al., 2021, Astronomical Journal, 161, 2

den Herder J. W., et al., 2001, Astronomy and Astrophysics, 365, L7

van Haarlem M. P., et al., 2013, Astronomy and Astrophysics, 556, A2

Acknowledgments

The list of people who I want to thank could almost double the length of this document but I'll try to keep it short.

I want to start by thanking my supervisor Katja Poppenhaeger who not only supported me academically both here at the AIP for my PhD and in Belfast for my undergrad degree, but who also was unbelievably supportive during the pandemic throughout this project. Thank you for always being willing to talk to me about basically anything in a time when it was especially easy to feel alone in a foreign country.

Thank you also to all my colleagues, especially my office pals Laura, Judy and Julian who I ended up rarely sharing an office with this past two years! An extra thank you to Laura for making the German summary of this work understandable and keeping me motivated throughout my time at the AIP. And to Engin and Mattias for their help in formatting this document.

I have an amazing group of friends and family who made all the lock-downs and self-isolation bearable. Thank you especially to Andrea, Rian, Billy and, as my dad calls you, "The Honourable North Elm Street Gang", who I'm sure know who you are. And thank you to the entire extended Foster/Apted/Meacock family who let me couch surf while I finished this dissertation and put up with me while I made them proof read endless times.

Thank you Johanna for not only being a wonderful friend, but also for helping with the German translations of this document – and if I'm honest all the German paper work I had to file too.

Last but certainly not least thank you to my parents for everything and more.

Declaration

I, Mary Grace Foster, confirm that all work in this document is my own.

Ort, Datum Signature